

# Ion-beam induced changes of magnetic and structural properties in thin Fe films

Dissertation  
zur Erlangung des Doktorgrades  
der Mathematisch-Naturwissenschaftlichen Fakultäten  
der Georg-August-Universität zu Göttingen

vorgelegt von  
Georg Alexander Müller  
aus Kassel

Göttingen 2003

D7

Referent: Prof. Dr. Dr. h.c. Klaus Peter Lieb  
Korreferent: Juniorprof. Dr. Markus Münzenberg  
Tag der mündlichen Prüfung: 20.01.2004

# Contents

<b>1</b>	<b>Introduction</b>	<b>1</b>
<b>2</b>	<b>Theoretical background</b>	<b>4</b>
2.1	Ferromagnetism . . . . .	4
2.1.1	Magnetization process . . . . .	4
2.1.2	Magnetic anisotropy . . . . .	6
2.1.3	Macromagnetism and internal fields . . . . .	9
2.2	Ion-solid interactions . . . . .	9
<b>3</b>	<b>Experimental methods and analysis</b>	<b>12</b>
3.1	Magneto-optical Kerr effect . . . . .	12
3.1.1	Origin and theory of the magneto-optical Kerr effect . . . . .	13
3.1.2	Experimental setup . . . . .	15
3.2	Magnetic orientation Mössbauer spectroscopy . . . . .	18
3.2.1	Hyperfine interactions . . . . .	19
3.2.2	Conversion electron Mössbauer spectroscopy . . . . .	22
3.2.3	Magnetic orientation Mössbauer spectroscopy: geometry and analysis . . . . .	24
3.3	Comparison of MOMS and MOKE . . . . .	27
3.4	Other measurement techniques . . . . .	30
3.4.1	X-ray diffraction . . . . .	30
3.4.2	Extended X-ray absorption fine structure . . . . .	32
3.4.3	Rutherford backscattering spectroscopy . . . . .	35
3.5	Sample preparation and treatment . . . . .	37
3.5.1	Sample preparation . . . . .	37
3.5.2	Sample bending . . . . .	37
3.5.3	Sample irradiation . . . . .	38
<b>4</b>	<b>Results for electron-beam deposited films</b>	<b>40</b>
4.1	Fluence and mass dependence . . . . .	40
4.1.1	Deposition, ion irradiation and RBS analysis . . . . .	40
4.1.2	Magnetic anisotropy (MOKE) . . . . .	42
4.1.3	Microstructure . . . . .	49
4.2	Influence of external stress and magnetization . . . . .	53
4.2.1	Deposition, experiments and layer structures . . . . .	53
4.2.2	Influence of stress (MOKE) . . . . .	57
4.2.3	Influence of stress (MOMS) . . . . .	59

4.2.4	Influence of pre-magnetization (MOMS) . . . . .	64
4.2.5	Crystallographic structure . . . . .	66
4.3	Summary . . . . .	68
<b>5</b>	<b>Discussion</b>	<b>70</b>
5.1	Symmetry of the magnetic anisotropy . . . . .	70
5.2	Influence of stress . . . . .	73
5.2.1	External mechanical stress . . . . .	73
5.2.2	Microscopical stress . . . . .	74
5.3	Influence of other external parameters . . . . .	76
5.4	Microscopical model for ion-beam induced anisotropy . . . . .	77
5.4.1	Irradiation induced defects . . . . .	77
5.4.2	Correlation between structure and magnetism . . . . .	78
<b>6</b>	<b>Effects of substrate and deposition method</b>	<b>81</b>
6.1	Deposition, ion irradiation and analysis . . . . .	81
6.2	Fe/Si(100) . . . . .	83
6.2.1	Magnetic anisotropy . . . . .	83
6.2.2	Crystallographic structure . . . . .	85
6.3	Fe/MgO(100) . . . . .	87
6.3.1	Magnetic anisotropy . . . . .	87
6.3.2	Crystallographic structure . . . . .	91
6.4	Discussion . . . . .	92
6.4.1	Structure of the PLD films . . . . .	92
6.4.2	Fe/Si . . . . .	93
6.4.3	Fe/MgO . . . . .	95
<b>7</b>	<b>Summary and outlook</b>	<b>97</b>
<b>A</b>	<b>PCSA-ellipsometry</b>	<b>100</b>
<b>B</b>	<b>CEMS Parameters</b>	<b>103</b>

# Chapter 1

## Introduction

In recent decades, much effort has been invested in the research of magnetic materials and particularly in magnetic films and multilayer systems [Gra93]. Especially magnetic anisotropy and the magneto resistance (MR) effect have been research topics due to their technological applications in magnetic storage and sensor systems. After Baibich and Grünberg [Bai88, Bin89] had discovered the giant magneto resistance effect (GMR) in 1989 and Miyazaki the tunneling magneto resistance effect (TMR) [Miy95, Moo96] in 1994, research in this field was more and more shifted towards complex multilayer systems with the aim of finding material combinations showing large MR effects. The rapid development in this field of research is evidenced by the fact that it took only 6 years from finding the GMR effect to its first technological application in a hard disc read-write head in 1995. Nowadays, the GMR technique has totally replaced the anisotropic magneto resistance (AMR) sensors that were in use since the beginning of the 1990s. Besides achieving a large magneto resistance effect, industry is interested in decreasing the lateral size of magnetically anisotropic devices. This is particularly needed to increase the storage density of hard disc drives in combination with the development of very small read-write heads. Thus, a technique for material modification in the nanometer scale is required. The irradiation of the films with an ion-beam seems to be a very promising tool, because it has been shown that for ion-beam lithography [Moe01] as well as for the focused ion-beam technique [Mei03, Reu03] the lateral resolution can be as small as 50 nm.

Several techniques for the modification of magnetic materials by ion irradiation are already well-known. One example is the change of the coercive field, induced by the mixing of cobalt and platinum atoms at the interfaces of Co-Pt multilayers by implanting helium ions penetrating the substrate [Cha98, Dev99a, Dev99b, Fer99]. Another one is the induction of uniaxial magnetic anisotropy by ion-beam assisted deposition of Fe or Ni films [Lew94, Far92].

One further mechanism for inducing uniaxial magnetic anisotropy was proposed by Neubauer et al. and Zhang et al. [Zha01, Zha00, Lie01, Neu98]. The anisotropy was induced in nickel films by the irradiation with heavy ions and relatively low energies. The ions did not penetrate into the substrate and therefore the total deposition of energy and the local disordering of the irradiated material, called "spike formation", occurred only within the film. Additionally, as a consequence of the low ion energies, any interface mixing effects were avoided. It was found that by modifying the external irradiation parameters, such as magnetic fields or mechanical stress, the direction of the anisotropy can be influenced. Up to now no general mechanism has been proposed to

describe all observed effects. Since the choice of the film material is decisive for the ion-solid interactions and consequently also for the induced magnetic anisotropy, further studies on various ferromagnetic metals and alloys are presently being carried out [Gup03a, Gup03b, Zha03b].

In the present work the results concerning the low-energy irradiation of iron films will be presented. Iron has a low magnetostriction constant and the defect production due to ion implantation is not as efficient as in nickel. Apart from the mechanisms of the modification of magnetic materials, it is an important question how to measure the magnetic anisotropy. Usually the anisotropic behavior is characterized by considering the saturation energy or the magnetic remanence of the specimen, resulting from measurements of the hysteresis curves by means of the magneto-optical Kerr effect (MOKE), vibrating sample magnetometer (VSM) or superconducting quantum interference device magnetometer (SQUID) in different directions of the specimen. These techniques are sensitive either to the uppermost layer of the specimen (MOKE) or to the magnetization of the whole sample (VSM, SQUID). One possibility to analyze magnetic properties of films containing  $^{57}\text{Fe}$  is the method of conversion electron Mössbauer spectroscopy (CEMS). The depth range of this method is about 150 nm and even an analysis of buried layers of  $^{57}\text{Fe}$  is possible up to this depth. CEMS is generally applied to characterize the phase formation or structural properties of thin films [Sch91, Car02, Woi00, Reu01]. Nevertheless, when using a certain sample- $\gamma$ -ray geometry, it is an appropriate way to measure the angular in-plane distribution of the nuclear spins and therefore the magnetization direction in the film without magnetizing the specimen [Zem89]. Furthermore, the measurement is limited to the layer containing  $^{57}\text{Fe}$ , which allows a depth-dependent analysis. Several anisotropy measurements presented in this thesis were carried out by this new technique called "magnetic orientation Mössbauer spectroscopy" (MOMS) [Mue03a, Mue03b, Sch02, Sch03] in combination with MOKE. Recently, a similar hyperfine method has been established and successfully applied to nickel films [Mue03b, Kul03], using the perturbed angular correlation method (PAC) with implanted  $^{111}\text{In}$  ions as basis of the spin orientation measurement. As the magnetic analysis in Zhang's work on nickel films [Zha01] was concentrated on the measurement of the hysteresis curves by MOKE, the use of MOMS results in additional information. By comparing the results on Ni [Zha01] with those of this thesis many open questions concerning the mechanism of the formation of ion-beam induced magnetic anisotropy can be answered.

This thesis is organized in the following way: chapters 2 and 3 summarize the theoretical and experimental background of this thesis. In chapter 2 the most important information about magnetic anisotropy, magnetic hysteresis, the correlation between macromagnetism and internal magnetic fields, and ion-beam solid interactions will be presented. Chapter 3 covers the experimental techniques. After a short description of the MOKE theory, the experimental apparatus which was built for this research project will be described. A short discussion of geometry and analysis of the new method MOMS will follow and it will be compared with MOKE. Finally, further techniques used for the analysis and preparation of the films will be described.

In chapter 4, all the results on the films deposited by electron-beam evaporation on Si(100) or  $\text{SiO}_2$  will be presented. In section 4.1, the dependence of the magnetic anisotropy on the fluence and mass of various irradiated ion species is investigated. Section 4.2 summarizes the results on the dependence of the anisotropy orientation on various external irradiation parameters like mechanical stress or pre-magnetization of the samples. A discussion of these findings for electron-beam deposited films follows in chapter 5, including the development of a model for the

---

ion induced magnetic anisotropy. Before summarizing and giving an outlook in chapter 7, some experiments on the dependence of the anisotropy on the deposition method and the substrate will be presented in chapter 6. To investigate the occurring phenomena, films deposited onto Si(100) and MgO(100) by pulsed laser deposition (PLD) were irradiated by xenon ions.

# Chapter 2

## Theoretical background

In this chapter some important theoretical background to this thesis will be briefly summarized. In section 2.1 the characteristic features of ferromagnetic materials will be illustrated, in particular the macroscopic magnetization process, magnetic anisotropy, and the correlation of macro-magnetism, and hyperfine interactions at the atomic nucleus, as measured by the Mössbauer effect. In section 2.2 the various interactions between ion-beams and solids will be presented.

### 2.1 Ferromagnetism

#### 2.1.1 Magnetization process

The behavior concerning the application of an external magnetic field is probably the best known property of a ferromagnetic body: *”It is possible to change the over-all magnetization of a suitably prepared ferromagnetic specimen from an initial value of zero (in absence of an applied magnetic field) to a saturation value of the order of 1000 gauss, by the application of a field whose strength may be of the order of 0.01 oersteds.”* [Kit49].

The typical hysteresis loop of a ferromagnetic specimen shows mainly two characteristic behaviors. First, it is possible in certain cases to obtain a very large sample magnetization for a very small external magnetic field, and second, the magnetization can be zero for zero external field. Important characteristic quantities of a hysteresis curve (although not describing its shape) are the remanent or residual magnetization  $M_r$  and the coercive field  $H_c$ . The remanent magnetization is obtained when the specimen is magnetized to the highest magnetization state, called saturation magnetization  $M_s$ , and then the external field is reduced to zero. The external magnetic field necessary to demagnetize the sample is the coercive field  $H_c$ . The parameters are illustrated in Figure 2.1 by means of a hysteresis loop of a 75 nm thick nickel film.

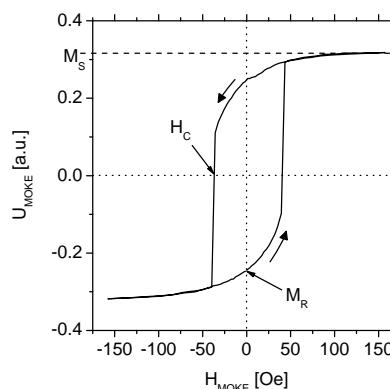


Figure 2.1: Hysteresis loop of a 75 nm thick Ni film.



To explain the phenomenon of magnetic hysteresis the theory of magnetic domains is needed [Kit49, Chi97, Hub00]. Following this theory, each ferromagnetic body consists of several so-called "domains", all of them having a certain magnetization vector pointing in the direction of their "easy axis" of magnetization. The orientation of the magnetization along the easy axis is the most favored energy state of the domain and this behavior is closely related to magnetic anisotropy that will be described in the next section. The counterpart of the easy axis is the "hard axis" of magnetization.

In case of a virgin sample in a zero external field, all domains are randomly oriented. If an external field is applied to the specimen, the magnetization is basically altered by two different mechanisms:

- Domain wall displacement: the domains with a magnetization pointing roughly in the direction of the external field are growing, while the others become smaller by the movement of the domain separating walls. In a perfect single crystal the shift of the domain walls demands nearly no energy and that is why it is the favored mechanism for changing the magnetization direction.
- Magnetization rotation: in case the external magnetic field is not applied parallel to the direction of an easy axis of magnetization, the alignment of all domain magnetization vectors in this direction cannot be achieved by domain wall displacement. The magnetization of the domains will finally rotate coherently from the easy axis to the axis of the external field until the saturation state is reached. Usually the energy that is necessary to rotate the magnetization depends on the strength of the anisotropy (anisotropy constant) of the material and is larger than the domain wall displacement energy.

In conclusion, the structure of the domains and the specimen itself plays an important role for the shape of its magnetization curve.

Due to the knowledge about the domain structure and the mechanisms of its change, the origin of the remanent magnetization and the coercive field can be explained qualitatively. The remanence mainly originates from irreversible domain wall shifts and irreversible magnetization rotations. A good example of such an effect is the move of a domain wall over a lattice defect, vacancy, grain boundary or in general a "pinning center". The energy of the applied magnetic field is necessary to pass the pinning center, and when the external field is released the wall cannot recover its original position. Thus, the coercive field  $H_c$  should be small for a perfect crystal where domain wall shifts are easily possible and it will be much larger for the same material with a large amount of pinning centers.

To obtain a zero magnetization of a magnetized specimen, an external field of strength  $H_c$  must be applied in the reverse direction. Then the irreversible domain wall shifts which happened during the magnetization process are recovered. Therefore, the coercivity is a very good indicator of the density and strength of the pinning centers.

The stable magnetization state of a body is determined by minimizing the total energy

$$E = E_{mag} + E_{ex} + E_a + E_{me} \quad (2.1)$$

with the contributions  $E_{mag}$  being the magnetostatic energy,  $E_{ex}$  the exchange energy,  $E_a$  the anisotropy energy and  $E_{me}$  the magnetoelastic energy. Thus, the magnetism of a sample is a

complex interaction of many parameters like the external magnetic field, the material with its anisotropy constants, crystallographic structure, texture, defect structure, strains and stresses, and the properties of domain walls. Some of these energy terms will be discussed in section 2.1.2.

A more detailed discussion and further literature about the macroscopic hysteresis of a ferromagnetic specimen can be found in chapters 12 and 13 of [Chi64], chapter 18 of [Chi97], [Hub00], pp. 466 and pp. 595 and [Mor65] pp. 344.

### 2.1.2 Magnetic anisotropy

If the internal energy of a magnetic material varies with a change in the direction of magnetization the specimen is called magnetically anisotropic. Magnetic anisotropy originates from magnetic dipolar interactions and the spin-orbit interaction which depends, for instance, on the shape of the specimen, the crystallographic structure or the strain field of the sample. These terms will be briefly illustrated below. Additional terms can occur at interfaces or surfaces but will not be discussed here. More detailed descriptions of magnetic anisotropy can be found in [Chi97, San99, Joh96, IFF99, Mor65].

#### Shape anisotropy

If a ferromagnetic specimen has an irregular shape, it can be shown that - considering homogeneous magnetization - its internal energy is different for the different axes of its body. This effect is called shape anisotropy and it is a result of magnetostatic energy due to magnetic free poles at the outside surface of the body. The magnetostatic energy stemming from these free poles can be described as  $E = \frac{1}{2\mu_0} N \mathbf{M}^2 v$ , where  $\mathbf{M}$  is the magnetization,  $v$  the considered volume and  $N$  the "demagnetizing factor" which is a tensor, specific for the shape of the body.

The most important example is the demagnetizing factor of an ellipsoid of revolution with its long axis parallel to its z-axis,  $N_x = N_y = \frac{1}{2}(1 - N_z)$ , where  $N_z$  is the demagnetizing factor along the z-axis. For  $\theta$  being the angle between the magnetization and the z-axis, and  $\varphi$  the angle between x-axis and the projection of  $\mathbf{M}$  on the x-y-plane, the magnetostatic energy of the ellipsoid is [Chi97]

$$\begin{aligned} E &= \frac{1}{2\mu_0} M_s^2 v (N_x \sin^2 \theta \cos^2 \varphi + N_y \sin^2 \theta \sin^2 \varphi + N_z \cos^2 \theta) \\ &= \frac{1}{4\mu_0} M_s^2 v (3N_z - 1) \cos^2 \theta + \text{const.} \end{aligned} \quad (2.2)$$

Thus the energy depends on the direction of magnetization.

The shape anisotropy of a thin film is usually approximated by an ellipsoid that is considered to be infinitely small in z-direction (out-of-plane) in comparison with the x and y-directions. Therefore  $N_z \approx 1$  and the magnetostatic energy can be written as

$$E \approx \frac{1}{2\mu_0} M_s^2 V \cos^2 \theta. \quad (2.3)$$

According to this expression the contribution of the shape anisotropy results in an in-plane preferential orientation for the magnetization in thin films. This statement is correct for films

not thinner than a few monolayers. For even thinner films, interface and surface anisotropy contributions become more and more important [Gra93, Bro97].

### Magnetocrystalline anisotropy

The internal energy of a magnetic single crystal depends on the considered crystallographic axis of the lattice. The axis with the lowest internal energy is called easy axis of magnetization, whereas the one with the highest internal energy is the hard axis of magnetization. Multiple easy and hard axes as well as local minima of the internal energy are possible.

The effect of so-called magnetocrystalline anisotropy originates in the spin-orbit interaction [Daa94]. Apart from this, the exchange interaction and the dipolar interaction could also contribute to this anisotropy. However, the exchange interaction is proportional only to the scalar product of two spin vectors and is in conclusion independent of the lattice orientation. The dipole-dipole interaction contribution is very small or vanishes completely due to symmetry reasons. A thorough theoretical understanding of the magnetocrystalline anisotropy can be obtained from ab initio bandstructure calculations [Joh96, Daa91].

Besides this theory of magnetocrystalline anisotropy, a phenomenological approach to the energy dependence exists, including the so-called anisotropy constants  $K_i$  which describe the strength of the anisotropy. In this approach, the anisotropy energy is described by the direction cosines  $(\alpha_1, \alpha_2, \alpha_3)$  of the magnetization vector, resulting for a cubic crystal in [Chi97]:

$$E_a = K_0 + K_1(\alpha_1^2\alpha_2^2 + \alpha_2^2\alpha_3^2 + \alpha_3^2\alpha_1^2) + K_2\alpha_1^2\alpha_2^2\alpha_3^2 + \dots \quad (2.4)$$

or a hexagonal crystal in:

$$\begin{aligned} E_a = & K_0 + K_1(\alpha_1^2 + \alpha_2^2) + K_2(\alpha_1^2 + \alpha_2^2)^2 + K_3(\alpha_1^2 + \alpha_2^2)^3 + \\ & K_4(\alpha_1^2 - \alpha_2^2)(\alpha_1^4 - 14\alpha_1^2\alpha_2^2 + \alpha_2^4) + \dots \end{aligned} \quad (2.5)$$

Using spherical coordinates  $(\theta, \phi)$  instead of the  $\alpha_i$ , the magnetocrystalline anisotropy can be described by

$$E_a = \frac{K_1}{4} \sin^2 2\theta + \frac{K_3}{16} \sin^4 2\theta + \dots \quad (2.6)$$

for a cubic crystal in the special case of fourfold symmetry (e.g. Fe(100) surface), and by

$$E_a = K_0 + K_1 \sin^2 \theta + K_2 \sin^4 \theta + K_3 \sin^6 \theta + K_4 \sin^6 \theta \cos 6\phi + \dots \quad (2.7)$$

for the hexagonal crystal, which shows a uniaxial anisotropy.  $\phi$  and  $\theta$  are the angles with respect to the a and c axes of the crystal. An example of the fourfold anisotropy of an Fe(100) film deposited on MgO(100) is given in Figure 2.2 a). The  $\langle 100 \rangle$  direction is the easy axis for an iron single crystal and it is oriented in  $\varphi = 45^\circ$  direction in the presented polar plot.  $0^\circ$  is the  $\langle 100 \rangle$  direction of the MgO substrate. A more detailed discussion of this particular film will follow in chapter 6.3.

The magnitudes of the anisotropy constants strongly depend on the temperature and on the symmetry of the lattice. For instance the magnitude of the uniaxial anisotropy constant  $K_1$  for hexagonal (and therefore low-symmetry) cobalt is in the order of  $10^6$  erg/cm<sup>-3</sup> and therefore much larger than  $K_1$  for cubic iron or nickel ( $10^4$  -  $10^5$  erg/cm<sup>-3</sup>).

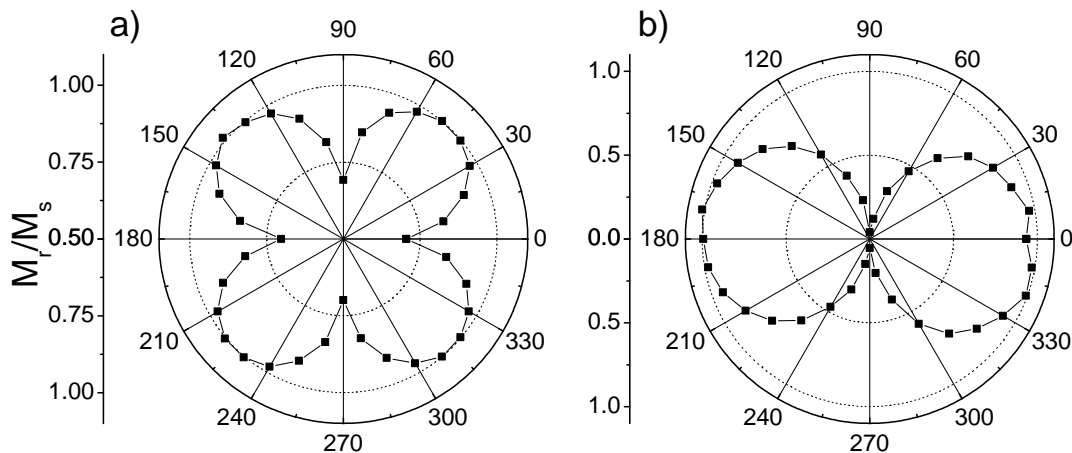


Figure 2.2: a) Fourfold anisotropy of a highly (100) textured Fe film due to magnetocrystalline anisotropy. b) Uniaxial anisotropy of a Ni film with compressive stress in  $0^\circ$  direction.

### Magnetoelastic anisotropy

Stress in a ferromagnetic body changes its magnetocrystalline anisotropy and may thereby alter the direction of the magnetization. This is the inverse effect to magnetostriction, where the sample dimensions change by variation of the magnetization direction. The energy per unit volume, associated with the inverse magnetostriction effect can be written as

$$E_{me} = -K_{me} \cos^2 \theta \quad (2.8)$$

for an elastically isotropic medium with isotropic magnetostriction constants. The magneto-elastic constant  $K_{me}$  can be written as  $K_{me} = -\frac{3}{2}\lambda\sigma$ , with  $\sigma$  being the stress, which is related to the strain  $\epsilon = \Delta l/l$  via the elastic modulus  $E$  by  $\sigma = E\epsilon$ . The magnetostriction constant  $\lambda$  depends on the crystallographic direction of the stress and can be positive if the easy axis is parallel to an external tensile stress or negative for the perpendicular case. It is well known that  $\lambda$  strongly depends on the considered material. The angle  $\theta$  measures the direction of the magnetization relative to the direction of the uniform stress. If the stress in the film is anisotropic and non-zero, the magneto-elastic coupling makes a uniaxial contribution to the effective anisotropy of the specimen. Typical examples of how strain can be induced in films are thermal stress due to different thermal expansion coefficients of film and substrate [Chi64], intrinsic stress caused by the nature of the deposition method [Kne62], stress due to non-matching lattice parameters of film and substrate [San99], or the application of external mechanical stress. An example of magnetic anisotropy in a 75 nm thick nickel film due to external compressive stress in  $0^\circ$  direction is given in Figure 2.2 b). Details about this experiment can be found in [Zha01].

### 2.1.3 Macromagnetism and internal fields

The hysteresis loop displays the characteristic macroscopic properties of a ferromagnetic material. In the case of the transition metals iron, cobalt and nickel these properties are based on the band magnetism [Sto36, Sto38, Boz51, Chi97] of the delocalized 3d bands, resulting in a spin polarization of the electrons. Besides this macroscopically measurable magnetization, an additional hyperfine field of the specimen can be found, having its origin in the s-electron shells which have a non-vanishing probability to penetrate the nucleus. The origin of this field is the polarization of the 1s, 2s and 3s electrons, caused by exchange interaction with the 3d electrons [Wat61, Mar58]. The polarization of the nucleus and therefore the hyperfine field occurs due to the Fermi contact interaction [Fer30], which is present not only for unpaired spins in atomic shells, but also for polarized spin bands in solids. Generally, 1s and 2s electrons produce negative internal fields, while 3s electrons produce positive fields.

In conclusion, the resulting hyperfine field must be oriented parallel or antiparallel to the spin polarization of the 3d band, depending on the radius of the 3d electrons and therefore the strength of the interaction. Because of this close relation between the magnetism of a crystal and the single nuclei, a lot of information about the magnetic properties of a specimen can be gained by nuclear techniques like Mössbauer spectroscopy (see section 3.3), nuclear magnetic resonance (NMR) or perturbed angular correlation (PAC) [Sch97], which base on the hyperfine interaction.

## 2.2 Ion-solid interactions

When ions hit the surface of a solid many different processes take place. On the one hand, there are processes occurring right at the surface of the material, such as sputtering. On the other hand, the majority of the effects is correlated to the stopping process of the ions in the solid, prominent features are ion-beam mixing, the formation of metastable phases, which is closely related to the mixing process, and ion-beam assisted deposition (IBAD). The subject of the following section is the stopping process of the ions [Nas96, Was90, Bol94, Ave94].

The interaction of an energetic ion with a solid involves several processes. As the ion penetrates the surface, it slows down by transferring energy to both the nuclei and the electrons of the solid. It comes to rest after several tens or hundreds of nm, depending on its initial energy, the element number and the density of the solid. The stopping power is consequently defined as

$$\frac{dE}{dx} = \left(\frac{dE}{dx}\right)_e + \left(\frac{dE}{dx}\right)_n, \quad (2.9)$$

where the electronic part is dominant for high energies and low mass projectiles and the nuclear part is more important in the low energy range and for ions with high masses. The transferred amount of energy for nuclear stopping is

$$E_t = E_0 \frac{4M_1M_2}{(M_1 + M_2)^2} \cos^2 \psi, \quad (2.10)$$

where  $M_1$  and  $M_2$  are the masses of the scattering atoms,  $E_0$  is the initial projectile energy and  $\psi$  is the angle between the incident ion and the dislocation direction of the target atom. Thus,

during the nuclear stopping, target atoms can be displaced from their lattice sites and relocated either in other lattice sites or in interstitial places, modifying the structure of the material.

Several phases of the time evolution of the ion-solid interaction are known. At the beginning of the interaction only the two-body collision of the implanted ion with a target atom (so-called "primary knock-on atom") is considered, which results - for a projectile energy larger than the dislocation energy  $E_d$  - in displacement and relocations of the target atoms. This phase of the primary interaction, called "collisional phase", lasts from  $10^{-13}$  to  $10^{-12}$  s after incidence of the ion.

Depending on the angle  $\psi$  of the first scattering process, the primary knock-on atoms themselves will induce a series of secondary and higher order recoils and dislocations, provided that they have a kinetic energy larger than the dislocation energy  $E_d$  which is typically 20 - 30 eV for a metal. The entire dislocated atoms, induced by a single projectile, is called "collision cascade". Since the kinetic energy, and as a result the free path length of the scattered atom, decreases after each scattering process, the spatial density of dislocated atoms will rise with increasing time after the first knock-on. Consequently, at the end of the "spike" a complete region around the cascade is in motion. This is essentially a local melt of the irradiated material in which the atoms move like in a diffusion process [And79]. This part of the collision cascade is called the "thermal spike phase". Considering typical values of stopping power, thermal conductivity and heat capacity for a transition metal, the maximum temperature within the spike is expected to be  $\gtrsim 1200$  K [Bol94]. The thermal spike phase ends about  $10^{-11}$  s after the initiation [Sei56]. By assuming that spikes can be created only by a space-filling cascade of displaced atoms, Sigmund [Sig74] postulated a critical kinetic energy  $E_c$ , below which the formation of a spike is possible. This energy depends on the atomic number of the target material  $Z_2$  and was estimated by Cheng [Che90] to be  $E_c = 0.039 \cdot Z_2^{2.23}$  (eV). In addition, for the dislocation of an atom, an energy larger than  $E_d$  is necessary, and therefore a spike can only be formed for ion energies satisfying the condition  $E_d < E < E_c$ . Based on this condition, a critical atomic number  $Z_2 = 20$  of the target material can be derived. For materials having  $Z < 20$  no thermal spike will form. For high energies of the projectiles the spike is not induced by the ion itself or by one of the first knock-on atoms, but by recoils of later generations. Thus, the formation of several "local spikes" will be favored over that of one "local or global spike".

The thermal spike phase is mainly responsible for the effects of ion-beam mixing in metallic and semiconductor materials. In addition to the ballistic process of dislocation of atoms, as a consequence of scattering, chemical effects play an important role. Since the atoms of different species in a spike can have a positive or a negative heat of mixing, the elements will be separated or mixed strongly. Apart from the heat of mixing the cohesive energy of the materials also plays an important role in the relaxation process of the melt because the mobility of the atoms can be enhanced or diminished [Nas96]. Nevertheless, the irradiation of the target produces defects and damages which cannot be compensated on account of the too short time scale and the restricted mobility of the atoms within the spike. A more detailed presentation of the mechanisms of ion-beam mixing is given in [Bol94, Har00, Nas96].

After the thermal spike phase, the irradiated region is often left with a large number of athermal defects, which can be several thousands per implanted ion. At sufficiently high target temperatures this non-equilibrium state may relax by thermally activated migration of the irradiation-induced defects. This stage is called "relaxation phase" and accounts for effects

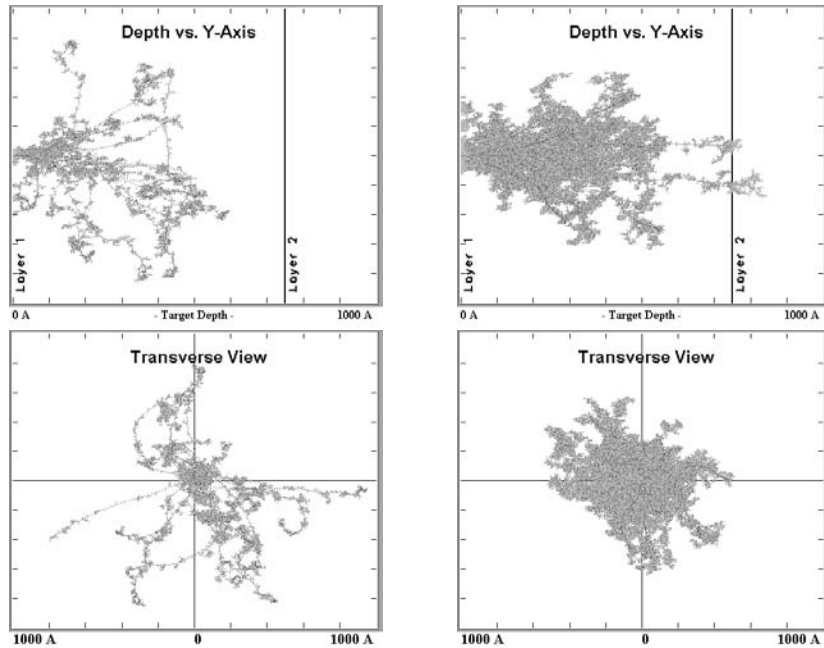


Figure 2.3: Simulation of ion tracks of 20 ions (left: 35 keV  $\text{Ne}^+$ , right: 200 keV  $\text{Xe}^+$ ) into a 75 nm thick Fe film on Si substrate. The top pictures depict depth distributions of the collision cascades while the bottom pictures show the z-projections of the cascades.

like radiation-enhanced diffusion. The formation of metastable phases can also be enhanced by thermally supported diffusion. Note, however, that this relaxation may also lead to the recombination and disappearance of defects and may even result in ion-induced grain growth or epitaxy.

Fig. 2.3 shows a comparison of the defect cascades produced by 35 keV  $\text{Ne}^+$  ions (left side) and 200 keV  $\text{Xe}^+$  ions in a 75 nm thick Fe film on a silicon substrate and simulated with *SRIM2003* [Zie99, SRI03] for 20 ions hitting the film at one point. It can be seen very clearly that not only the spatial distribution of the cascade is more focused for the heavier xenon ions, but also the defect density is much higher in this case. As a consequence, the regions with spike formation overlap and are not spread over the sample like in the case of neon irradiation. The projected range of both irradiations is  $R_p = 33(2)$  nm.

## Chapter 3

# Experimental methods and analysis

In this chapter the experimental methods and setups used in the thesis will be described briefly. Since a lot of effort has gone into developing a setup for the measurement of in-plane magnetic anisotropies via the magneto-optical Kerr effect (MOKE), the method and apparatus will be described in detail in section 3.1. Section 3.2 focusses on conversion electron Mössbauer spectroscopy (CEMS) and magnetic orientation Mössbauer spectroscopy (MOMS), a technique for the measurement of in-plane spin distributions that was developed and successfully applied in this thesis. A comparison of both methods, including first experimental results, will follow in section 3.3. The other techniques, used to characterize the structural properties of the specimens, are shortly reviewed in section 3.4. These are in particular Rutherford backscattering spectroscopy (RBS), X-ray diffraction spectroscopy (XRD), and extended X-ray absorption fine structure spectroscopy (EXAFS). Finally, the different methods of sample preparation and the geometries of the sample treatments are illustrated in section 3.5.

### 3.1 Magneto-optical Kerr effect

In 1876 John Kerr observed that linearly polarized light, reflected from a sample surface with the magnetization  $\mathbf{M}$ , will be elliptically polarized and that the main polarization axis will be rotated by an angle  $\phi_{Kerr}$  which is proportional to  $\mathbf{M}$ . This effect was later called the magneto-optical Kerr effect (MOKE). Depending on the orientation of the sample magnetization with respect to the incidence plane of the polarized light, three different MOKE geometries can be distinguished:

- transversal:  $\mathbf{M}$  is in the sample plane, but perpendicular to the incidence plane of the light
- longitudinal:  $\mathbf{M}$  is in the sample plane and parallel to the incidence plane of the light
- polar:  $\mathbf{M}$  is perpendicular to the sample plane

Besides the magneto-optical Kerr effect which considers the light reflected from the surface, two similar effects for the transmission geometry are known: the Faraday and the Voigt effect. Figure 3.1 shows the different geometries of the magneto-optical effects. With the Voigt effect, the influence of  $\mathbf{M}$  on the polarization state of the light is quadratic, for all others it is linear in



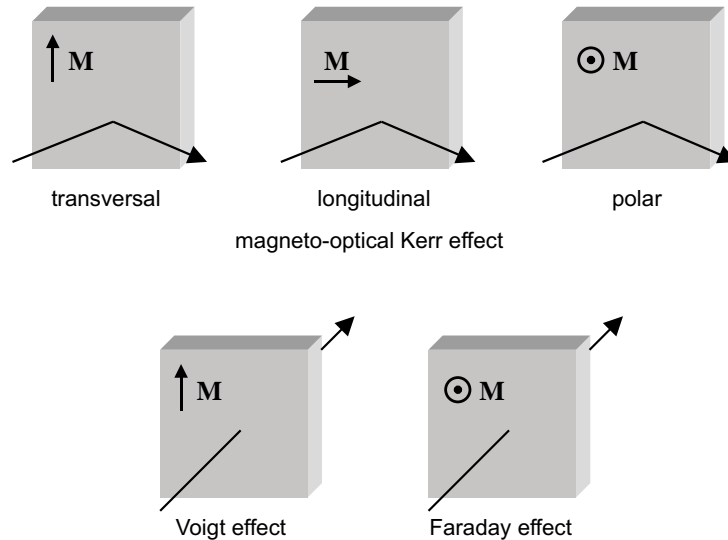


Figure 3.1: Orientation of the sample magnetization  $\mathbf{M}$  with respect to the incidence plane of the light for the different magneto-optical effects in reflection and transmission.

first approximation.

In recent years MOKE has become one of the most popular methods for measuring hysteretic parameters of ferromagnetic samples. Although MOKE is not sensitive to the absolute value of magnetization and its measurement depth is limited to the penetration depth of the used laser light, it is appropriate especially for the analysis of thin and ultrathin films down to monolayer thickness [Bad87, Moo89, Web96, Bro97, Ber01a].

### 3.1.1 Origin and theory of the magneto-optical Kerr effect

In the following the theoretical background of the Faraday and the magneto-optical Kerr effect will be presented. The early classical approaches to these phenomena, such as the Drude-Lorentz-theory [Gro79, Hub88], could explain the observed effects qualitatively or incompletely (only the rotation or the ellipticity), especially when considering ferromagnetic materials. The first successful theoretical model that was able to explain the Kerr rotation as well as the ellipticity and the proportionality regarding  $\mathbf{M}$  independent of the magnetic state of the specimen was published by Argyres [Arg55]. His approach is valid also for all extensions and generalizations made later on and that is why it will be briefly described here.

The quantum mechanical approach for the explanation of the Faraday and polar Kerr effect by Argyres is based on the one-electron-approximation for metals, including spin-orbit coupling and the interaction with the incident electromagnetic wave. The specimen is considered to be a ferromagnet with a homogeneous spontaneous magnetization like a single domain and is not influenced by an external magnetic field. The Hamiltonian of the system has the form:

$$H = H_0 + H' + H'' \quad (3.1)$$

where

$$H_0 = (1/2m)\mathbf{p}^2 + V(\mathbf{r}) \quad \text{kinetic and potential electron energy}$$

$$H' = (1/2m^2c^2)[\nabla V(\mathbf{r}) \times \mathbf{p}] \cdot \mathbf{s} \quad \text{electron spin-orbit interaction}$$

$$H'' = (e/mc)\mathbf{A}(\mathbf{r}, t) \cdot \mathbf{p} \quad \text{interaction with an electromagnetic field.}$$

$V(\mathbf{r})$  denotes the average potential energy of an electron in the crystal in absence of radiation, which means that only the average influence of the nuclei and the other electrons of the crystal is considered.  $\mathbf{A}(\mathbf{r}, t)$  is the vector potential of the electromagnetic field inside the material,  $\mathbf{p}$  is the electron momentum operator and  $\mathbf{s}$  the electron spin operator.

Now the Schrödinger equation  $H\Psi = i\hbar(\partial\Psi/\partial t)$  of (3.1) is solved by the method of variation of the constants, considering the parts  $H'$  and  $H''$  as perturbation terms. The aim of this approach is to obtain an expression for the wave function  $\Psi$  and the total current density  $\mathbf{J}_{\text{total}}$ , including conduction and polarization current. For this macroscopic total current density, the equation

$$\mathbf{J}_{\text{total}} = \sigma \cdot \mathbf{E} + \alpha \cdot \partial\mathbf{E}/\partial t \quad (3.2)$$

is derived,  $\sigma$  being the conductivity tensor,  $\alpha$  the polarizability tensor and  $\mathbf{E}$  the electric field of the light wave. This is the basic equation which results in all optical phenomena, when used in conjunction with Maxwell's equations for the electromagnetic field.

Before combining (3.2) with Maxwell's equations,  $\sigma$  and  $\alpha$  have to be derived. Several assumptions must be made to simplify the calculations; for example it is assumed that the light entering the material is perpendicular to the surface, the magnetization of the specimen is out-of-plane and the specimen has a cubic lattice structure with the light propagating along one of the cube axes. According to these assumptions, the conductivity and polarizability tensors simplify to:

$$\sigma = \begin{pmatrix} \sigma_0 & -\sigma_1 & 0 \\ \sigma_1 & \sigma_0 & 0 \\ 0 & 0 & \sigma_0 \end{pmatrix}, \quad \alpha = \begin{pmatrix} \alpha_0 & -\alpha_1 & 0 \\ \alpha_1 & \alpha_0 & 0 \\ 0 & 0 & \alpha_0 \end{pmatrix}, \quad (3.3)$$

where the non-diagonal elements  $\sigma_1$  and  $\alpha_1$  represent the spin-orbit interaction and therefore refer to the unpaired electrons in the ferromagnetic crystal. These elements vanish for a non-ferromagnet.

Using now Maxwell's equations

$$\nabla \times \mathbf{E} = -\frac{1}{c} \frac{\partial \mathbf{H}}{\partial t} \quad (3.4)$$

$$\nabla \times \mathbf{H} = \frac{1}{c} \frac{\partial \mathbf{E}}{\partial t} + \frac{4\pi}{c} \mathbf{J}_{\text{total}} \quad (3.5)$$

and introducing (3.2), the solutions for  $\mathbf{E}$  and  $\mathbf{H}$  have the form

$$\mathbf{E} = \mathbf{E}_0 e^{i\omega(t-Nz/c)} \quad (3.6)$$

$$\mathbf{H} = \mathbf{H}_0 e^{i\omega(t-Nz/c)} \quad (3.7)$$

with  $\mathbf{E}_0$  and  $\mathbf{H}_0$  being constant vectors and  $N$  the complex index of refraction. Solving the equation system (3.4) in combination with (3.6) one obtains two solutions of the refraction indices ( $N_+$  and  $N_-$ ), and the reflection and transmission for left and right circularly polarized light can be derived. Considering superpositions of this type, all polarization states can be described and thus the polarization rotations and ellipticities of Faraday and Kerr effect can be derived in dependence on the distance  $z$  from the boundary:

$$\begin{aligned}\phi_{Faraday} &= \frac{1}{2} \cdot (\omega z/c) \Re(N_+ - N_-) \\ \epsilon_{Faraday} &= -\tanh \left[ \frac{1}{2} \cdot (\omega z/c) \Im(N_+ - N_-) \right] \\ \phi_{Kerr} &= -\Im[(N_+ - N_-) / (N_+ N_- - 1)] \\ \epsilon_{Kerr} &= -\Re[(N_+ - N_-) / (N_+ N_- - 1)]\end{aligned}$$

with

$$\begin{aligned}N_+ - N_- &= (-4\pi) \frac{(\sigma_1/\omega) + i\alpha_1}{n - ik} \\ \frac{N_+ - N_-}{N_+ N_- - 1} &= (-4\pi) \frac{(\sigma_1/\omega) + i\alpha_1}{(n - ik) [(n - ik)^2 - 1]}\end{aligned}$$

In the final step an estimation for  $\sigma_1$  and  $\alpha_1$  is made, resulting in

$$\sigma_1 = -\frac{4ec}{m} \left\{ \sum_{m>n} \langle Q_{mn} / (\omega_{mn}^2 - \omega^2) \rangle \right\} \mathbf{M} \quad (3.8)$$

$$\alpha_1 = \frac{2\pi ec}{m} \left\{ \frac{1}{\omega^2} \sum_{m>n} \langle \delta(\omega_{mn} - \omega) Q_{mn} \rangle \right\} \mathbf{M} \quad (3.9)$$

where the  $Q_{mn}$  are the transition matrix elements for the concerned optical transition. Equation (3.8) shows the proportionality of the Faraday and the Kerr effect on the sample magnetization  $\mathbf{M}$ .

The presented model is in good qualitative agreement with the experimental results for visible and ultraviolet light. All effects are observed experimentally, although for instance the specimen is treated as a single ferromagnetic domain and the interactions between electrons and phonons are neglected. The latter assumption limits the theory to the wavelengths in the range of visible and ultraviolet light.

Several generalizations of Argyres' model were published. Bennett [Ben65] extended the theory, taking into account external magnetic fields and not considering a ferromagnetic body in particular. Cooper [Coo65] suggested a model that was not limited to the narrow frequency band of optical and ultraviolet light.

### 3.1.2 Experimental setup

The experimental setup is a PCSA-ellipsometer, similar to the one described in [Mue97]. A short review of the working principle is presented in appendix A.

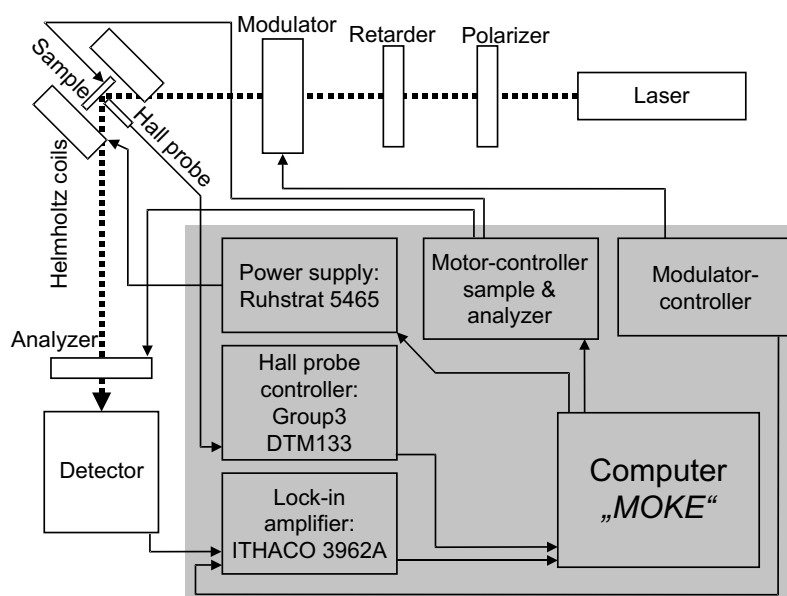


Figure 3.2: Schematic view of the PCSA-ellipsometer, constructed in the course of this thesis. The electronic components have a gray background, the optical part is shown with white background.

A schematic view of the optical (white background) and electronic (gray background) part of the setup is shown in Fig. 3.2. A helium-neon laser with a power of 2 mW and a wavelength of  $\lambda = 632.8$  nm (*Melles Griot*) is used as a light source. No special power stabilization is required, because the use of the modulator technique and the zero-point correction before each measurement makes the signal independent of small variations of the light intensity. To improve the polarity of the laser light, a dichroic polarizer is introduced into the beam. The extinction coefficient of this polarizer is given by the manufacturer *Melles Griot* to be  $< 3 \times 10^{-6}$  for the wavelength in use. The polarization axis is set  $90^\circ$  with respect to the incidence plane of the light on the sample (see appendix A).

After passing the polarizer the light is retarded by the  $\lambda/4$ -plate (*Melles Griot*), consisting of a birefringent mica-plate. Its thickness is chosen to obtain a difference in optical length for fast and slow axis of  $\lambda/4$  with a tolerance of  $\lambda/20$ . Therefore, the phase difference is  $\pi/2$ . As described in section A, the fast axis is oriented at  $\approx 45^\circ$  with respect to the linear polarization direction of the light and that is why the light leaves the retarder circularly polarized. By a slight variation of the retarder orientation, ellipticities caused by stresses of the polarizer during its mounting can be corrected.

Before hitting the sample, the light passes through the modulator. One way of modulating the polarization state of light is to use a Faraday cell [Rob63, Zei91] which is known to be very sensitive, but has the disadvantage of probably creating magnetic stray fields at the position of the sample. To avoid these stray fields, a photoelastic modulator (*PEM-90, HINDS instruments*) was used in the present setup. In this type of modulator a time-dependent birefringence is induced in a quartz crystal by a piezoelectric transducer. The modulator is run with a frequency of  $\nu = 50$  kHz and a retardation amplitude of  $\pi/2$ . In conclusion, the previously circularly po-

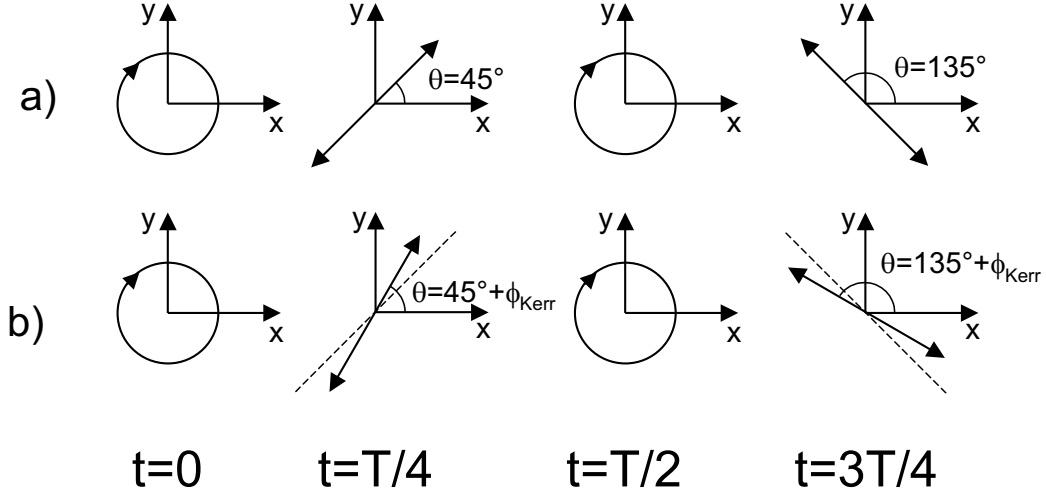


Figure 3.3: Modulation of the polarization state of the light during one period  $T$ . The linear polarity changes between a)  $45^\circ$  and  $135^\circ$  before and b)  $45^\circ + \phi_{Kerr}$  and  $135^\circ + \phi_{Kerr}$  after reflection from the sample surface.

larized light shows a modulated linear and circular polarization after having passed the modulator. The linear polarization is oriented at  $45^\circ$  after  $T/4$  or  $135^\circ$  after  $3T/4$  (see Fig. 3.3 a)). After being modulated, the light hits the specimen surface under an angle of about  $50^\circ$  with respect to the surface normal. The sample is placed in a magnetic field, produced by water cooled Helmholtz coils, each having 600 windings and an average radius of 80 mm. Applying a maximum current of 23 A at 150 V, the field strength  $H_{MOKE}$  is about 1600 Oe.  $H_{MOKE}$  is controlled online by a Hall probe (*DTM-133/LPT-230, Group3*) in front of the surface with the measured field having an accuracy of better than 0.06% at room-temperature.

The sample holder is either a goniometer which can be adjusted manually with an accuracy of  $0.1^\circ$ , or a computer-controlled goniometer which performs the automatized measurement of complete in-plane anisotropy polar diagrams with a step size of  $\geq 0.2^\circ$ . Nevertheless, the main limit of the accuracy is not due to the goniometer, but to the mounting of the sample. Consequently, the goniometer errors given above are negligible in comparison with the mounting error which is considered to be as large as  $2^\circ$ .

After being reflected from the magnetized sample surface, the light has changed its linear polarization state for  $t=T/4$  or  $3T/4$  to  $45^\circ + \phi_{Kerr}$  or  $135^\circ + \phi_{Kerr}$  direction.  $\phi_{Kerr}$  is the Kerr rotation obtained from the magnetized surface as discussed in section 3.1.1. The situation of the polarization states before and after being reflected by the sample is shown in Figure 3.3.

The analyzer is a dichroic sheet like the polarizer, but mounted in a precision polarizer holder (*Melles Griot*), which can be adjusted manually or motor-driven with an accuracy of 5 arc-min. The analyzer was set before each measurement to get the highest signal/noise ratio. Finally, a silicon photodiode detector (*S1337-1010BR, Hamamatsu*) is used for the detection of the light. Its sensitive area is  $1 \times 1 \text{ cm}^2$  to allow for an automatic  $360^\circ$  polar diagram

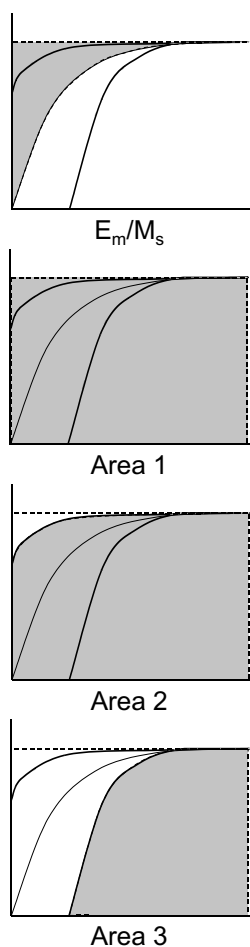


Figure 3.4: Areas necessary to derive the normalized magnetization energy  $E_m/M_s$ .

measurement of a sample without realignment of the setup during the measurement. The components of the MOKE setup are controlled by a computer via RS232-interface or a DA/AD input-output-card. Fig. 3.2 shows a diagram of all components and their signal connections. The controlling of the data recording is performed by the program *MOKE*, written in Visual C++ code in the course of this thesis. The data points of the hysteresis curves for several in-plane angles  $\varphi$  of the specimen's  $0^\circ$  axis with respect to the external magnetic field  $H_{MOKE}$ , are stored in separate files. After finishing all measurements on one sample, the saturation magnetization  $M_s$ , the relative remanence  $M_r/M_s$ , the coercive field  $H_c$ , and the normalized magnetization energy  $E_m/M_s$  are extracted from these files as a function of  $\varphi$ . This work and the creation of the final file, containing all information necessary for the polar plots of  $H_c$ ,  $M_r/M_s$  and  $E_m/M_s$ , is done by the program *MOKE-AUSWERTUNG*, also implemented in Visual C++. The program extracts the saturation magnetization by averaging the 5 highest values of the MOKE-signal in the positive as well as the negative branch of the hysteresis loop. The error is the mean error of this average. The remanence point is derived from linear regression of all points measured for magnetic fields in the range between  $-2$  Oe and  $+2$  Oe. This assumption is sufficient, especially for curves with at least 5 points in this interval. To obtain the coercive field  $H_c$ , the two points closest to the magnetization reversal are interpolated linearly. The error is the distance to the nearest measured point. The normalized magnetization energy is derived by integrating the area over the anhysteretic magnetization curve, as described by Brockmann et al. [Bro97]. The integration was done as presented in Fig. 3.4 by the equation

$$\frac{E_m}{M_s} = \text{Area 1} - \frac{\text{Area 2} + \text{Area 3}}{2}. \quad (3.10)$$

As the error of the coercive field is up to 3 Oe for some measurements, also the error for  $E_m/M_s$  is large in these cases.

A comparison of the parameters derived by the computer program with values obtained by "hand-made" analysis showed that all results are identical within the given errors.

## 3.2 Magnetic orientation Mössbauer spectroscopy

In 1957 Rudolph Mößbauer discovered that the energy loss due to resonant emission or absorption of a  $\gamma$ -ray photon vanishes by fixing the atom concerned in a crystal [Moe58]. This so-called Mössbauer effect has had an important impact on physics until today, because it has made possible the production of electromagnetic radiation with the narrow energy distribution of the natural line width of the transition by avoiding Doppler broadening. In combination

with the controlled motion of the emitter nucleus relative to the absorber atom and the related Doppler effect of the radiation, even hyperfine interactions can be observed. Therefore, Mössbauer spectroscopy is a powerful and destruction-free method for analyzing the crystallographic surrounding of the probe nucleus [Fra62, Gon75, Gre71, Weg66].

### 3.2.1 Hyperfine interactions

Basically, three different types of hyperfine interaction play a significant role in Mössbauer analysis. Their influence on the energy levels will be briefly described in the present paragraph; more detailed discussions can be found in [Gon75, Gre71, Sch97]. It is assumed that the source of the  $\gamma$ -rays is placed on a solid which moves periodically back and forth with a linear velocity profile, while the absorber is at rest. The energies in Mössbauer spectroscopy are usually expressed in the velocity unit [mm/s].

#### Chemical isomer shift $\delta$

It is sufficient for many purposes to describe a nucleus as a spherical charge, interacting with the electrons by Coulomb interaction. Taking into account the non-zero probability of s-electrons to penetrate the nucleus, the chemical isomer shift  $\delta$  refers to the change of the nucleus' volume, leading to a change of the nucleus-electron interaction energy. The energy levels of the ground and excited state are changed depending on the chemical environments  $E$  (emitter state) and  $A$  (absorber state) of the nucleus. The difference between the excitation energies  $\delta$  directly depends on these states:

$$\delta = \frac{2}{3}\pi Ze^2\{|\psi_s(0)_E|^2 - |\psi_s(0)_A|^2\}\{\langle R_e^2 \rangle - \langle R_g^2 \rangle\}. \quad (3.11)$$

$\psi_s(0)$  describes the (non-relativistic) Schrödinger s-electron wavefunction at  $r = 0$ ,  $Ze$  is the charge of the nucleus and  $\langle R_g \rangle$  and  $\langle R_e \rangle$  are the root mean square radii of its ground and excited state.

In equation (3.11) the nuclear term  $\{\langle R_e^2 \rangle - \langle R_g^2 \rangle\}$  and the atomic term  $\{|\psi_s(0)_E|^2 - |\psi_s(0)_A|^2\}$  can be distinguished, and because the nuclear term is constant for a given  $\gamma$ -ray transition the change  $\delta$  is only influenced by the chemical surrounding. Besides these influences also a relativistic temperature-dependent effect resulting from phonons of the emitter, and an effect of pressure on the isomer shift were discovered [Gre71].

#### Electric quadrupole interactions

The electric quadrupole interaction is closely related to the non-spherical charge distribution of nuclei

$$eQ = \int \rho r^2 (3 \cos^2 \theta - 1) d\tau, \quad (3.12)$$

where  $eQ$  denotes the nuclear quadrupole moment and  $\rho$  is the nuclear charge density in a volume element  $d\tau$  at a distance  $r$  from the center of the nucleus, having an angle  $\theta$  to the nuclear spin. The electronic charge distribution is not spherical, as described by

$$\eta = \frac{(V_{xx} - V_{yy})}{V_{zz}}. \quad (3.13)$$

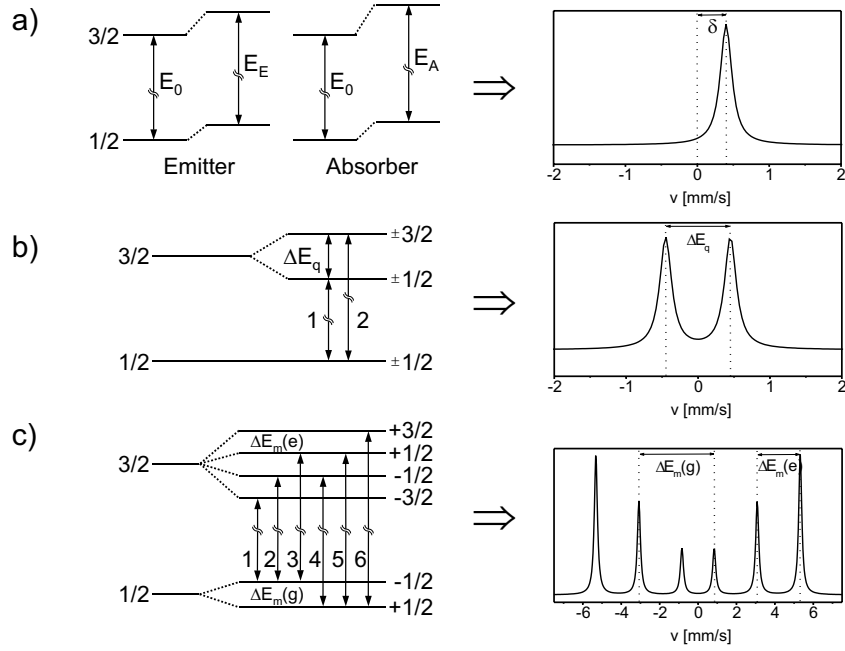


Figure 3.5: Energy level schemes and corresponding conversion electron Mössbauer spectra for the hyperfine interactions. a) Chemical isomer shift, b) electric quadrupole interaction, c) magnetic hyperfine interaction.

Using the convention that  $|V_{zz}| > |V_{yy}| \geq |V_{xx}|$ , the asymmetry parameter  $\eta$  must be  $0 \leq \eta \leq 1$ . The solution of the Hamiltonian for a general symmetry of the electric field gradient (EFG) and nuclear spin  $I = 3/2$ , as in the case of  $^{57}\text{Fe}$ , results in

$$E_q = \frac{eQV_{zz}}{4I(2I-1)} [3m_I^2 - I(I+1)] \left(1 + \frac{\eta^2}{3}\right)^{1/2}. \quad (3.14)$$

Other special cases for different symmetries of the EFG are discussed in [Gre71, Sch97].

### Magnetic hyperfine interactions

The effect of the magnetic hyperfine interaction originates in the nuclear Zeeman effect. The magnetic (hyperfine) field can be produced either within the atom itself or within the crystal via exchange interactions. The eigenvalues of the Hamiltonian are given by

$$E_m = -\frac{\mu H m_I}{I} = -g_N \mu_N H m_I. \quad (3.15)$$

$\mu_N$  is the nuclear Bohr magneton,  $\mu$  is the nuclear magnetic moment,  $I$  is the nuclear spin,  $g_N$  is the nuclear g-factor, and  $m_I$  the magnetic quantum number. Only transitions yielding  $\Delta m_I = 0, \pm 1$  are allowed. In the case of  $^{57}\text{Fe}$  - taking into account the selection rules - a sextet of transitions appears.

The splitting of the energy levels and the correlated Mössbauer spectra of the three different kinds of interaction are illustrated in Fig. 3.5 for  $^{57}\text{Fe}$ .



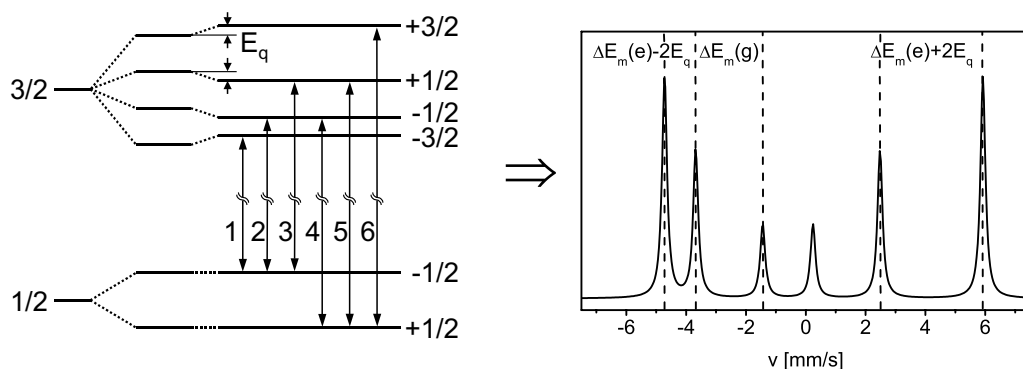


Figure 3.6: Energy splitting and corresponding conversion electron spectrum of the combined magnetic and quadrupole interaction.

### Combined magnetic and quadrupole interactions

Isomer shifts, electric field gradients and magnetic hyperfine fields may occur simultaneously and interact with each other, making the analysis of the spectra difficult. The important parameters are the nuclear moments and hyperfine field strengths. For  $^{57}\text{Fe}$ , the quadrupole moment of the state is small enough to consider the quadrupole interaction in general as a first-order perturbation of the magnetic field interaction. A schematic view of the level scheme and the spectrum is given in Figure 3.6. In the case of an axially symmetric EFG-tensor, the energy splitting can be described by [Sch91]

$$E = -g_N \mu_N H m_I + (-1)^{|m_I|+1/2} \cdot \frac{e^2 Q V_{zz}}{4} \cdot \frac{1}{2} (3 \cos^2 \beta - 1) \quad (3.16)$$

with  $\beta$  being the angle between the orientation of the magnetic field and the principal axis of the EFG-tensor.

### Intensity ratios

Apart from the analysis of the level splitting, additional information can be obtained by measuring the relative intensities of the peaks in a Mössbauer spectrum. Generally, the intensity of a transition between two sub-states of two levels depends on the appropriate Clebsch-Gordan coefficients [Con35]. These coefficients have been derived for the  $\frac{3}{2} \rightarrow \frac{1}{2}$  transitions in the isotope  $^{57}\text{Fe}$  and are summarized in Table 3.1 [Gre71].

Magnetic spectra (M1)			
Line	Transition	$\Delta m$	Intensity
L1	$-\frac{3}{2} \rightarrow -\frac{1}{2}$	+1	$I_1 = \frac{3}{8} (1 + \cos^2 \theta)$
L2	$-\frac{1}{2} \rightarrow -\frac{1}{2}$	0	$I_2 = \frac{1}{2} (1 - \cos^2 \theta)$
L3	$+\frac{1}{2} \rightarrow -\frac{1}{2}$	-1	$I_3 = \frac{1}{8} (1 + \cos^2 \theta)$
L4	$-\frac{1}{2} \rightarrow +\frac{1}{2}$	+1	$I_4 = \frac{1}{8} (1 + \cos^2 \theta)$
L5	$+\frac{1}{2} \rightarrow +\frac{1}{2}$	0	$I_5 = \frac{1}{2} (1 - \cos^2 \theta)$
L6	$+\frac{3}{2} \rightarrow +\frac{1}{2}$	-1	$I_6 = \frac{3}{8} (1 + \cos^2 \theta)$
Quadrupole spectra (M1)			
L1	$\pm\frac{1}{2} \rightarrow \pm\frac{1}{2}$		$I_1 = 2 + 3 \sin^2 \theta$
L2	$\pm\frac{3}{2} \rightarrow \pm\frac{1}{2}$		$I_2 = 3(1 + \cos^2 \theta)$

Table 3.1: Intensities of the various transitions in  $^{57}\text{Fe}$ . The angular terms are the radiation probabilities in a direction  $\theta$  to the principal axis of the magnetic field or the EFG tensor.

### 3.2.2 Conversion electron Mössbauer spectroscopy

Electromagnetic transitions having small energies show the effect of internal conversion [Dan39], as is the case for the 14.4 keV Mössbauer transition in  $^{57}\text{Fe}$  [Spi81, Sch91]. The energies and probabilities for the conversion process in  $^{57}\text{Fe}$  are summarized in Figure 3.7. In conversion electron Mössbauer spectroscopy (CEMS) only the conversion electrons emitted by the probe are used to collect the spectra. Generally, electrons are absorbed quite easily in any material (the penetration depth is, depending on the material, between 10 nm and 400 nm [Wag76]) and therefore CEMS is an ideal technique for surface analysis. To avoid absorption of the electrons in the air or in the detector window, the sample has to be placed inside the detector. In our experiments, a gas-flow proportional counter with a He + 6%CH<sub>4</sub> gas mixture was used

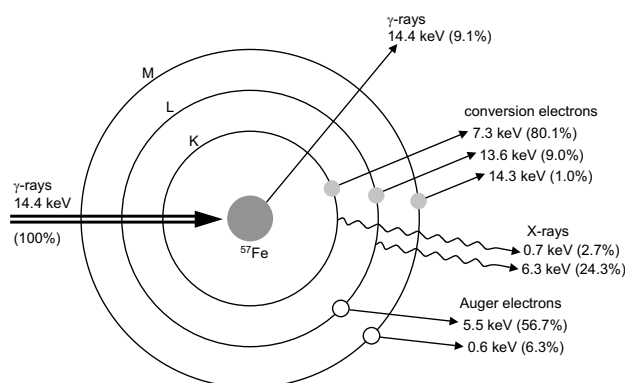


Figure 3.7: Energies and probabilities of all kinds of radiation of the internal conversion of  $^{57}\text{Fe}$ .

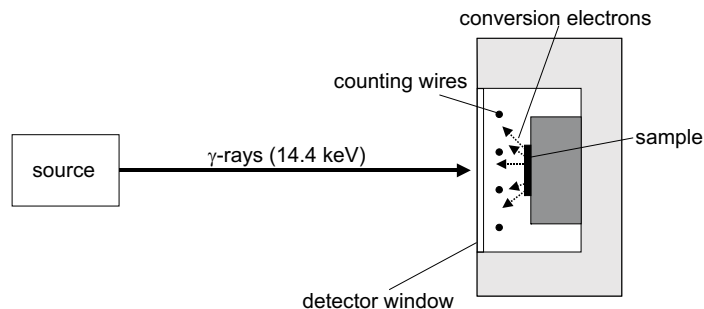


Figure 3.8: Structure of a CEMS-detector. The sample is mounted inside the detector to avoid absorption of the conversion electrons in the detector window.

[Sch91, Spi81]. The detector setup is illustrated in Figure 3.8.

In the presented experiments a  $^{57}\text{Co}$  source in a Rh-matrix with a typical activity of 1 - 2 GBq was used. The energy of the  $\gamma$ -rays was varied by moving the source by a constant acceleration drive, producing a Doppler-shifted energy of the ray. The velocity profile was controlled by a feed-back control circuit, showing a velocity error of 0.2% - 0.4%. The amplified detector signals were separated by an energy discriminator and sent to a computer system via triggered multichannel analyzer (1024 channels).

Finally, the spectra were fitted with superposed Lorentzian line shapes by minimizing the  $\chi^2$ . The hyperfine parameters (isomer shift, quadrupole splitting, magnetic hyperfine field, line intensities, line width), including the area fractions  $F_i$  of the sub-spectra and all errors, were extracted from the fit. Several sextets and typically one doublet were needed to obtain the best fit results. Usually the strongest sextet 1 corresponds to  $\alpha$ -iron, giving information about the area fraction  $F_1$ , hyperfine field  $B_{HF1}$ , isomer shift  $\delta_1$ , intensity ratio of the peaks  $I_2/I_3$ , and the peak widths. For the other sites, having smaller area fractions, all parameters (besides the area fraction, hyperfine field and quadrupole splitting) were fitted once for all spectra of the sample (see section 3.2.3) and these parameters were fixed to their average values in the final fit.

To calibrate the velocity axis, one spectrum of a 25  $\mu\text{m}$  thick  $\alpha$ -iron foil was measured, because the hyperfine parameters of  $\alpha$ -iron are well-known ( $B_{HF} = 32.9$  T,  $\Delta = 0$  mm/s). All isomer shift were correlated to the center of the calibration spectrum. Since all measurements were performed at room-temperature, an analysis of the Debye-Waller-factor was not possible. Thus the atomic fractions of the sites could not be derived by the fitted area fractions. As on the one hand the signal of  $\alpha$ -iron and the sites with a reduced number of nearest neighbors due to radiation damage was dominant ( $> 90\%$  in all except one sample) and on the other hand the main subject of this work was the study of the direction dependence of the  $\alpha$ -iron spin distribution (see section 3.2.3), this point is considered to be negligible.

The magnetic field produced by the source drive at the sample position was measured to be less than 1 Oe. This fact is of minor importance for standard CEMS analysis of thin films, because the orientation of the spins in the film plane is not measured. For MOMS this is an essential condition which has to be controlled, because the in-plane spin orientation can be affected dramatically by an in-plane component of an external magnetic field.

### 3.2.3 Magnetic orientation Mössbauer spectroscopy: geometry and analysis

Using the standard CEMS technique, as described in the previous section, it is possible to analyze the size of the hyperfine field and the electric field gradient, but concerning the directions of these quantities one can only distinguish between "out-of-plane" and "in-plane". This is sufficient for phase analyses, but generally the CEMS technique can provide more information. By breaking the symmetry of parallel directions of the incident  $\gamma$ -ray and sample normal, and taking spectra at several orientations around its normal, the in-plane hyperfine field structure of the samples can be measured. This so-called magnetic orientation Mössbauer spectroscopy (MOMS) for the measurement of magnetic anisotropy was suggested for the first time in [Mue03a, Sch02] and will be applied intensely in this thesis. As the method is only sensitive to  $^{57}\text{Fe}$ , it provides an analysis of the magnetic anisotropy for the volumes containing this isotope. Consequently, depth-sensitive anisotropy measurements of buried Fe layers or the analysis of different regions within Fe films containing sandwiched  $^{57}\text{Fe}$  marker layers are possible.

The principle of the method is the following: we start with the geometry sketched in Figure 3.8, where the incident  $\gamma$ -ray beam, the sample normal  $\mathbf{n}$  and the axis of the detector coincide. Then the sample normal  $\mathbf{n}$  and the detector (the sample is fixed inside the detector) are tilted by the angle  $\alpha$  relative to the incident  $\gamma$ -ray beam (see Fig. 3.9, small sketch). Now  $\varphi$  describes the angle between the axis around which  $\mathbf{n}$  was tilted and the  $0^\circ$  axis of the sample. CEMS spectra for various angles  $\varphi$  starting at  $0^\circ$  are now collected. Considering that the sample contains only  $\alpha$ -iron, and all  $^{57}\text{Fe}$  hyperfine field vectors are oriented in one particular in-plane direction  $\psi$  relative to  $\varphi = 0^\circ$ , by variation of  $\varphi$  also  $\theta$  will change. In this context,  $\theta$  is the angle between the incident  $\gamma$ -ray and the hyperfine field vectors. As the intensity ratio of the sextet-lines 2 and 3  $I_2/I_3$  depends on  $\theta$  (see Table 3.1), it will show a  $\varphi$ -dependence as presented in Fig. 3.10. Generalizing this example for films having  $N$  preferred hyperfine field directions  $\psi_a, \dots, \psi_N$ , the variation of  $I_2/I_3$  with  $\varphi$  is the linear combination of all  $N$  contributions. Using the equations for the  $\theta$  dependence of the  $I_2/I_3$  ratio, as presented in Table 3.1, the general equation

$$I_2/I_3(\varphi) = \sum_{i=a}^N 4c_i \cdot \frac{1 - \sin^2 \alpha \cdot \sin^2(\varphi - \psi_i)}{1 + \sin^2 \alpha \cdot \sin^2(\varphi - \psi_i)} + 4c_{op} \cdot \frac{1 - \cos^2 \alpha}{1 + \cos^2 \alpha} \quad (3.17)$$

for  $N$  different in-plane hyperfine field orientations and one out-of-plane hyperfine field vector ( $\sum c_i + c_{op} = 1$ ) can be derived by elementary vector algebra. The  $\psi_i$  are the angles of the preferred directions of the hyperfine field vectors  $B_{HF_i}$ , which denote in our case the field for  $\alpha$ -iron ( $F_1 = \text{area fraction}$ ,  $|B_{HF1}| = 32.9 \text{ T}$ ), with respect to the  $0^\circ$  axis of the sample. No other fitted sites (sextets 2 and 3 or doublets) with a reduced hyperfine field or an EFG-splitting of the level are considered in this analysis.

For all present experiments the angle  $\alpha$  was fixed to  $45^\circ$ , simplifying equation (3.17). In addition, nearly all analyzed samples showed a uniaxial anisotropy, having a second local energy minimum at  $90^\circ$  with respect to the easy axis (see MOKE analysis in chapter 4). Consequently, a restriction to two in-plane hyperfine field directions is a good approximation. These angles will be called  $\psi_a$  for the easy axis and  $\psi_b \equiv \psi_a - 90^\circ$  for the hard axis, showing the local energy minimum. The corresponding intensities are  $c_a$  and  $c_b$  and the equation used in the MOMS fits is finally

$$I_2/I_3(\varphi) = 4c_a \cdot \frac{1 - 0.5 \cdot \sin^2(\varphi - \psi_a)}{1 + 0.5 \cdot \sin^2(\varphi - \psi_a)} + 4c_b \cdot \frac{1 - 0.5 \cdot \sin^2(\varphi - \psi_b)}{1 + 0.5 \cdot \sin^2(\varphi - \psi_b)} + \frac{4}{3}c_{op}. \quad (3.18)$$

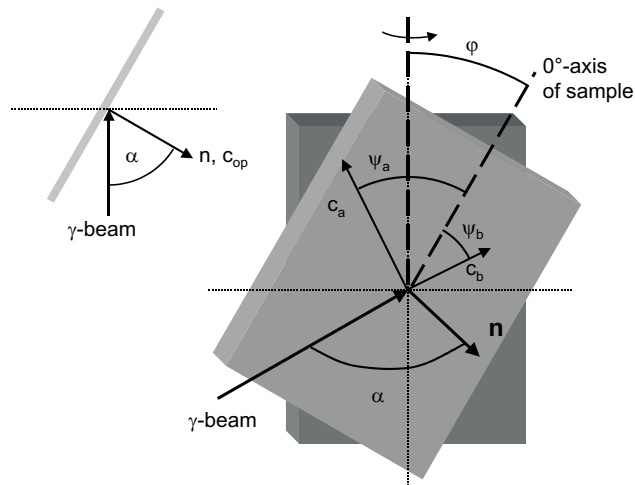


Figure 3.9: Geometry of MOMS measurements.

The geometries of the setup and all the angles used are presented in Fig. 3.9. An example of the  $\varphi$  dependence of  $I_2/I_3$  with  $\alpha = 45^\circ$  is given in Fig. 3.10 for a 75 nm thick iron film, containing a 15 nm thin  $^{57}\text{Fe}$  marker layer in the middle of the  $^{nat}\text{Fe}$  "sandwich". The film was irradiated with  $1 \times 10^{16} \text{ Xe}^+/\text{cm}^2$ , with applied mechanical stress during the implantation [Mue03a]. In Fig. 3.10 a) six spectra for several angles  $\varphi$  are shown. The variation of  $I_2/I_3(\varphi)$  can be clearly seen (see Fig. 3.10 b)), as will be discussed later.

All measured CEMS spectra were fitted as described in section 3.2.2. It was sufficient to use a combination of the following sites:

- up to 4 sextets with  $B_{HF} \approx 33 \text{ T}$ ,  $30 \text{ T}$ ,  $27 - 28 \text{ T}$  or  $20 \text{ T}$  having isomer shifts of  $\delta \approx 0 \text{ mm/s}$
- up to 2 nonmagnetic phases with quadrupole splittings of  $\Delta \approx 1.2 \text{ mm/s}$  or  $\Delta \approx 0.61 \text{ mm/s}$  and isomer shifts of  $\delta \approx 0.35 \text{ mm/s}$  or  $\delta \approx 0.2 \text{ mm/s}$
- a singlet site with an isomer shift of  $\delta \approx -0.13 \text{ mm/s}$

The 32.9 T sextet, which has an area fraction of  $> 70\%$  for all specimens besides one, corresponds to the pure  $\alpha$ -iron, used for MOMS. Because  $\alpha$ -iron has a bcc-structure, the number of neighbors in the first and the second shell is 14. The removal of one neighboring Fe atom reduces the hyperfine field at the  $^{57}\text{Fe}$  site by 3.6 T [Neu96]. In this way the sextets with reduced  $B_{HF}$  can be explained. The  $\Delta \approx 1.2 \text{ mm/s}$  doublet is a result of surface oxidation of the sample if the  $^{57}\text{Fe}$  is on top of the film, and the  $\Delta \approx 0.61 \text{ mm/s}$  doublet is an indication of iron-silicide formation at the interface with the substrate. The singlet site most probably originates from the high pressure hcp-Fe phase and was only observed in samples measured in bent condition (see section 3.5.2). All hyperfine parameters used are summarized in Table 3.2, showing the parameters found in the literature.

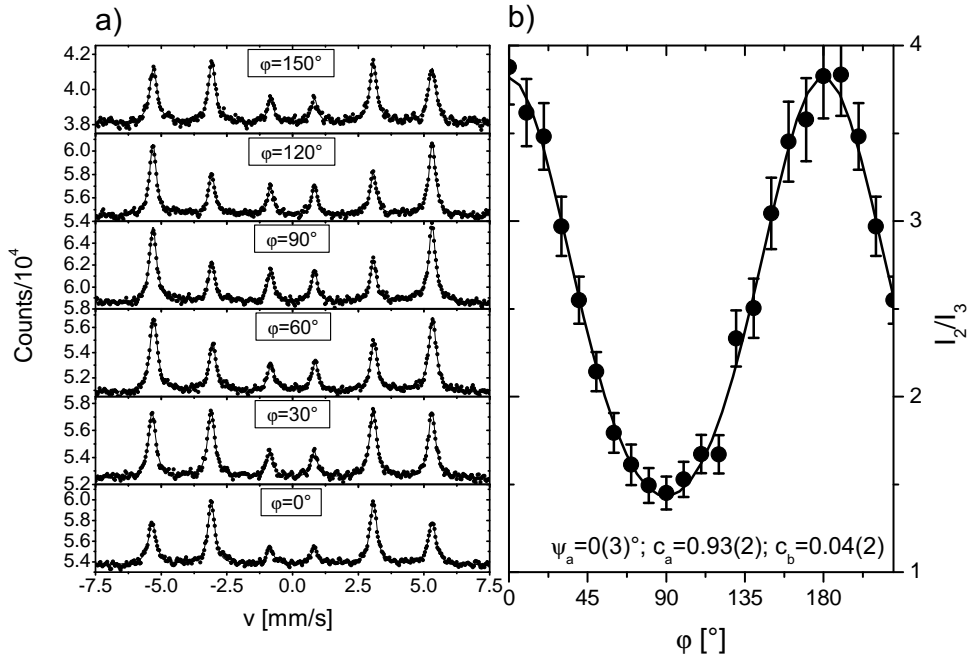


Figure 3.10: a) Mössbauer spectra showing the  $\varphi$  dependence of the ratio  $I_2/I_3$  of the Fe/ $^{57}\text{Fe}$ /Fe/Si(100) layer structure of 1-M (see section 4.2.3). b) Plot of  $I_2/I_3$  over  $\varphi$ . The solid line shows the fit using equation (3.18).

Phase	comment	$\delta$ [mm/s]	$\Delta$ [mm/s]	$B_{HF}$ [T]	Reference
$\alpha$ -Fe		0	—	32.9(1)	[Rix93, Rix95]
	depending on number of neighbors	0	—	< 32.9	[Rix93, Rix95, Neu96]
a-Fe-Si	$c_{Fe} = 16$ at%	0.119	0.653	—	[San91]
	$c_{Fe} = 17.1$ at%	0.131	0.622	—	[San91]
	$c_{Fe} = 36.7$ at%	0.204	0.545	—	[San91]
	$c_{Fe} = 38.4$ at%	0.229	0.478	—	[San91]
Fe-Si	not resolved phase	0.26	0.62	—	[Des99]
$\text{Fe}_2\text{O}_3$	amorphous phase	0.33	1.13	—	[Hei79]
FeO	not resolved phase	no value	no value	—	[Bay83]
$\epsilon$ -Fe	—	-0.11	—	—	[Tay91]

Table 3.2: Hyperfine parameters  $\delta$ ,  $\Delta$  and  $B_{HF}$  and references of the Fe phases, used to fit the spectra.

Based on the fitted hyperfine parameters, the intensity ratios of the pure  $\alpha$ -iron phase (sextet 1) was used to perform the MOMS analysis. The corresponding  $I_2/I_3$  ratios were plotted versus  $\varphi$  and fitted by equation (3.18).  $I_2/I_3$  of the sextets 2 and 3, having a reduced number of neighbors, were set manually to the same value as obtained for sextet 1. An example of the experimental results is given in Figure 3.10 b) where the symbols are the measured ratios and the solid line is the fit.

### 3.3 Comparison of MOMS and MOKE

Before MOMS is used for the analysis of magnetic anisotropy, several of its important properties in comparison with MOKE will be illustrated.

In CEMS the hyperfine field of only one isotope (in our case  $^{57}\text{Fe}$ ) is taken into account. The measurement depth can be adjusted by changing the deposition or implantation depth of the probe isotope. As the conversion electrons are absorbed in the top layer, the signal intensity decreases exponentially with increasing depth and CEMS is consequently restricted to the uppermost 150 nm of the sample. The MOKE method only analyzes the properties of the illuminated sample area and the hysteresis loop of this spot is measured by sweeping an external magnetic saturation field (see section 2.1.1). The restriction to the illuminated area limits the measurement depth to the absorption length  $l_\alpha$  of the laser in the film material.  $l_\alpha$  is given by the reciprocal value of the absorption coefficient  $\alpha$ :

$$l_\alpha = \frac{\lambda_{laser}}{4\pi k} = \frac{1}{\alpha}. \quad (3.19)$$

$\lambda_{laser}$  is the wavelength of the incident laser light and  $k$  is the extinction coefficient of the refractive index  $\mathbf{n} = n + ik$ . For  $\lambda_{laser} = 632.8$  nm and, consequently,  $k_{Fe} = 3.07$  [Joh74], the absorption length is  $l_\alpha \approx 16.4$  nm. Therefore MOKE is only sensitive to the very surface of the specimen. Nevertheless, a 75 nm thick film is supposed to have a uniform domain structure from the surface to the substrate, because it is in the range of the "thin film limit" [Hub00].

In addition to these differences in the measurement volumes, the method of measuring the magnetic anisotropy is also different. MOMS is sensitive to the static spin distribution of the sample. Due to the Fermi contact interaction (see section 2.1.3), the direction of highest spin intensity in a magnetically anisotropic specimen is in  $180^\circ$  symmetry to the easy axis of magnetization. By means of MOKE, full hysteresis loops are measured and the information about the anisotropy is extracted from the change of the magnetization state.

To illustrate the different properties of MOMS and MOKE, measurements were performed on two samples, both  $10 \times 7$  mm<sup>2</sup> in size. One was showing strong magnetic anisotropy, the other was nearly isotropic. The first sample, called 2-S (see section 4.2.3), was a natural iron film of 55 nm thickness, capped with a 15 nm  $^{57}\text{Fe}$  marker layer and another 5 nm  $^{nat}\text{Fe}$  layer to prevent the  $^{57}\text{Fe}$  from oxidation. The  $^{nat}\text{Fe}$  was deposited by electron-beam evaporation and the  $^{57}\text{Fe}$  by an effusion-cell, and this film was in its as-deposited state. The second sample was a pure  $^{57}\text{Fe}$  film (sample P), 78 nm thick and irradiated with  $1 \times 10^{16}$  Xe<sup>+</sup>/cm<sup>2</sup> at room-temperature with an external magnetic field of 104 Oe applied parallel to the long axis of the sample.

The different layer structures of both films led to different results of the MOKE analysis, as

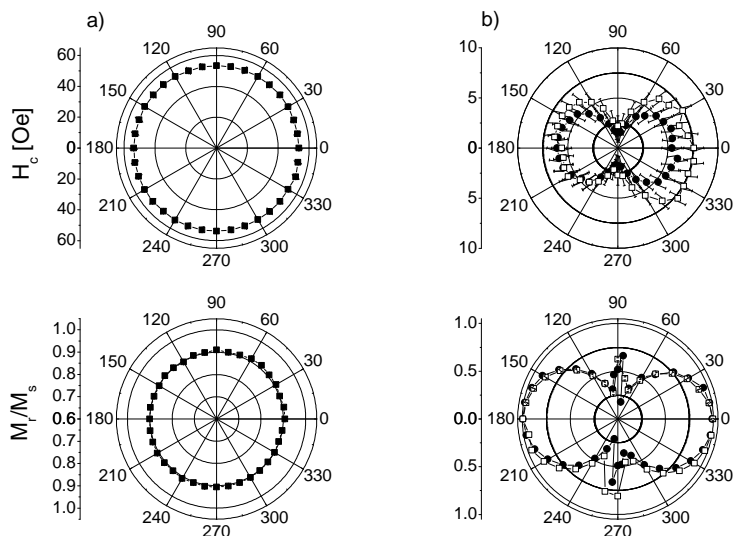


Figure 3.11: MOKE polar plots of  $M_r/M_s$  and  $H_c$  for samples: a) 2-S (as-deposited) and b) P as-deposited (open squares) and implanted (solid circles).

illustrated in Figure 3.11. While 2-S (a) shows a completely isotropic coercivity and relative remanence after deposition, P (b) is strongly anisotropic when as-deposited (open squares) or ion irradiated (solid circles).

After the MOKE analysis a saturation field (300 Oe) was applied in the direction  $\chi$  relative to the long axis of the samples. This external field was then released to leave the specimens in remanent magnetization state. After this treatment, MOMS ( $\alpha = 45^\circ$ ) was measured for various angles  $\varphi$ . This procedure - sample magnetization and MOMS measurement - was repeated for various angles  $\chi$ . According to the discussion at the beginning of this section, an orientation of the preferred hyperfine field direction along the remanence axis  $\chi$  is expected for the isotropic sample 2-S. This sample shows no free energy minimum for the in-plane magnetization direction. In the anisotropic specimen P the spins should be aligned along the easy axis of magnetization, independent of the direction of the applied magnetic field  $\chi$ .

The MOMS results of these measurements are presented in Fig. 3.12 and the fit parameters are summarized in Table 3.3. The measured values of  $\psi_a$  agree in nearly all the cases with the expectations. For sample 2-S the measured value always agrees with the angle  $\chi$ , the only exception being the magnetization direction  $\chi = 100^\circ$ . The values  $c_a \approx 0.75(2)$ ,  $c_b \approx 0.18(2)$  and  $c_{op} \approx 0.07(2)$ , show only small variations for different  $\chi$ .

For sample P in all the cases  $\psi_a = 0^\circ$ , as it was expected. At the angles  $\chi = 70^\circ - 90^\circ$  the ratio  $c_a/c_b$  is significantly smaller than at the other angles, as shown in Table 3.3. The MOKE hysteresis loops are nearly square-shaped with high remanence at angles between  $85^\circ$  and  $95^\circ$ .

To sum up, the expected results are observed with only one exception in specimen 2-S.

A similar way of measuring the easy axis was proposed by Richter and Woods [Ric91, Woo02], who used a vibrating sample magnetometer (VSM) for this measurement.



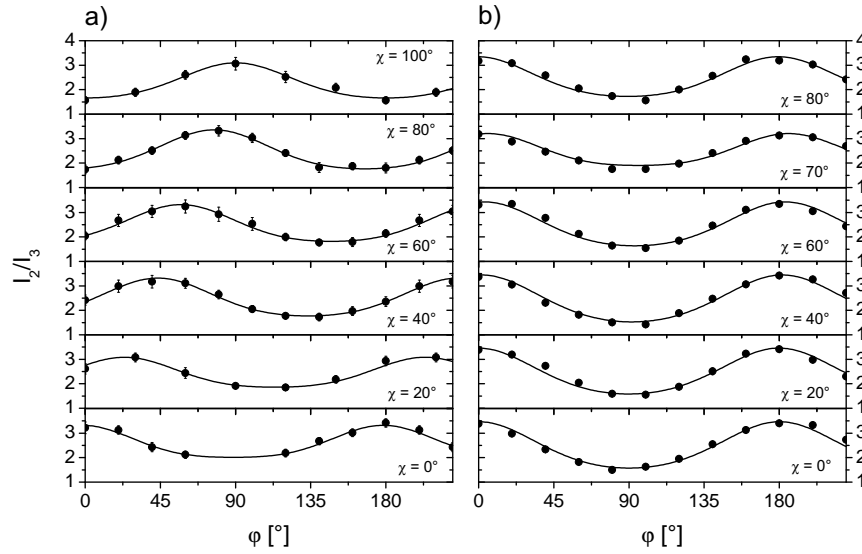


Figure 3.12: MOMS graphs for samples 2-S and P, being in remanence state in different directions  $\chi$ . In sample 2-S (a)  $\psi_a$  follows the remanence direction  $\chi$ , while P (b) always shows a parallel alignment of spins and easy axis direction.

Sample	$\chi$ [°]	MOMS fit				Exp.
		$\psi_a$ [°]	$c_a$ [%]	$c_b$ [%]	$c_{op}$ [%]	$c_{op}$ [%]
2-S	0	-2(4)	74(2)	26(2)	0(0)	5(5)
	20	24(4)	66(2)	19(2)	15(2)	7(7)
	40	43(4)	74(2)	17(2)	9(2)	0(3)
	60	57(4)	75(2)	18(2)	7(2)	1(5)
	80	77(4)	76(2)	16(2)	8(2)	10(7)
	100	90(5)	66(3)	12(3)	22(4)	5(5)
P	0	0(4)	80(3)	9(3)	11(4)	10(3)
	20	0(4)	80(3)	9(3)	11(4)	6(2)
	40	2(4)	79(3)	8(3)	13(4)	10(2)
	60	3(4)	79(3)	13(3)	8(4)	8(2)
	70	5(5)	70(4)	22(4)	8(5)	6(1)
	80	0(4)	75(3)	15(3)	10(4)	7(2)
	90	0(4)	65(2)	16(2)	19(2)	11(3)

Table 3.3: Parameters of the  $\chi$ -dependent MOMS measurement of samples 2-S and P. The values in the last two columns show the comparison of the out of plane component of the hyperfine field as resulting from the fit and as measured by CEMS with perpendicular incidence.

### 3.4 Other measurement techniques

In this section the techniques X-ray diffraction, extended X-ray absorption fine structure spectroscopy and Rutherford backscattering spectroscopy are described briefly. In this project also secondary ion mass spectroscopy were used, but will not be discussed here.

#### 3.4.1 X-ray diffraction

Since interatomic distances in a solid are of the order of  $10^{-10}$  m, an electromagnetic wave with an energy of  $hc/\lambda = 10^4$  eV ( $\lambda = 10^{-10}$  m) is an ideal probe to analyze the crystallographic structure. There are different ways of explaining the scattering process of X-rays by a perfect lattice [Ash76]. The Bragg relation is the most famous description for a constructive interference of X-rays with wavelength  $\lambda$  and incidence angle  $\theta$ , being reflected at lattice planes with distance  $d$ :

$$2d \sin \theta = n\lambda. \quad (3.20)$$

The lattice constant  $a$  can be derived for a cubic crystal using the Miller indices  $(hkl)$  [Ash76] of the planes:

$$a = \frac{\lambda}{2 \sin \theta} \sqrt{h^2 + k^2 + l^2}. \quad (3.21)$$

All XRD spectra presented in this thesis have been recorded with a *Bruker AXS D8 Advance* diffractometer, working with a Cu-K $_{\alpha}$  source ( $\lambda = 1.54$  Å) and a LiF single-crystal monochromator on the diffracted beam. For the data collection various geometries were used. The Bragg-Brentano ( $\theta - 2\theta$ ) geometry was employed to obtain information about the out-of-plane texture of the films. Since the films, deposited by electron-beam evaporation (see chapter 4), had a very weak texture, additionally an analysis with grazing incident X-ray (GIXRD) was performed, which has several advantages. First of all, the penetration depth of the X-ray is smaller, resulting in higher intensities for the measured peaks. Second, the geometry does not restrict the measurement to the grains oriented out-of-plane. In this way, it is possible to obtain peaks of various lattice planes. Fig. 3.13 shows the two basic geometries, used in this work. Depending on the grazing angle  $\alpha$  of the X-ray, the measured peak positions are slightly shifted towards higher diffraction angles. This effect was reported by Takayama et al. [Tak90] and can be corrected by the equation

$$\Delta(2\theta) \approx \alpha - (\alpha^2 - \alpha_c^2)^{1/2}. \quad (3.22)$$

$\alpha_c$  is the critical angle of the material, which is  $0.384^\circ$  for iron.

In chapter 6 also rocking curves and  $\varphi$ -scan measurements are presented. For both geometries, the  $2\theta$ -angle of one certain line is adjusted and the angle  $\theta$  (rocking curve) or the in-plane orientation of the specimen  $\varphi$  ( $\varphi$ -scan) are changed.

#### Stress analysis

In addition to the advantages of the GIXRD geometry discussed above, the variation of the angle  $\psi$  (see Figure 3.13) for the different peaks provides information about the in-plane strain of the specimen surface, from which the stress can be derived. This kind of analysis is known as the  $\sin^2\psi$ -method and is performed for a fixed  $(hkl)$  peak in the asymmetric  $\theta - 2\theta$  geometry.

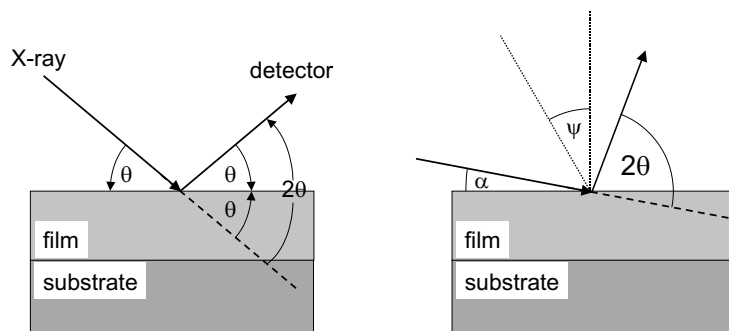


Figure 3.13: Bragg-Brentano or  $\theta - 2\theta$  (left) and grazing incidence (right) geometry of an X-ray diffraction experiment.

The basic theory is described for instance in [Pre86] and it will be shortly summarized here. The angle  $\psi$  is the angle between the surface normal of the sample and the incident and diffracted beam bisector. According to this definition, it is also the angle between the normal to the diffracting lattice planes and the sample surface. Considering Bragg's law (3.20), the angle of a diffracted beam  $2\theta$  depends on the lattice parameter  $d$  of the irradiated grain in the surface. If in-plane stress is present in the surface layer, it is obvious that the lattice parameter depends on the measurement direction  $\psi$ . If for example  $\psi$  is set to  $0^\circ$  as in  $\theta - 2\theta$  geometry, the lattice parameter  $d_\perp$  perpendicular to the film surface is measured. The only influence of an in-plane tensile stress on this distance is a reduction of  $d_\perp$  as a result of the Poisson's ratio contraction. For large  $\psi$ , the orientation of the investigated lattice parameter is no longer perpendicular to the surface and a component of the in-plane tension will act to expand the distance between the observed planes (see Fig. 3.14). The accuracy of this analysis in the standard-geometry, using an asymmetric  $\theta - 2\theta$  scan, strongly depends on the diffraction angle chosen. Usually,  $2\theta$  is larger than  $120^\circ$  and the lattice parameter for one  $(hkl)$  direction is measured for several angles  $\psi$ . Thus, the  $\sin^2 \psi$  method is limited to thick samples, showing an acceptable peak intensity also at high diffraction angles.

The equation which is used to derive the stress in the sample is

$$\frac{d_{\varphi\psi} - d_0}{d_0} = \left[ \left( \frac{1 + \nu}{E} \right)_{(hkl)} \sigma_\varphi \sin^2 \psi \right] - \left[ \left( \frac{\nu}{E} \right)_{(hkl)} (\sigma_1 + \sigma_2) \right]. \quad (3.23)$$

$d_{\varphi\psi}$  is the measured lattice parameter in-plane in direction  $\varphi$  under angle  $\psi$ ,  $d_0$  is the theoretical lattice parameter of the unstrained lattice,  $\sigma_\varphi$  is the in-plane stress in direction  $\varphi$ ,  $\sigma_1$  and  $\sigma_2$  are the principal in-plane stresses,  $\nu$  is the Poisson ratio and  $E$  is the Young modulus for the crystallographic direction normal to the lattice planes in which the strain is measured. The unstrained lattice parameter  $d_0$  cannot be measured, but is usually extracted from the fit of the measured data [Pre86].

For thin films it is appropriate to use the GIXRD geometry for a similar analysis [Jao01]. In this geometry also the angle  $\psi$  is varied, but for each angle, a different crystallographic direction is measured and the stress analysis is performed with the lattice constants  $d_{\varphi\psi}$  derived from the

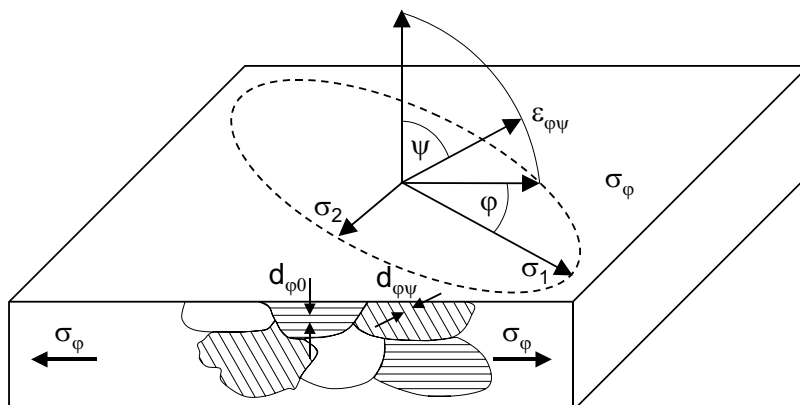


Figure 3.14: Influence of in-plane stress on crystallites, oriented in different directions.

measured peak positions with the correlated Miller indices. Figure 3.15 shows three peaks of a GIXRD ( $\alpha = 2^\circ$ ) measurement of a bcc iron film, irradiated with  $5 \times 10^{16} \text{ Xe}^+/\text{cm}^2$ , as it will be presented in section 4.1.3 (a) Fe(110), b) Fe(200) and c) Fe(211)). The corresponding fits were made with a symmetric Pearson VII line-shape. In this example the angles  $\psi = \theta - \alpha$  are  $\psi_{110} = 20.2^\circ$ ,  $\psi_{200} = 30.3^\circ$  and  $\psi_{211} = 38.9^\circ$ .

As a consequence of the  $(hkl)$  dependence of the Poisson ratio and the Young modulus, these parameters have to be derived separately for the different  $(hkl)$ . A more detailed description of the derivation of  $E$  and  $\nu$  for various  $(hkl)$  is given by Sander or Nye [San99, Nye85].

### 3.4.2 Extended X-ray absorption fine structure

In the last decades properties of solids became accessible through the use of synchrotron radiation [IFF92, Ste88]. Several X-ray techniques such as XMCD, EXAFS, XANES, XRD or Mössbauer spectroscopy were developed or improved exploiting the high intensity and the continuous spectrum of synchrotron light. The extended X-ray absorption fine structure (EXAFS) concerns the oscillations of the absorption coefficient as a function of the X-ray photon energy. It occurs when the energy of the incident photons exceeds the absorption edge of the element studied. These oscillations contain information about the short range order of the atoms.

Generally, the intensity of X-rays is reduced by transmission through a material. Considering a material of thickness  $t$ , the absorption of the layer is expressed by the equation

$$I_2(E) = I_1(E)e^{-\mu(E)t}. \quad (3.24)$$

$I_1(E)$  is the original intensity,  $I_2(E)$  is the intensity after transmission through the material and  $\mu(E)$  is the linear absorption coefficient. At the binding energies of inner shells - characteristic of each element - the absorption coefficient increases strongly. This energy is called absorption edge. At the so-called  $L_1$ ,  $L_2$  or  $L_3$  edges of the spectrum, a  $2s$ ,  $2p_{1/2}$  or  $2p_{3/2}$ -electron is emitted. For higher energies,  $\mu$  shows oscillations (see Fig. 3.16) which originate from the interference

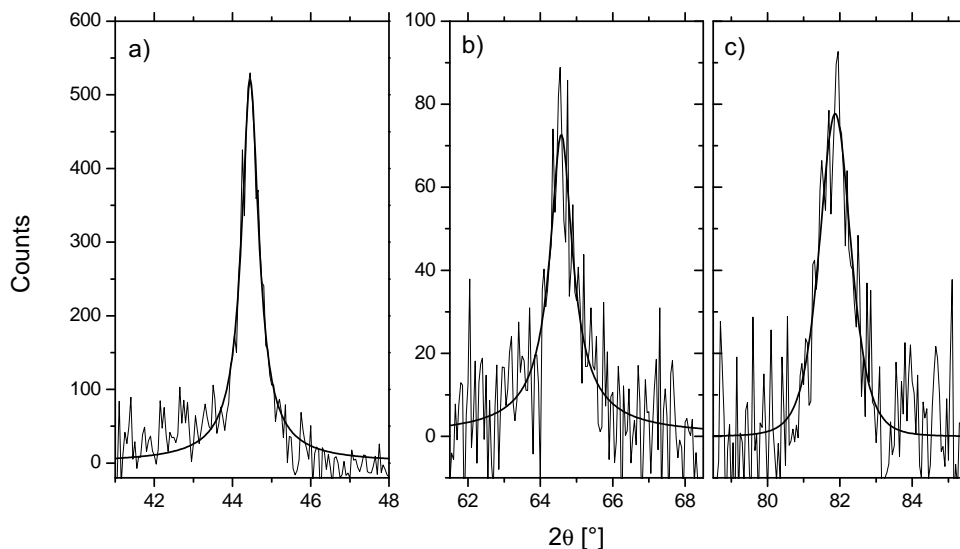


Figure 3.15: Example for the fit of the three main GIXRD reflections of bcc iron: a) Fe(110), b) Fe(200) and c) Fe(211). The fits were done with symmetric Pearson VII line shapes.

of the photoelectrons emitted and scattered at neighborly atoms. Taking  $\mu_0$  as the absorption coefficient for an atom without neighbors, constructive interference increases the probability to find the photoelectron outside the absorbing atom ( $\mu < \mu_0$ ) and destructive interference diminishes this probability ( $\mu > \mu_0$ ). Hence the distance and number of neighbors, and the disorder of the material are correlated to the periodicity and amplitude of the oscillations of the absorption coefficient (see Fig. 3.16). The oscillations of  $\mu$  directly result in the EXAFS-spectrum  $\chi(E)$  by normalizing the oscillatory part of  $\mu$  above the edge [Say88]

$$\chi(E) = [\mu(E) - \mu_0(E)] / \Delta\mu_0, \quad (3.25)$$

where  $\Delta\mu_0$  is typically the magnitude of the jump at the absorption edge. Conventionally,  $\chi$  is defined with respect not to the photon energy  $E$ , but to the photon momentum  $k$  and can be expressed by the equation [Say71]

$$\chi(k) = \sum_i A(k)_i N_i \frac{\sin[2kR_i + \delta_i(k)]}{R_i^2} \cdot e^{-\frac{2R_i}{\eta}} e^{-2k^2\sigma_i^2}. \quad (3.26)$$

The index  $i$  refers to the atomic shell,  $N_i$  denotes the coordination numbers,  $R_i$  the interatomic distances,  $A_i$  the scattering amplitudes,  $\delta_i(k)$  are phase shifts,  $\eta$  is the EXAFS mean free path and  $\sigma_i$  are the distribution widths of the interatomic bond lengths. To isolate the contributions of the parameters of each shell, a Fourier transform (FT) of the weighted spectrum  $\chi(k) \cdot k^n$  (see Fig. 3.16) is performed. In the FT, each shell is represented by a peak. By choosing a certain contribution via setting a window, the shell parameters  $N_i$ ,  $R_i$  and  $\sigma_i$  can be analyzed with the

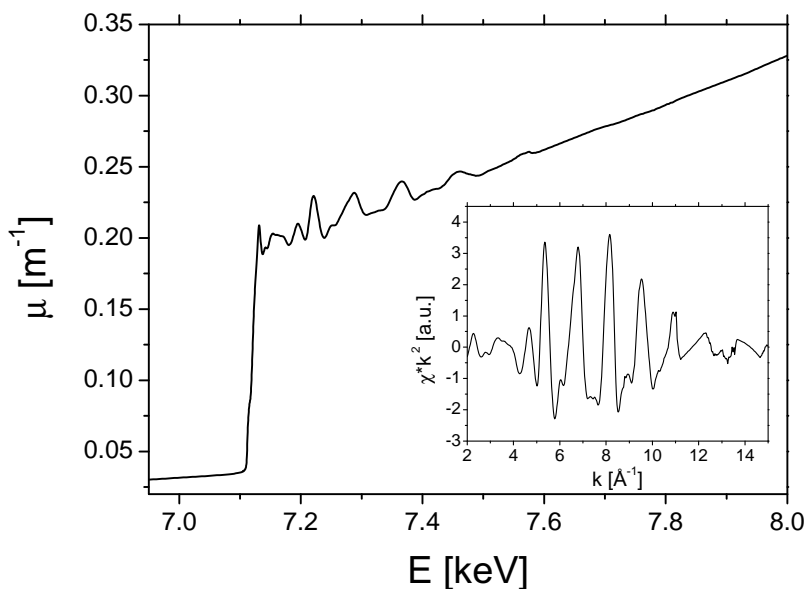


Figure 3.16:  $\mu$  and  $\chi \cdot k^2$  graphs of an EXAFS measurement at the Fe- $K_\alpha$  edge of a 75 nm thick Fe film.

back Fourier transform (BFT) of only this part of the FT spectrum. The quantities  $A_i$  and  $\delta_i$  enter as initial parameters obtained from a calibration sample. A more detailed description of the theory and analysis of EXAFS can be found in [Len92, Ste88, Car02].

The experiments discussed in this thesis were performed at the BM29 beam-line [Fil03] at the European synchrotron radiation facility (ESRF) in Grenoble. The X-ray energy was selected by a Si(111) double crystal monochromator and the data were collected at room-temperature in the energy range 6.9 - 8.0 keV. The step width was constant in the  $k$ -space. The EXAFS spectra were collected in backscattering geometry, where the emitted photoelectrons are detected (total electron yield mode), and not in transmission geometry, where the incident and the transmitted X-ray intensities are compared. Because the emitted electrons of the backscattering geometry are absorbed by the specimen, this setup is sensitive only to the uppermost  $\approx 100$  nm of the surface [Ela88].

The data analysis was performed with the *VIPER* software [Kle02, Kle01], using weighted cubic spline functions to simulate  $\mu_0$ . The FT was performed in the region  $2 \text{ \AA}^{-1} < k < 15 \text{ \AA}^{-1}$  (see Fig. 3.16, small part), using a  $k^2$  weight for  $\chi$  and a Gaussian window  $W(k)$  centered at  $\bar{k} = 8.5 \text{ \AA}^{-1}$ . The distance of the first and the second shell of the iron differs by less than 14% (1. shell:  $R_1 = 2.48 \text{ \AA}$ , 2. shell:  $R_2 = 2.87 \text{ \AA}$ ), resulting in a strong overlap of the two peaks in the FT. Thus it was not possible to create two separate files for amplitude and phase of the two shells on the basis of the calibration sample. This problem was solved [Jao01] by the simulation and subsequent fit of the calibration sample with the programs *FEFF 8.10* and *FEFFIT 2.55* and the separate extraction of amplitude and phase files for the two shells with the help of

*VIPER*. On the basis of these amplitude and phase files the BFT was performed. The third, fourth and fifth shell were not included in the fitting, because they contained multiple scattering signals. As the Debye-Waller-factor and the number of neighbors were strongly correlated,  $\sigma$  was fixed for all fits of the BFT. For a separate analysis of  $\sigma$  and  $N_i$  a temperature-dependent measurement would be necessary. Summarizing, all changes in disorder and in the number of neighbors directly result in a variation of  $N_i$ . The distance ratio of the first and the second shell was constant in all fits.

### 3.4.3 Rutherford backscattering spectroscopy

Rutherford backscattering spectroscopy (RBS) is an analytical ion-beam method, based on the detection of light ions such as  $H^+$ ,  $He^+$  or  $He^{++}$ , elastically backscattered from the Coulomb potential of heavy ions. The energy of the backscattered ions depends on the original energy  $E_0$ , the depth of the scattering nucleus  $x$ , the mass of the scattering nucleus  $M_2$  and the scattering angle which is the angle between incident beam and detector  $\Theta$ . From the energy spectrum of the detected light ions, information about the element distribution and stoichiometry can be obtained without destroying the specimen. Since this technique is described in great detail in the scientific literature [Chu78, Lea95] only a brief overview will be given here.

Considering the laboratory system as shown in Fig. 3.17, the energy  $E_1$  of the backscattered ion at the surface is proportional to the incidence energy  $E_0$

$$E_1 = K \cdot E_0. \quad (3.27)$$

$K$  is called the kinematic factor and only depends on the masses of the projectile  $M_1$  and the probe atom  $M_2$  and on the scattering angle  $\Theta$ . In the laboratory system,  $K$  is [Chu78]:

$$K = \left( \frac{\sqrt{1 - ((M_1/M_2) \sin \Theta)^2} + (M_1/M_2) \cos \Theta}{1 + (M_1/M_2)} \right)^2 \leq 1. \quad (3.28)$$

The depth sensitivity of RBS is based on the energy loss of the projectiles before and after the scattering process at depth  $x$ . Therefore, the energy of the backscattered ions can be described by

$$E_2 = K (E_0 - \Delta E(x)) - \Delta E(x / \cos \Theta). \quad (3.29)$$

The energy losses  $\Delta E(x)$  and  $\Delta E(x / \cos \Theta)$  can be derived with the help of the stopping powers of the material [Zie99]. The probability of a projectile with energy  $E$ , mass  $M_1$  and nuclear

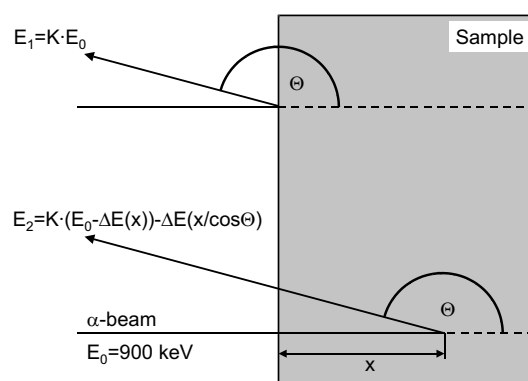


Figure 3.17: Energies in a scatter process at the sample surface and at the depth  $x$ .

charge  $Z_1$  to be scattered by the angle  $\Theta$  is given by the Rutherford backscattering yield [Rut11]:

$$\frac{d\sigma}{d\Omega} = \left( \frac{Z_1 Z_2 e^2}{16\pi\epsilon_0 E} \right)^2 \frac{4}{\sin^4 \Theta} \frac{\left[ \sqrt{1 - \left( \frac{M_1}{M_2} \sin \Theta \right)^2} + \cos \Theta \right]}{\sqrt{1 - \left( \frac{M_1}{M_2} \sin \Theta \right)^2}}. \quad (3.30)$$

The reduction of the energy with increasing depth and consequently the increasing backscattering yield can be recognized in the RBS spectra of a 75 nm thick Fe films deposited on Si, irradiated with various xenon fluences (see Figure 3.18 a)). Three different signals are apparent: the signal of the Fe film, as rising at about 690 keV, the Si substrate at 430 keV, and the Xe atoms, showing a Gaussian distribution with a tail inside the film around 750 keV. Figure 3.18 b) shows the concentration profiles, derived by the *WiNDF* program [Bar97, Bar98], which was used for all analyses. With increasing Xe fluence a decrease in the iron yield and concentration can be observed.

The scale of the depth profile is the areal density  $(Nt)_{film}$  in units of  $10^{15}/\text{cm}^2$ , and it can be transformed to the physical film thickness  $t$  in nm when the atomic density  $N_{film}$  of the film is known:

$$t = \frac{(Nt)_{film}}{N_{film}}. \quad (3.31)$$

$N_{film}$  can be found in [Tes95] or derived by  $N_{film} = \rho_{film} \cdot N_0/M$ , where  $\rho_{film}$  and  $M$  are the density and the molecular weight of the film material and  $N_0$  is Avogadro's number. For natural

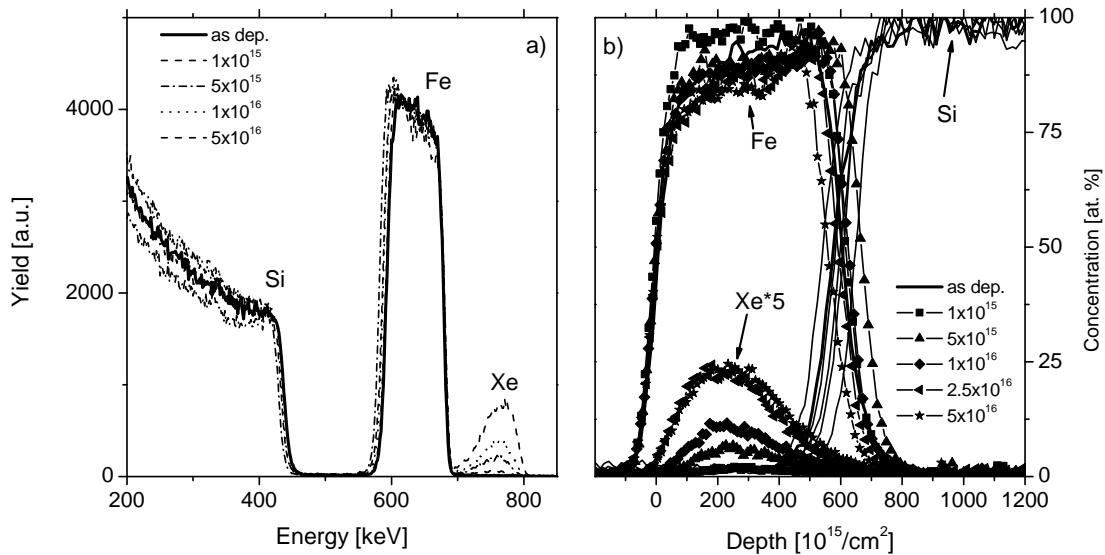


Figure 3.18: a) RBS spectra of 75 nm thick iron films implanted with various fluences of 200 keV  $\text{Xe}^+$  ions. b) Depth profiles of the irradiated films.



iron films  $N_{Fe} = 8.44 \times 10^{22}/\text{cm}^3$  and thus the areal density of  $100 \times 10^{15}/\text{cm}^2$  is equivalent to the physical thickness of  $t = 11.8$  nm.

The present experiments were performed at the R-30 beam-line of the Göttingen ion implanter IONAS [Uhr85], using a 900 keV beam of  $\alpha$ -particles. The depth resolution is limited by the energy resolution of the detector (typically 12.5 keV in the used setup), the energy distribution of the projectile beam (50 - 100 eV as measured for protons [Uhr85]), and the energy straggling of the  $\alpha$ -particles.

## 3.5 Sample preparation and treatment

### 3.5.1 Sample preparation

The films were deposited by different methods and in different chambers. The  $^{57}\text{Fe}/^{nat}\text{Fe}$  films used for the experiments described in chapter 4 were prepared in a UHV chamber [Har00], where the  $^{nat}\text{Fe}$  was deposited by electron-beam evaporation and the  $^{57}\text{Fe}$  marker layers by an effusion-cell. As both deposition systems were mounted in the same chamber, the films were prepared without intermediate air exposition. By means of a cryogenic pump the chamber was evacuated to a base pressure  $\leq 4 \times 10^{-8}$  mbar before the deposition. The large distance between sample and evaporator (40 cm for the electron-beam system and 20 cm for the effusion-cell) enabled a homogeneous film thickness, as controlled online by a quartz oscillator (electron-beam evaporator) or a flux meter (effusion-cell).

The films used in chapter 6 were deposited by pulsed laser deposition (PLD) at the Institut für Materialphysik, Universität Göttingen, using the chamber and laser described in [Kre97, Wei02]. The  $^{nat}\text{Fe}$  or  $^{57}\text{Fe}$  target was irradiated by a Kr-F excimer laser ( $\lambda = 248$  nm, pulse duration  $\tau = 30$  ns) under an angle of  $45^\circ$  and the evaporated material was deposited on the substrate at a distance of about 6 cm. PLD films are known to be usually thicker in the middle than at the edges. To improve this homogeneity the substrate was rotated during deposition and the laser plume was arranged pointing slightly out of the center of the sample. The deposition rate was controlled by a calibration sample to be 85 nm/25002 pulses. The base pressure in the deposition chamber was  $< 1 \times 10^{-9}$  mbar.

Most specimens were prepared on Si(100) or SiO<sub>2</sub> substrates, cut from large wafers by a diamond cutter and ultrasonically cleaned in acetone before being mounted in the deposition chamber. The standard geometry of the films was  $10 \times 7$  mm<sup>2</sup>. For the experiments discussed in chapter 4.2, the substrate size was  $40 \times 15$  mm<sup>2</sup> and the film was deposited in the center with a mask covering the rest of the substrate (see Fig. 3.19). The large substrate allowed for a homogeneous bending of the film, as will be presented in section 3.5.2. The PLD films were deposited on MgO(100) or Si(100) substrates,  $10 \times 10$  mm<sup>2</sup> in size (see chapter 6).

### 3.5.2 Sample bending

To induce an external mechanical stress in the film in a controlled way, some of the substrates had to be bent. For this purpose a special sample holder,  $50 \times 20$  mm<sup>2</sup> size with a 2 mm high blade in the middle, was manufactured. With the help of two steel bars, fixed at both ends of the substrate, a well defined curvature was achieved in the film. The curvature was controlled by a mechanical surface profilometer (*DEKTAK<sup>3</sup> ST*, *Veeco Instruments Inc.*), pulling a diamond tip

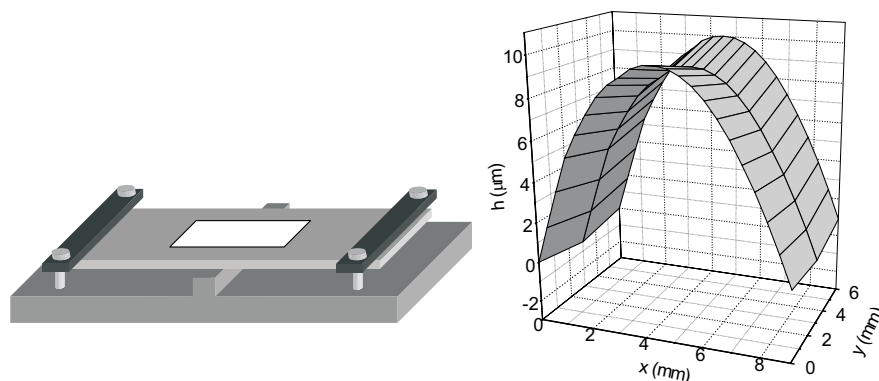


Figure 3.19: Left side: Sample, bent on the sample holder. The typical curvature of the surface was 1/m. Right side: Image of the sample surface, obtained by three scans at different places of the film by mechanical surface profilometry.

(diameter: 1  $\mu\text{m}$ ) with a weak force over the surface of the film. Figure 3.19 shows the sample mounted on the holder together with a surface profile. The stress  $\sigma$  induced in the film can be derived by considering Hooke's law for elastic continuum mechanics

$$\frac{\Delta l}{l} = \frac{\sigma}{E}. \quad (3.32)$$

$\Delta l$  is the elongation of the film with respect to the neutral fiber in the middle of the substrate and  $E$  is the Young modulus of the polycrystalline iron film [Ber70]. The well known Stoney-equation [Sto09] cannot be applied to the present treatment because it determines the stress (for instance after deposition) in a film by measuring the deformation of its substrate. One can imagine that the stress in a thin film, necessary to deform the substrate (this is usually several thousand times as thick as the film itself) must be very large. However, the force needed to elongate a 75 nm thick film by some percent of its length is much smaller.

For bulk iron the Young modulus is  $E = 216 \text{ GPa}$  [Ber70] and this value is somewhat lower for polycrystalline films [Lee94]. With the help of elementary geometry and knowledge about the thickness of the film 75(5) nm, the thickness of the substrate 525(35)  $\mu\text{m}$ , and the bending radius at the surface  $R = 1.00(5) \text{ m}$ , the film stress can be derived by equation (3.32). Since the elongation at the top and at the interface of the film differ by just 0.03%,  $\Delta l$  can be considered equal for both places. Using  $\Delta l/l = 2.63(22) \times 10^{-4}$  results in a stress of  $\sigma = 56.7(57) \text{ MPa}$  assuming a 10% error of the Young modulus.

### 3.5.3 Sample irradiation

The xenon, krypton, neon and iron irradiations of the films were performed at the Göttingen ion implanter IONAS [Uhr85] at the L15 beam-line. All irradiations were performed at room-

temperature because the irradiation temperature proved to play a minor role in the magnetic behavior of nickel films [Zha01]. Additionally, a large change in temperature possibly modifies the stress applied in the samples which were irradiated in bent condition. The implantation chamber [Cor89, Har95] was evacuated by a turbo molecular pump, supported by a liquid nitrogen cooling trap to achieve a pressure of  $1 \times 10^{-7}$  mbar during implantation. The irradiated area was  $10 \times 10$  mm<sup>2</sup>, as fixed by an aperture with a square hole of this size. To make sure that the ions are spread homogeneously over the film area, an electric x-y sweeping system was used, controlled by a four-sector beam monitor.

The ion energy was fixed in all the cases to adjust the projected range  $R_p$  of 33(2) nm, as determined by *SRIM2003* simulations [Bie80, Zie99, SRI03] and controlled by RBS after the irradiation. This penetration depth limited the implanted ions within the film. Interface mixing effects were minimized in this way and, additionally, this energy was found to result in the largest magnetic texture effect.

## Chapter 4

# Results for electron-beam deposited films

In this chapter the changes in the magnetic and structural properties of electron-beam deposited films by ion irradiation are considered, investigating various external irradiation parameters.

In section 4.1 all films were irradiated in an external magnetic field of 104 Oe, varying the projectile mass and the irradiation fluence. After a short description of the film deposition and the irradiation parameters in section 4.1.1, the effect of ion induced magnetic anisotropy will be presented in terms of MOKE measurements (section 4.1.2). A detailed analysis (EXAFS and GIXRD) of the change of the short range order and the in-plane stress in the films due to the irradiation with different projectiles will follow in section 4.1.3.

Section 4.2 will concentrate on the influence of the external parameters mechanical stress and pre-magnetization on the easy axis direction of the anisotropy. The film preparation, RBS characterization and sample treatments will be presented in section 4.2.1. It turned out that the combination of MOKE and MOMS yields decisive information about the change of the magnetic properties of the specimens. They will be illustrated in sections 4.2.2 (MOKE) and sections 4.2.3 and 4.2.4 (MOMS). Finally, the analysis of the crystallographic structure by means of XRD will be presented in section 4.2.5.

### 4.1 Fluence and mass dependence

#### 4.1.1 Deposition, ion irradiation and RBS analysis

**Deposition.** 28 films,  $10 \times 7 \text{ mm}^2$  in size, consisting of  $^{nat}\text{Fe}$  were deposited on Si(100) substrates by electron-beam evaporation. The thickness of the films was controlled in-situ by a quartz oscillator and was supposed to be 75 nm. An additional RBS analysis was performed and the resulting film thicknesses were in good agreement with the expected values (see Table 4.1).

**Ion irradiation.** After characterizing the film properties by RBS, GIXRD and MOKE, the samples were ion irradiated at room-temperature using  $^{20}\text{Ne}^+$ ,  $^{83}\text{Kr}^+$  and  $^{131}\text{Xe}^+$  ions. In order to analyze the influence of the implanted noble gas ions on the magnetic anisotropy effect, some samples were irradiated by  $^{56}\text{Fe}^+$  ions. For all implantations the projected range of the ions was kept at  $R_p \approx 33(2) \text{ nm}$ , demanding different energies for each ion species. Figure 4.1

shows the implantation profiles for 35 keV Ne<sup>+</sup>, 90 keV Fe<sup>+</sup>, 130 keV Kr<sup>+</sup> and 200 keV Xe<sup>+</sup> ions implanted into a 75 nm thick Fe film on Si(100), as simulated by *TRIM95* [Zie85].

The ions were swept over an area of  $10 \times 10 \text{ mm}^2$  (see section 3.5.1), covering the whole sample surface, and the ion current was kept between 0.8 and  $1.0 \mu\text{A}$  to avoid sample heating. During the irradiation an external magnetic field of  $H_{impl} = 104 \text{ Oe}$  was applied in the long axis direction ( $\varphi = 0^\circ$ ) of the specimens. The films were irradiated with the fluences  $\Phi = 1 \times 10^{15}$ ,  $2.5 \times 10^{15}$ ,  $5 \times 10^{15}$ ,  $7.5 \times 10^{15}$ ,  $1 \times 10^{16}$ ,  $2.5 \times 10^{16}$  and  $5 \times 10^{16} \text{ ions/cm}^2$ . The highest fluence was missing in the neon series. After the irradiation RBS, GIXRD and MOKE analyses were again performed.

**RBS analysis.** RBS was measured to gain information about film thickness, sputtering and implantation profiles. The Ne<sup>+</sup> irradiated samples were not analyzed after the ion irradiation, because the silicon and the neon signals overlap strongly.

In the RBS spectra of the 90 keV Fe<sup>+</sup>-irradiated specimens the signals of the film and the implanted ions are identical, thus the implantation profile could not be separated. Nevertheless, the interface width  $w_{Fe/Si}$  between iron and silicon was found not to change for increasing  $\Phi$ . For the highest irradiation fluence, a sputter effect ( $\approx 5 \text{ nm}$ ) was measured. In the 130 keV Kr<sup>+</sup> irradiated samples the tail of the krypton and the iron signal overlap in the RBS spectra. Thus the Kr-depth profile could be deduced in the first tens of nm of the film, while the rest of the profile was fitted according to the reduction of the iron signal in this region. A significant amount of sputtering ( $\approx 5$  and  $10 \text{ nm}$ ) was observed only for the two highest implantation fluences (see Figure 4.2). The RBS results for the samples irradiated with 200 keV Xe<sup>+</sup> were illustrated for various fluences in Fig. 3.18. Here the Fe and Xe signals are well separated and therefore an accurate analysis could be performed by means of *WiNDF*. The concentration profiles indicate a Gaussian distribution of the xenon with a tail to the substrate. The results are summarized in Table 4.1.

Figure 4.2 shows the effect of sputtering for the highest implanted fluence for each kind of ions. The sputtering yields  $Y$  are  $Y_{Fe} = 4.9(2) \text{ atoms/ion}$ ,  $Y_{Kr} = 5.9(2) \text{ atoms/ion}$  and  $Y_{Xe} = 8.4(2) \text{ atoms/ion}$ , as simulated by means of *SRIM2003*. The results obtained from the RBS analysis vary, but are significantly lower than the simulated ones. The strongest reduction in the film thickness was observed in the sample implanted with  $5 \times 10^{16} \text{ Xe}^+/\text{cm}^2$  (thickness of the sputtered layer:  $15.3 \text{ nm}$ ). The values in Table 4.1, given in the physical thickness nm, were derived with the help of the conversion  $100 \times 10^{15}/\text{cm}^2 = 11.8 \text{ nm}$  for bulk iron (see section 3.4.3).

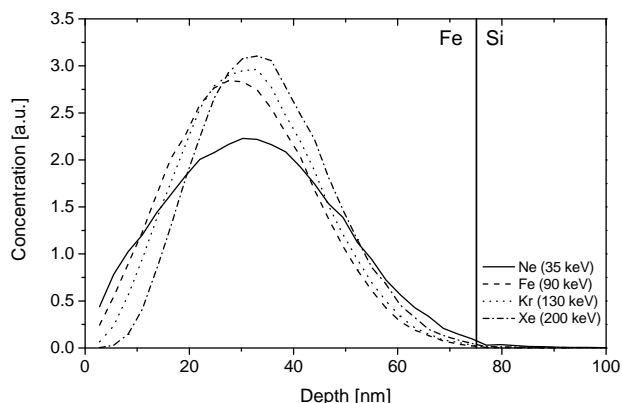


Figure 4.1: Implantation profiles of 35 keV Ne<sup>+</sup>, 90 keV Fe<sup>+</sup>, 130 keV Kr<sup>+</sup> and 200 keV Xe<sup>+</sup> ions, implanted in a 75 nm thick iron film as simulated by *TRIM95* [Zie85].

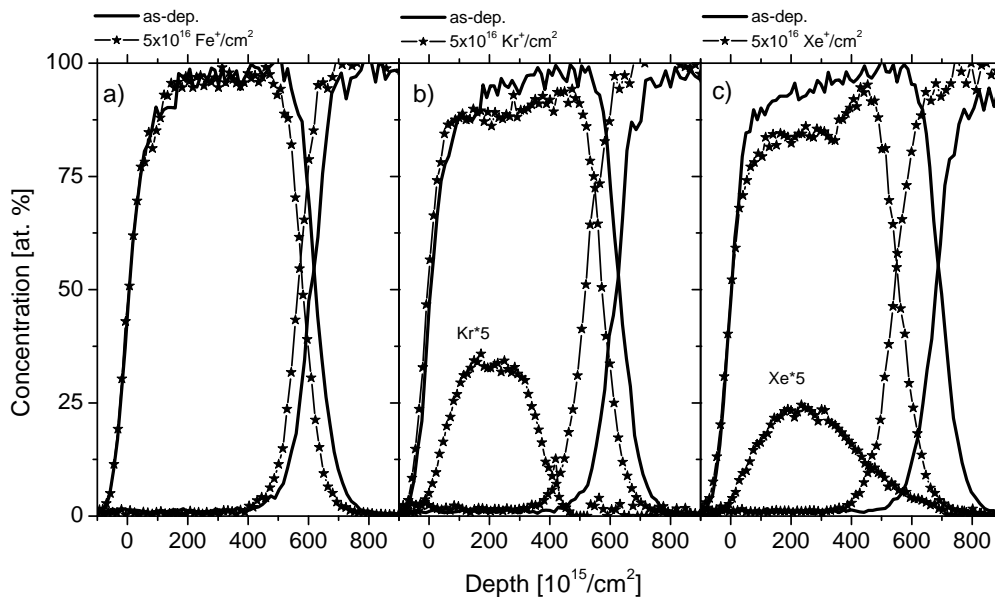


Figure 4.2: RBS concentration profiles of 75 nm thick iron films, implanted with the fluence of  $5 \times 10^{16}$  ions/cm<sup>2</sup> by a) 90 keV Fe<sup>+</sup>, b) 130 keV Kr<sup>+</sup> and c) 200 keV Xe<sup>+</sup>.

#### 4.1.2 Magnetic anisotropy (MOKE)

In this section, the changes in the magnetic properties of the films are presented, as analyzed by MOKE. All specimens were measured with an angular step size of  $\Delta\varphi = 10^\circ$ , the isotropic samples (as-deposited) with  $\Delta\varphi = 20^\circ$ . From the hysteresis loops the coercive fields  $H_c$ , the relative remanences  $M_r/M_s$  and the magnetization energies, normalized to saturation magnetization,  $E_m/M_s$  values were derived (see section 3.1.2). Because the hysteresis curve is square-shaped in the easy axis,  $M_r/M_s$  and  $H_c$  both have their maxima in this direction. The hard axis usually is in the direction of the minimum of both parameters.

The basic effect of magnetic anisotropy in an electron-beam deposited ferromagnetic film, induced by ion irradiation during the presence of an external magnetic field, is illustrated in Figure 4.3. The polar diagrams for  $H_c$  and  $M_r/M_s$  showed in addition to an isotropic part a  $\sin^2\varphi$  dependence (see section 2.1.2), which became stronger with increasing fluence of the implanted 200 keV xenon ions. In addition to this uniaxial magnetic anisotropy, another axis with high  $M_r/M_s$  and  $H_c$  values and a nearly square shaped hysteresis loop was observed perpendicular to the easy axis. Triangular hysteresis loops were measured at  $10^\circ - 20^\circ$  around this direction. A typical example is presented in Figure 4.4 for the film irradiated with  $5 \times 10^{16}$  Fe<sup>+</sup>/cm<sup>2</sup> and a detailed discussion of this observation will follow in chapter 5. Up to this discussion in section 5.1 the magnetic anisotropy will be considered as uniaxial with a high remanence hysteresis in the hard axis direction.

$t_{asdep}$ [nm]	$E$ [keV]	$\Phi_{impl}$ [ $10^{15}/\text{cm}^2$ ]	$\Phi_{RBS}$ [ $10^{15}/\text{cm}^2$ ]	$t_{irr}$ [nm]	$R_p^a$ [nm]	$R_p^b$ [nm]	$w_{Fe/Si,asdep}$ [nm]	$w_{Fe/Si,irr}$ [nm]
69(3)	90 Fe <sup>+</sup>	1	—	71(3)	—	—	14(1)	14(1)
71(3)	90 Fe <sup>+</sup>	2.5	—	69(3)	—	—	15(1)	13(1)
71(3)	90 Fe <sup>+</sup>	5	—	70(3)	—	—	12(1)	12(1)
72(3)	90 Fe <sup>+</sup>	7.5	—	69(3)	—	—	13(1)	12(1)
71(3)	90 Fe <sup>+</sup>	10	—	70(3)	—	—	14(1)	14(1)
71(3)	90 Fe <sup>+</sup>	25	—	67(3)	—	—	12(1)	12(1)
74(3)	90 Fe <sup>+</sup>	50	—	69(3)	—	—	12(1)	12(1)
75(3)	130 Kr <sup>+</sup>	1	0.9	76(3)	31.8	31(5)	14(1)	13(1)
75(3)	130 Kr <sup>+</sup>	2.5	2.0	76(3)		31(5)	14(1)	13(1)
75(3)	130 Kr <sup>+</sup>	5	4.4	71(3)		30(5)	14(1)	13(1)
74(3)	130 Kr <sup>+</sup>	7.5	5.5	73(3)		29(5)	13(1)	13(1)
75(3)	130 Kr <sup>+</sup>	10	7.2	73(3)		29(5)	12(1)	15(1)
75(3)	130 Kr <sup>+</sup>	25	16.0	69(3)		25(5)	14(1)	14(1)
75(3)	130 Kr <sup>+</sup>	50	22.2	65(3)		25(5)	12(1)	14(1)
79(3)	200 Xe <sup>+</sup>	1	1.7	74(3)	34.2	33(4)	14(1)	13(1)
77(3)	200 Xe <sup>+</sup>	2.5	2.4	78(3)		32(4)	13(1)	13(1)
81(3)	200 Xe <sup>+</sup>	5	4.4	81(3)		29(4)	14(1)	12(1)
81(3)	200 Xe <sup>+</sup>	7.5	6.8	77(3)		28(4)	14(1)	12(1)
76(3)	200 Xe <sup>+</sup>	10	8.0	75(3)		28(4)	12(1)	12(1)
79(3)	200 Xe <sup>+</sup>	25	17.8	71(3)		28(4)	14(1)	14(1)
82(3)	200 Xe <sup>+</sup>	50	19.3	67(3)		28(4)	12(1)	17(1)

Table 4.1: Results of the RBS analysis of all irradiated films.  $t$  is the film thickness,  $E$  is the implantation energy,  $\Phi$  the fluence as implanted or as measured by integration of the RBS concentration profile,  $R_p$  is the projected ion range and  $w_{Fe/Si}$  the width of the iron/silicon interface.

<sup>a</sup>as simulated by *SRIM2003*

<sup>b</sup>as measured by RBS

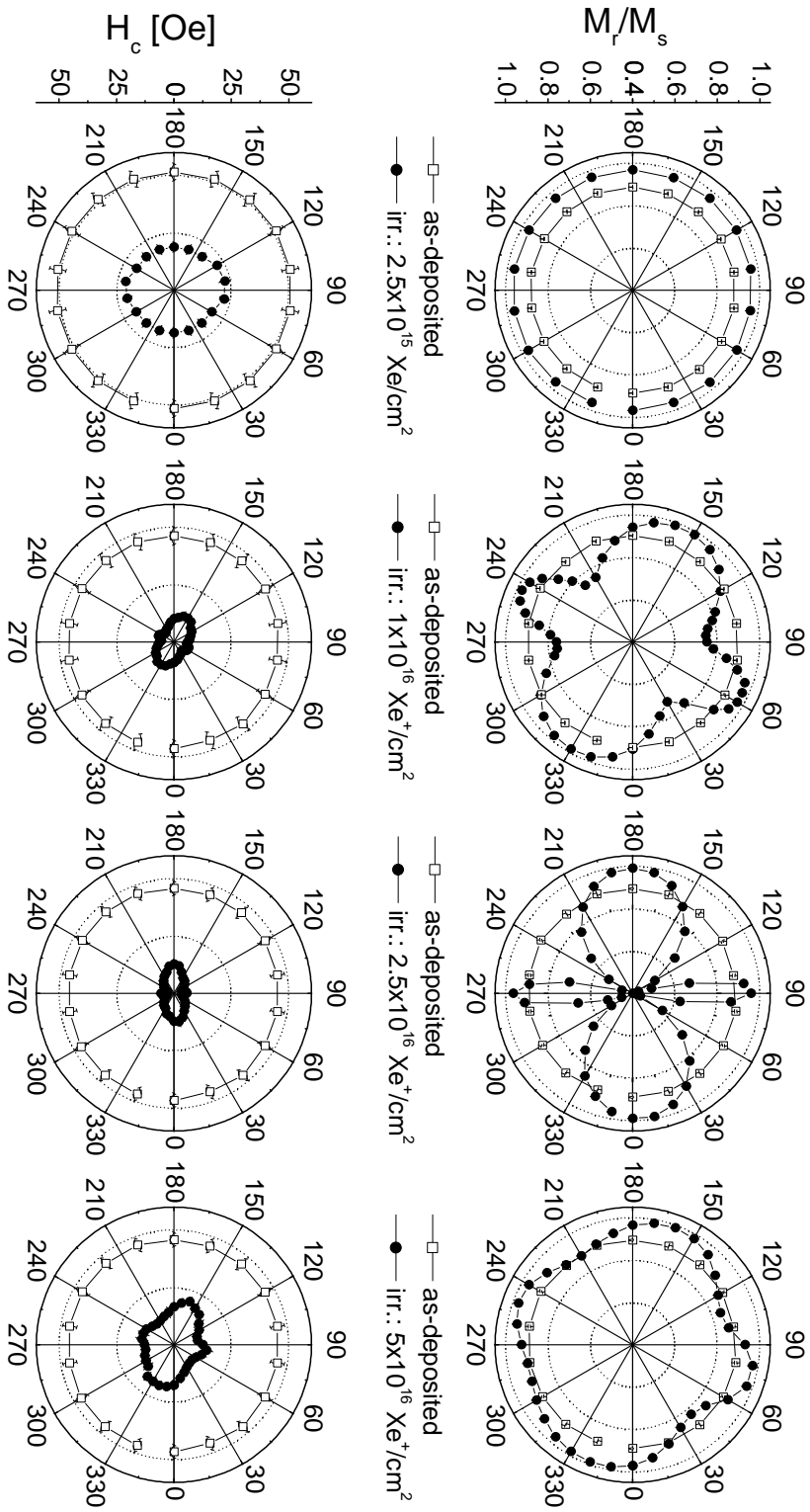


Figure 4.3: Variation of  $H_c$  and  $M_r/M_s$  for iron films irradiated with 200 keV  $\text{Xe}^+$  ions in an external magnetic field of  $H_{\text{imp}} = 104$  Oe. The maximum anisotropy for this projectile is reached at a fluence of  $2.5 \times 10^{16} \text{Xe}^+/\text{cm}^2$ .



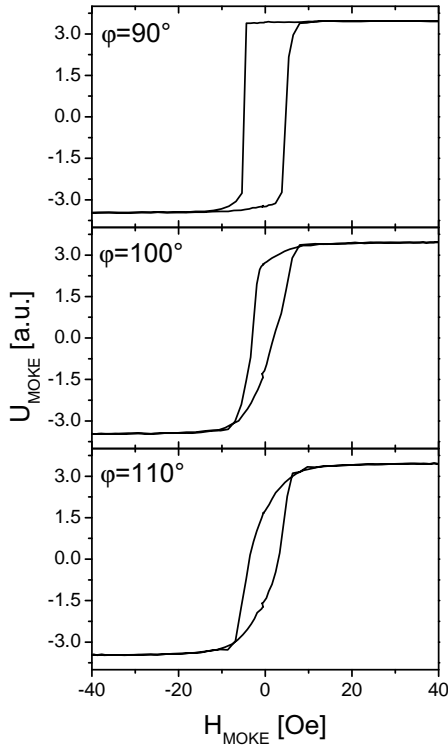


Figure 4.4: Hysteresis loops of a 75 nm thick Fe film, irradiated with  $5 \times 10^{16}$   $\text{Fe}^+/\text{cm}^2$  in various in-plane directions  $\varphi$  (see also Fig. 4.5).

The figure illustrates two fits of the normalized magnetization energy  $E_m/M_s$ , corresponding to fluences of  $7.5 \times 10^{15}$  (a) and  $2.5 \times 10^{16}$   $\text{Xe}^+/\text{cm}^2$  (b). In the fitted regions the agreement with the experiment is good, while the angles around the hard axis exhibit components of fourfold symmetry. In this context it was difficult to select the relevant region for the fitting, especially for the samples showing a small anisotropy.

The coercivities of the as-deposited samples were different for each sample. Because the isotropic fractions of the magnetization energies are closely related to  $H_c$ , only the double ratio

$$\kappa \equiv (K_0/M_s)_{irr}/(K_0/M_s)_{asdep}$$

will be considered in the further discussion, taking into account only the relative change of  $(K_0/M_s)$  due to the irradiation. The fit results of the anisotropy constants are presented in Fig. 4.7 and in Table 4.2.

Generally, the comparison of the normalized anisotropy constants resulting from MOKE measurements is not straightforward, since the MOKE-signal is only proportional to the magnetization of the specimen, and the proportionality factor depends for instance on the laser-sample geometry or the reflectivity of the surface. Thus, the measured signals of two films may differ although their magnetization vectors are identical.

The presented polar diagrams for the  $\text{Xe}^+$  irradiated specimens and the hysteresis loops are typical of the implantations of all projectiles. The samples irradiated with  $\text{Ne}^+$ ,  $\text{Fe}^+$  and  $\text{Kr}^+$  projectiles show similar shapes of their polar diagrams, but the ion fluence necessary to induce an anisotropy is larger than in the xenon irradiated samples. Figure 4.5 illustrates this dependence, summarizing the polar plots of the samples with the highest anisotropy for each ion species. For the xenon irradiated samples a decrease in the anisotropy for large fluences is observed. The other projectiles reach the largest magnetic texture at the highest  $\Phi$ .

The strength of the twofold anisotropy was obtained for all samples by fitting the equation [Bro97]

$$\frac{E_m}{M_s}(\varphi) = \frac{K_0}{M_s} + \frac{K_u}{M_s} \sin^2(\varphi - \varphi_0) \quad (4.1)$$

to the normalized magnetization energies  $E_m/M_s$ . The fitting parameters are the angle  $\varphi_0$  of the easy axis of the uniaxial anisotropy relative to the long axis of the film, the normalized uniaxial anisotropy constant  $K_u/M_s$ , and the isotropic part of the normalized magnetization energy  $K_0/M_s$ . No fourfold anisotropy term was considered, as will be discussed in section 5.1, and the angles around the hard axis with a high  $M_r/M_s$  ratio and a low magnetization energy were excluded from the fit, as indicated by the hatched  $\varphi$ -regions in Fig. 4.6.

The figure illustrates two fits of the normalized magnetization energy  $E_m/M_s$ , corresponding to fluences of  $7.5 \times 10^{15}$  (a) and  $2.5 \times 10^{16}$   $\text{Xe}^+/\text{cm}^2$  (b). In the fitted regions the agreement with the experiment is good, while the angles around the hard axis exhibit components of fourfold symmetry. In this context it was difficult to select the relevant region for the fitting, especially for the samples showing a small anisotropy.

The coercivities of the as-deposited samples were different for each sample. Because the isotropic fractions of the magnetization energies are closely related to  $H_c$ , only the double ratio

$$\kappa \equiv (K_0/M_s)_{irr}/(K_0/M_s)_{asdep}$$

will be considered in the further discussion, taking into account only the relative change of  $(K_0/M_s)$  due to the irradiation. The fit results of the anisotropy constants are presented in Fig. 4.7 and in Table 4.2.

Generally, the comparison of the normalized anisotropy constants resulting from MOKE measurements is not straightforward, since the MOKE-signal is only proportional to the magnetization of the specimen, and the proportionality factor depends for instance on the laser-sample geometry or the reflectivity of the surface. Thus, the measured signals of two films may differ although their magnetization vectors are identical.

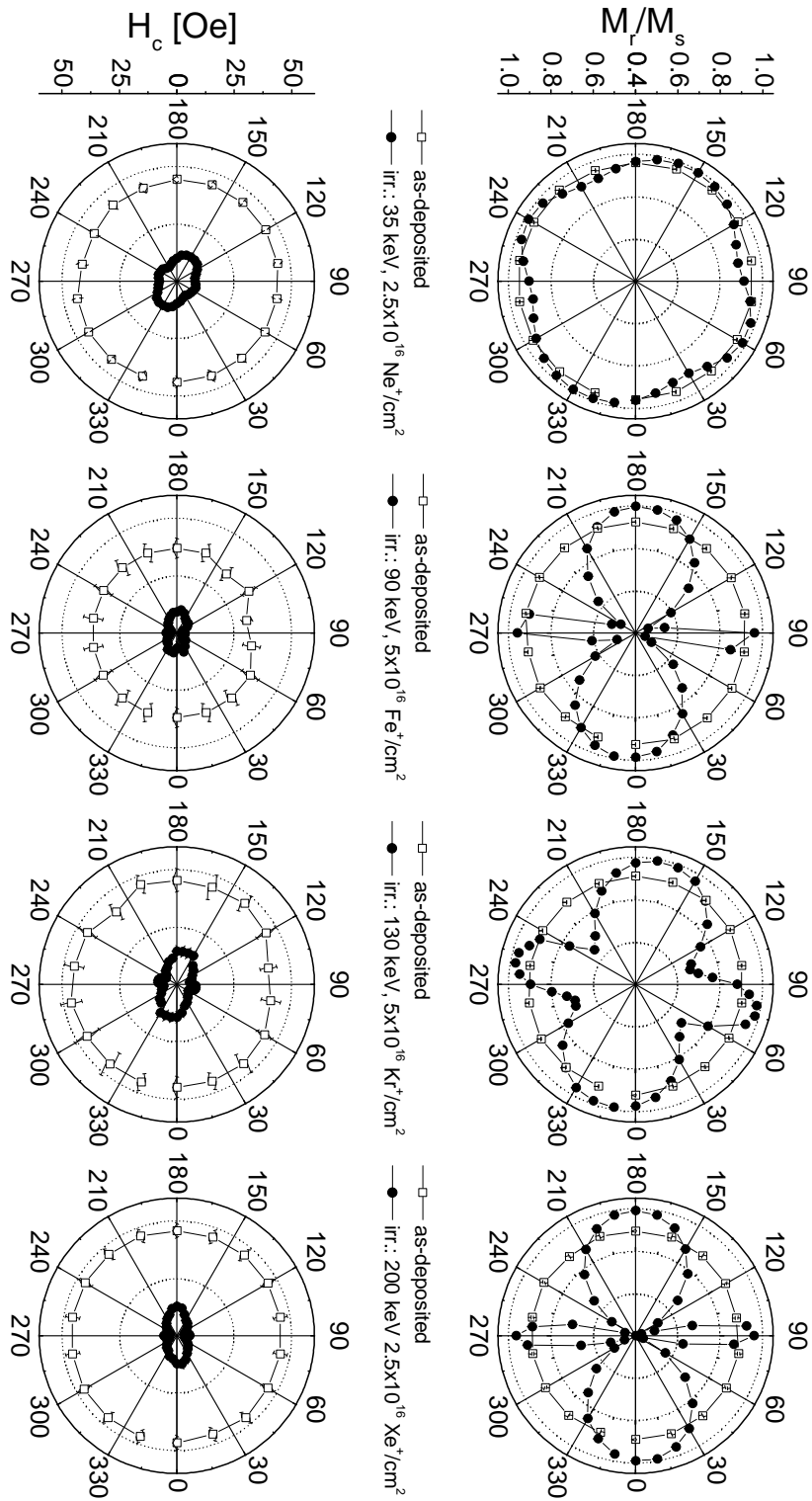


Figure 4.5: Variation of  $H_c$  and  $M_r/M_s$  for the maximum measured anisotropy for all projectiles.

When comparing the MOKE-signals of the present specimens in saturation state, they are found to match within an error of 2%. Only four exceptions were observed: the specimens irradiated with  $5 \times 10^{16} \text{ Fe}^+/\text{cm}^2$  (88% of the average saturation-signal),  $5 \times 10^{16} \text{ Kr}^+/\text{cm}^2$  (86%),  $2.5 \times 10^{16} \text{ Xe}^+/\text{cm}^2$  (89%) and  $5 \times 10^{16} \text{ Xe}^+/\text{cm}^2$  (86%). Because most of the specimens show the same saturation signal, they are supposed to have similar  $M_s$ , and for the four exceptions the difference is taken into account by a larger error. Thus the normalized anisotropy constants illustrated in Figure 4.7 are comparable within the given errors.

The fluence and ion mass dependence of the normalized anisotropy constants in Fig. 4.7 is very instructive. Several effects can be observed for  $\kappa(\varphi)$ :

1. Generally,  $\kappa$  decreases logarithmically for increasing ion fluence.
2.  $\kappa$  drops to a value of 0.15. Increasing the ion fluence further does not affect this parameter up to  $2.5 \times 10^{16} \text{ ions}/\text{cm}^2$ . Only the xenon irradiation with  $5 \times 10^{16}/\text{cm}^2$  slightly increases the value of  $\kappa$ .
3. The decrease of  $\kappa$  is different for the different projectiles. While in the case of xenon saturation is reached for  $2.5 \times 10^{15} \text{ Xe}^+/\text{cm}^2$ , one needs  $7.5 \times 10^{15} \text{ Kr}^+/\text{cm}^2$  and more than  $2.5 \times 10^{16} \text{ Ne}^+/\text{cm}^2$  to reach  $\kappa = 0.15$ .
4. Although iron has a smaller mass compared with xenon and krypton, and its implantation energy was smaller, the decrease in  $\kappa$  is even faster for  $\text{Fe}^+$  irradiation (the slope of the line is larger).
5. For low iron fluences  $\kappa$  increases to  $\kappa > 1$ . As it is correlated with  $H_c$  of the specimens, this

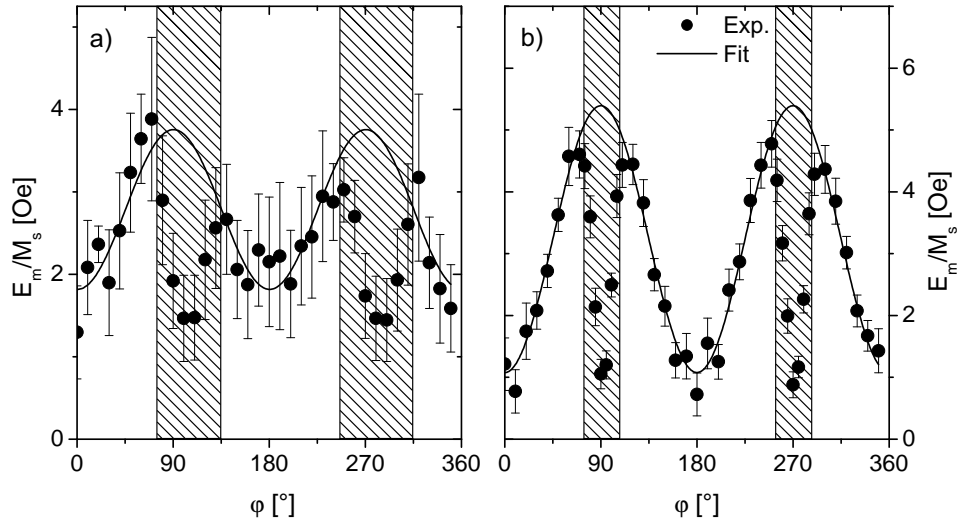


Figure 4.6: Fit of the normalized magnetization energies for the samples irradiated with  $7.5 \times 10^{15}$  (a) and  $2.5 \times 10^{16} \text{ Xe}^+/\text{cm}^2$  (b). The points measured around the hard axis direction (hatched area) were not used for the fit.

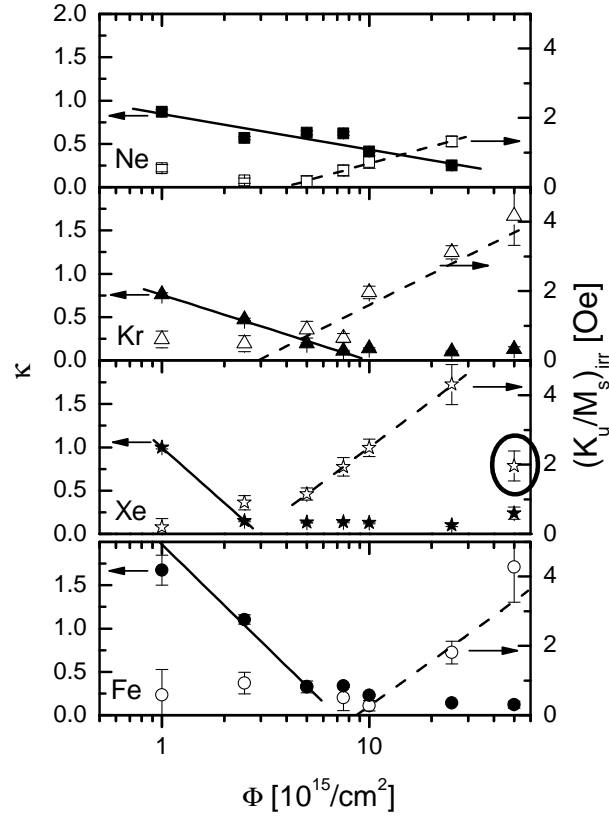


Figure 4.7: Normalized anisotropy constants  $\kappa$  (solid symbols) and  $(K_u/M_s)_{irr}$  (open symbols) resulting from the normalized magnetization energy.

is equivalent to a rise in the coercivity.

The dependence of the parameter  $(K_u/M_s)_{irr}$  on the implanted fluence and ion mass can be summarized as follows:

1.  $(K_u/M_s)_{irr}$  is very small for small ion fluences.
2.  $(K_u/M_s)_{irr}$  increases logarithmically for larger fluences of the projectiles iron, krypton and xenon. For the neon irradiation only a slight rise can be seen.
3. The highest fluence of xenon induces a decrease in the anisotropy constant as highlighted by the circle in Fig. 4.7.
4. The increase in  $(K_u/M_s)_{irr}$  for the self-irradiation starts at  $1 \times 10^{16} \text{ Fe}^+/\text{cm}^2$  and not at  $5 \times 10^{15} \text{ ions}/\text{cm}^2$  like in the case of the other projectiles.

Concerning the symmetry angle  $\varphi_0$ , we found good alignment with the direction of the external magnetic field for high fluences and heavy projectiles, but not for the light ions. However, for the highest  $\text{Xe}^+$  and  $\text{Kr}^+$  fluences a strong deviation of  $\varphi_0 = 0^\circ$  was found. All results of the anisotropy fits are summarized in Table 4.2.

$\Phi$ [ $10^{15}/\text{cm}^2$ ]	35 keV Ne <sup>+</sup>			90 keV Fe <sup>+</sup>		
	$\kappa$	$(K_u/M_s)_{irr}$	$\varphi_0$ [°]	$\kappa$	$(K_u/M_s)_{irr}$	$\varphi_0$ [°]
1	0.87(3)	0.55(11)	-19(8)	1.67(17)	0.59(74)	30(8)
2.5	0.57(2)	0.19(8)	43(14)	1.10(5)	0.92(32)	28(12)
5	0.63(2)	0.16(17)	20(31)	0.33(2)	0.81(18)	-67(8)
7.5	0.62(2)	0.48(16)	5(11)	0.34(2)	0.50(37)	-3(13)
10	0.41(2)	0.73(18)	-29(6)	0.23(1)	0.28(15)	-86(18)
25	0.25(1)	1.32(15)	-32(4)	0.14(1)	1.81(33)	-5(5)
50	—	—	—	0.12(4)	4.27(101)	-10(4)

	130 keV Kr <sup>+</sup>			200 keV Xe <sup>+</sup>		
	$\kappa$	$(K_u/M_s)_{irr}$	$\varphi_0$ [°]	$\kappa$	$(K_u/M_s)_{irr}$	$\varphi_0$ [°]
1	0.76(2)	0.60(24)	-46(14)	1.00(2)	0.19(25)	43(39)
2.5	0.47(1)	0.48(23)	59(16)	0.15(1)	0.90(21)	7(9)
5	0.19(1)	0.88(24)	0(8)	0.13(1)	1.15(18)	47(5)
7.5	0.11(1)	0.64(13)	15(8)	0.14(1)	1.94(27)	0(5)
10	0.14(2)	1.96(19)	6(4)	0.13(1)	2.48(25)	-35(4)
25	0.10(1)	3.11(19)	-6(4)	0.10(2)	4.31(58)	0(3)
50	0.13(3)	4.16(84)	-18(3)	0.24(7)	1.97(43)	-30(5)

Table 4.2:  $\kappa$ ,  $(K_u/M_s)_{irr}$  and  $\varphi_0$  for all fluences and projectiles after ion implantation.

### 4.1.3 Microstructure

#### Short range order (EXAFS)

The short range order of the samples was studied by means of EXAFS (see section 3.4.2) after irradiations with Xe<sup>+</sup>, Kr<sup>+</sup> and Fe<sup>+</sup> at fluences of  $1 \times 10^{16}$  and  $5 \times 10^{16}$  ions/cm<sup>2</sup>. One absorption spectrum  $\mu(E)$  and a  $\chi \cdot k^2(k)$  spectrum of this experiment were already depicted in Fig. 3.16. The Fourier transforms, extracted from the product  $\chi \cdot k^2(k)$  for all measured implantation fluences, are shown in Fig. 4.8.

Even without fitting these curves some qualitative statements can be made. The most obvious finding is the uniform decrease in signal height for rising ion fluence and all projectile species. A decrease in the amplitude is usually correlated with a decrease in the coordination number of the iron atoms, or with an increase in the disorder of the crystal given by a higher Debye-Waller-factor. At first glance, the change in the amplitude neither depends on the projectile species used nor on its energy. Another important result is that the overall shape of the spectra does not change. No peak correlated to a different phase occurs.

For the analysis of the data only the first two shells of iron were used. In the Fourier transform both shells overlap and result in the large peak at about 2.2 Å (see Fig. 4.8). Note that the position of the shell contribution is related to the radius of the shells, but is not equal to  $r$ . The peaks were fitted simultaneously with the program *VIPER*, using the amplitude and phase-file created by means of *FEFFIT 2.55*.

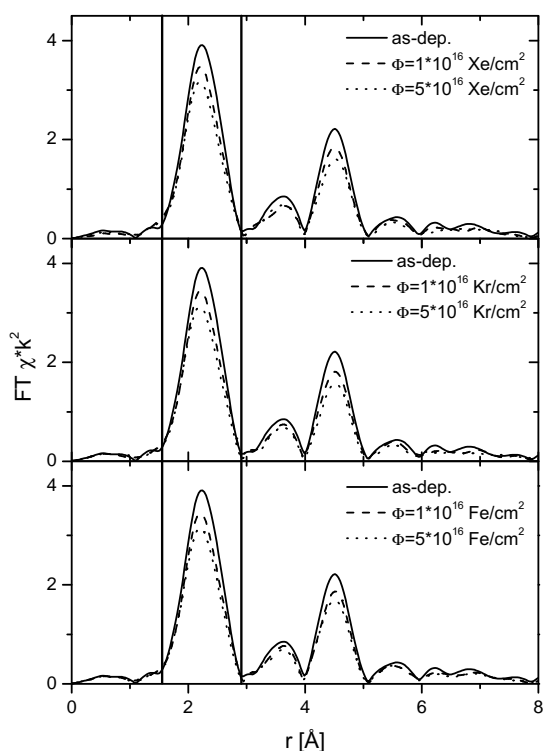


Figure 4.8: Fourier transforms of the EXAFS measurements. A general decrease in the oscillation amplitude with increasing fluence can be observed.  $r$  of first and second shell is indicated by the lines.

The resulting parameters were the coordination numbers of the first two shells  $N_1$  and  $N_2$ , and the radius of the second shell,  $R_2$  ( $R_1 = \frac{\sqrt{3}}{2}R_2 = \frac{\sqrt{3}}{2}a$ ). The Debye-Waller-factor  $\sigma$  remained constant during the fitting. Despite the strong correlation between  $\sigma$  and the coordination numbers, the results concerning  $N_i$  are reasonable. As the radii of the shells differ by only 14%, Figure 4.9 a) illustrates  $N_1 + N_2(\Phi)$  ( $\Phi$  was the same for all projectiles, the points are only separated to distinguish the error bars). The errors of the measurement are quite large. However, no significant difference in the reduction of  $N_1 + N_2$  for iron, krypton and xenon-irradiated films can be deduced: as-deposited the first two shells are nearly completely filled (96( $\frac{4}{6}$ )%), after  $1 \times 10^{16}$  ions/cm<sup>2</sup> had been implanted only 83(6)% of the sites are occupied and this fraction further decreases to 75(6)% for implantations with  $\Phi = 5 \times 10^{16}$  ions/cm<sup>2</sup>.

Regarding the change of the lattice constant  $a$  (see Fig. 4.9 b)) two results are obvious: firstly,  $a$  is equal within the error for the different projectiles and secondly, it is also equal within the error for the different fluences  $\Phi$ . There might be an increase in the lattice constant for the highest Fe<sup>+</sup> and Kr<sup>+</sup> fluence and a slight decrease for Xe<sup>+</sup>, but within the 0.004 Å error these effects are not significant.

### Crystallographic structure (GIXRD)

Stress in thin films plays an important role concerning their magnetic parameters such as the coercive field. Inhomogeneously stressed films can also show magnetic anisotropy [San99, Zha01]. It is well-known that after deposition the internal tensile stress in a film can be of the order of 1 GPa or larger [Tho89], depending on the deposition method and conditions, and on the materials used. To control the film stress in the present experiments, it was analyzed by means of GIXRD. The spectra were measured for all the films with  $\alpha = 2^\circ$  and rotating specimen, and the reflection peaks in (110), (200) and (211) direction were fitted with symmetric Pearson VII line-shapes in the *Origin* program, as described in section 3.4.1 and illustrated in Fig. 3.15. The peak positions were corrected according to the grazing angle [Tak90]. With the corrected angles a stress analysis (see section 3.4.1) was performed.

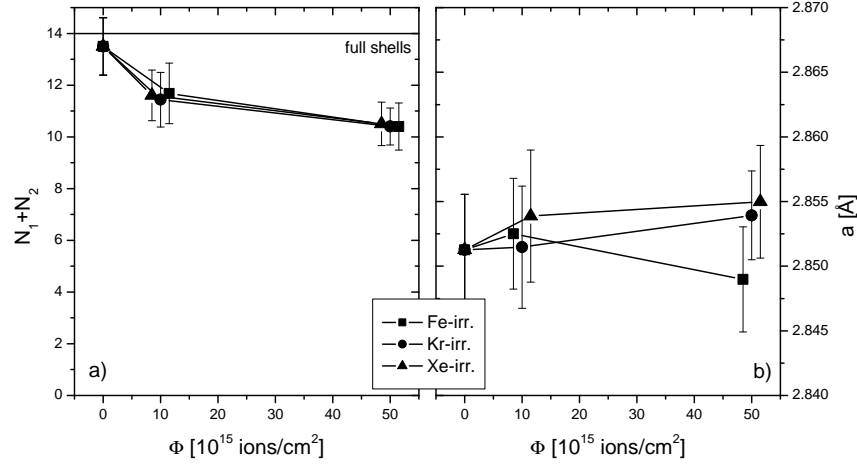


Figure 4.9: a) Variation of  $N_1 + N_2$  for the iron films irradiated with 1 or  $5 \times 10^{16}$  ions/cm<sup>2</sup>. b) lattice constant/radius of the second shell of the irradiated films. The points are separated in  $\Phi$  to distinguish the error bars.

According to equation (3.23) in section 3.4.1, the equation

$$\frac{a_\psi - a_0}{a_0} = \sigma \left[ \left( \frac{1 + \nu}{E} \right)_{(hkl)} \sin^2 \psi - \left( \frac{2\nu}{E} \right)_{(hkl)} \right] \equiv \sigma \cdot \Xi_{(hkl)} \quad (4.2)$$

is valid for homogeneously stressed thin films ( $\sigma_1 = \sigma_2 = \sigma$ ,  $a_{\varphi\psi} = a_\psi$ ).  $\sigma$  can be obtained by a simultaneous fit of  $\sigma$  and  $a_0$ , while  $\Xi_{(hkl)}$  and  $a_\psi$  are known from the experiment for the (110), (200) and (211) directions. Consequently,  $\sigma$  can be illustrated by the linear slope of a plot of the relative change of the lattice parameter  $\Delta a/a_0$  versus  $\Xi_{(hkl)}$  with the specific Miller indices  $(hkl)$  of the concerned angles  $\theta$  and  $\psi$ .

The Young moduli and the Poisson ratios are different for the three measured crystallographic directions. Knowing the compliance constants of iron films  $s_{11} = 7.64$  (TPa)<sup>-1</sup>,  $s_{12} = -2.81$  (TPa)<sup>-1</sup>,  $s_{44} = 8.71$  (TPa)<sup>-1</sup> the parameters are [Nye85, San99]:

$$\begin{aligned} E_{(110)} &= 223 \text{ GPa} & \nu_{(110)} &= 0.198 \\ E_{(200)} &= 175 \text{ GPa} & \nu_{(200)} &= 0.314 \\ E_{(211)} &= 198 \text{ GPa} & \nu_{(211)} &= 0.294 \end{aligned}$$

The resulting graphs are shown in Figure 4.10 for all implanted ions and fluences. These measurements yield the following observations: the graphs b), c) and d) indicate a successive decrease in tensile stress (positive slope) and the relaxation is correlated to the mass of the projectile, as for xenon ions the process occurs fastest. In some measurements the points do not behave linearly, especially for samples irradiated with neon ions (a). They match this tendency only if the values corresponding to the Fe(200) peak ( $\Xi_{(hkl)} = -1.7$ ) are neglected. When considering all points, like in the final analysis, the slopes seem to be smaller or more negative than the

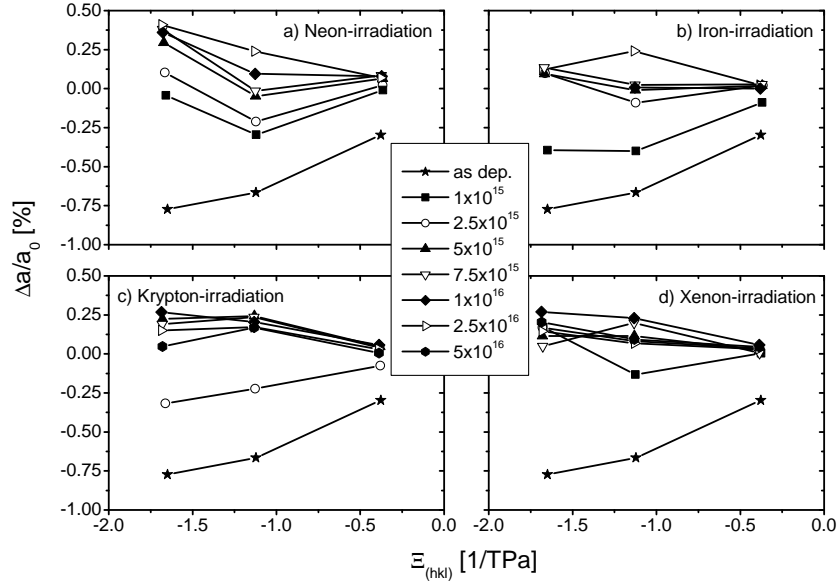


Figure 4.10: Dependence of the lattice expansion on  $\Xi_{(hkl)}$ . The slope of the plotted points is the in-plane film stress.

expected values.

Generally, it is recognized that the slope is positive for the as-deposited samples and the low ion fluences. For increasing ion fluences it changes its sign to negative slope, staying more or less constant for all higher ion fluences, particularly for the heavy elements. The results for the fit of the stress are presented in Fig. 4.11 a). Fig. 4.11 b) shows the lattice constants  $a_0$  of the hypothetical stress-free lattices, resulting from the fit, and the averages of the measured lattice constants  $a_{\psi, average}$  for which  $\psi$  is between  $20^\circ$  and  $40^\circ$ . The different values for the as-deposited lattice constants  $a_0$  and  $a_{\psi, average}$  can be explained by the strong decrease in the out-of-plane lattice constant due to the tensile stress after deposition. For the irradiated specimens the difference between the values is smaller because the stress is relaxed.

The results of the GIXRD analysis can be summarized as follows:

1. For low ion fluences, the stress of originally  $\sigma = 3.8(4)$  GPa decreases rapidly for any projectile.
2. For higher fluences, the stress saturates at a compressive stress of  $\sigma \approx -1$  GPa. This observation is true for all projectiles (dotted lines in Fig. 4.11 a)).
3. While the decrease in  $\sigma$  happens very slowly for  $\text{Ne}^+$  irradiation, the stress in the  $\text{Xe}^+$  bombarded films already saturates for  $\Phi = 1 \times 10^{15}$  ions/cm<sup>2</sup>.
4. The  $\text{Ne}^+$  irradiation induces a very large compressive stress of  $-2$  GPa, whose possible origin was already discussed.
5. The lattice constant  $a_0$  of the stress-free lattice decreases for low ion fluences of any projectile.
6. For higher fluences,  $a_0$  rises, reaching a saturation value similar to the one of the as-deposited sample. For the xenon irradiation this increase happens rapidly, for neon very slowly.



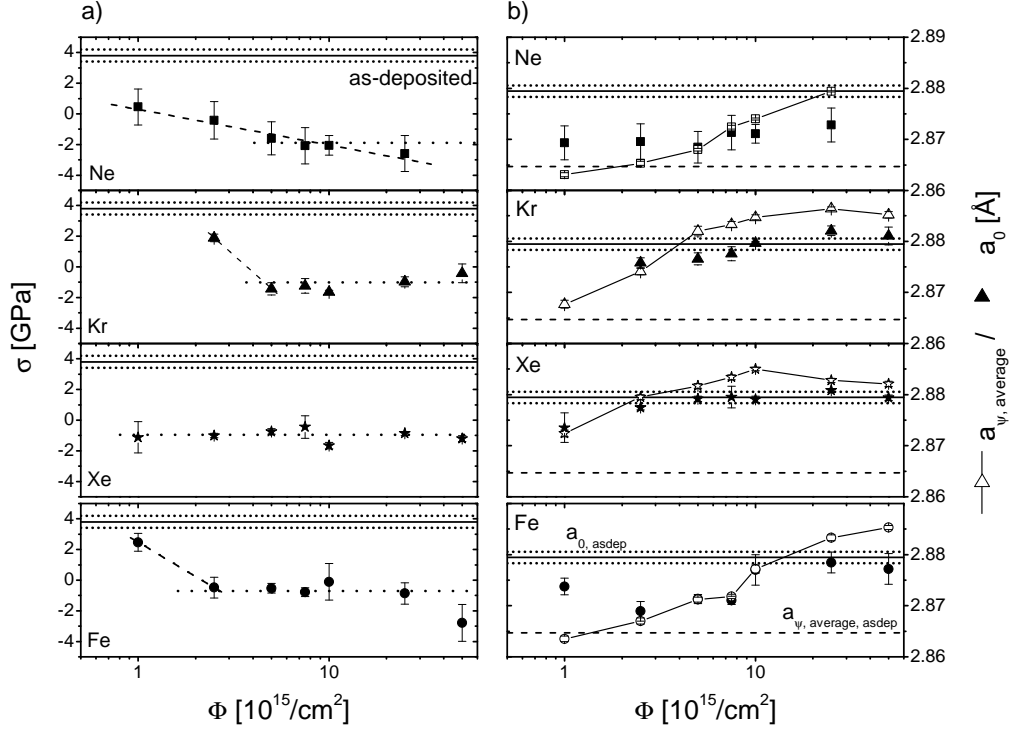


Figure 4.11: a) fluence dependence of the stress, resulting from the slopes of the graphs in Fig. 4.10. b) fluence dependence of  $a_0$  and average of the measured lattice constants  $a_{\psi, \text{average}}$ .

## 4.2 Influence of external stress and magnetization

The present section was motivated by and is closely related to the work of Zhang et al. on ion irradiated Ni films [Zha01, Zha03a]. One main subject of his work was to investigate the dependence of the magnetic uniaxial anisotropy on external mechanical tensile stress and a magnetic field applied during room-temperature ion irradiation. Zhang found that both external parameters align the easy axis of magnetization parallel to this predetermined direction. A comparison between his results and the present ones on iron films may lead to a better understanding of the influence of these parameters.

### 4.2.1 Deposition, experiments and layer structures

**Deposition.** For the following experiments 12 iron films,  $10 \times 7 \text{ mm}^2$  in size, were prepared. Their thickness was 75 nm as measured in-situ by a quartz oscillator. Six of them, consisting of  $^{nat}\text{Fe}$ , were deposited by electron-beam evaporation in the center of  $40 \times 15 \text{ mm}^2$  large thermally oxidized Si(100) wafers (see Fig. 3.19). The others were prepared in the same way on Si(100) wafers, but they contain 15 nm thin  $^{57}\text{Fe}$  layers at various depths, deposited by an effusion cell. Since natural iron consists of 91.7%  $^{56}\text{Fe}$  but only of 2.2%  $^{57}\text{Fe}$ , the marker layer ( $^{57}\text{Fe}$ , enriched

Name	L1: $^{nat}\text{Fe}$ $t$ [nm]	L2: $^{57}\text{Fe}$ $t$ [nm]	L3: $^{nat}\text{Fe}$ $t$ [nm]	$t_{RBS}$ [nm]	$d_{57\text{Fe}} /$ $w_{57\text{Fe}}$ [nm]	$d_{Xe}$ [nm]	$C_{Xe}$ [at%]
1-I	60	15	—	80(3)	75(3)/18(3)	24(3)	2.3
1-M	30	15	30	84(3)	41(3)/17(3)	22(3)	2.5
1-S	—	15	60	82(3)	9(3)/17(3)	24(3)	2.3
2-M	30	15	30	59(3)	30(3)/12(3)	28(3)	1.8
2-S	5	15	55	58(3)	5(3)/11(3)	24(3)	2.3
2-B	18	15	42	56(3)	17(3)/10(3)	—	—

Table 4.3: Layer thicknesses ( $t$ ) as measured by the in-situ quartz oscillator. Layer 1 (L1) is at the sample surface, layer 3 at the interface with the substrate. The right-hand columns show results of the RBS measurements: overall film thickness  $t_{RBS}$ , marker layer depth  $d_{57\text{Fe}}$ , width  $w_{57\text{Fe}}$  of the  $^{57}\text{Fe}$  distribution and depth  $d_{Xe}$  of highest Xe-concentration  $C_{Xe}$ .

to 95%) contains nearly 90% of all  $^{57}\text{Fe}$  atoms of the layer structure. These films will be called 1-I for the specimen with the  $^{57}\text{Fe}$  layer at the interface with the substrate, 1-M and 2-M for the specimens with the  $^{57}\text{Fe}$  layer in the middle, 1-S and 2-S for the specimens with the  $^{57}\text{Fe}$  layer at the surface or near the surface, and 2-B for the specimen having the  $^{57}\text{Fe}$  between the surface and the middle (see Table 4.3). The samples with the same number in their name were prepared on the same day and under identical conditions.

**Experiments.** The experiments which will be described in section 4.2.2 were done in a similar way as those presented in [Zha01]. The  $^{nat}\text{Fe}/\text{SiO}_2$  films were bent, irradiated with ion fluences from  $4 \times 10^{14}$  to  $4 \times 10^{16}$   $\text{Xe}^+/\text{cm}^2$ , and finally relaxed. The curvature was fixed to  $1/R \approx 1/\text{m}$ , sufficient to induce the anisotropy in the case of nickel films, and the irradiation was carried out at room-temperature without an external magnetic field. MOKE hysteresis loops were measured in four different states of the sample (1. as-deposited, 2. bent, 3. irradiated and still bent, 4. irradiated and relaxed) and for several orientations  $\varphi$  of the long axis of the films with respect to the measurement field  $H_{MOKE}$ . Additionally, the specimens were characterized in their as-deposited and relaxed state by means of RBS and XRD in  $\theta - 2\theta$  geometry. In this way, detailed information about the dependence of the magnetic texture on the irradiated fluence, and about the influence of the bending and the relaxation process was obtained. Like in Zhang's experiments [Zha01], only MOKE was used for the analysis of the magnetic anisotropy in these films.

Additional information about the sample magnetism was gained with MOMS, which measures the easy axis of magnetization without externally magnetizing the film. In sections 4.2.3 and 4.2.4, the influence of stress and the magnetization state during the room-temperature irradiation of the Fe films containing an  $^{57}\text{Fe}$  marker layer is investigated. The ion fluence was  $1 \times 10^{16}$   $\text{Xe}^+/\text{cm}^2$ , which was found to have a large effect on the magnetic anisotropy (see section 4.1). Sample preparation and bending was the same as described above for section 4.2.2. The following experiments allowed to investigate the influence of stress and pre-magnetization during irradiation on the orientation of the easy axis after relaxation of the film.

Samples 1-I, 1-M and 1-S were all measured by means of MOMS, MOKE and XRD before irradiation and then irradiated in bent condition. After relaxation they were again characterized

Name	MOMS	MOKE	XRD	RBS	magnet.	bend.	MOMS	
1-I	•	•	•	•	—	•	—	
1-M	•	•	•	•	—	•	—	
1-S	•	•	•	•	—	•	—	
2-M	•	—	•	•	—	•	•	
2-S	•	•	•	•	•	—	•	
2-B	•	•	•	•	•	•	•	

Name	irr.	MOMS	relaxing	MOMS	MOKE	RBS	XRD	SIMS
1-I	•	—	•	•	•	•	•	•
1-M	•	—	•	•	•	•	•	•
1-S	•	—	•	•	•	•	•	•
2-M	•	•	•	•	•	•	•	—
2-S	•	•	—	—	•	•	•	—
2-B	•	•	•	•	—	—	•	—

Table 4.4: Summary of all the samples and all possible combinations of treatments and analyses. The symbols • indicate that the treatment/analysis was performed.

by MOMS, MOKE and XRD. Thus, the influence of the stress irradiation was investigated at different sample depths.

Sample 2-M was irradiated in bent condition without being magnetized before, which means that for the magnetic characterization of the as-deposited sample only MOMS was applied. Thus, only the influence of the external stress on the orientation of the anisotropy was regarded. Samples 2-S and 2-B were magnetized in one particular direction and then irradiated in flat (2-S) or in bent condition (2-B). In these experiments the effect of sample magnetization and stress can be observed.

The characterization of 2-M, 2-S and 2-B included MOMS, MOKE, RBS and XRD. Since any magnetic field could disturb the original magnetic status of the film (see section 3.3), it was very important to use MOMS first after deposition. Later on, MOKE was applied to 2-S and 2-B, and the structural characterization including RBS and XRD followed. After the characterization of the as-deposited state, samples 2-M and 2-B were bent to a curvature of 1/m and then irradiated by  $1 \times 10^{16}$  Xe<sup>+</sup>/cm<sup>2</sup> at room-temperature without applying an external magnetic field. Finally, the samples were relaxed, and again characterized by means of MOMS, MOKE, RBS and XRD. Detailed information about the order of the specimen treatments are summarized in Table 4.4.

**Layer structure.** Depending on the position of the <sup>57</sup>Fe in the films, the investigated depth range of MOMS varies and, in contrast to MOKE, possibly depth-sensitive information about the anisotropy behavior can be gained. To allow for a serious discussion of the MOMS results, the layer structures and in particular the positions and widths of the <sup>57</sup>Fe distributions in the films were checked by means of RBS. The overall layer thicknesses are slightly larger than 75 nm for the "1"-samples and smaller for the "2"-samples (see Table 4.3), possibly due to an inaccurate calibration of the quartz oscillator. The difficulty of measuring the deposited <sup>57</sup>Fe thickness using a flux meter, as done for the effusion-cell deposition, can be seen by the variation of the

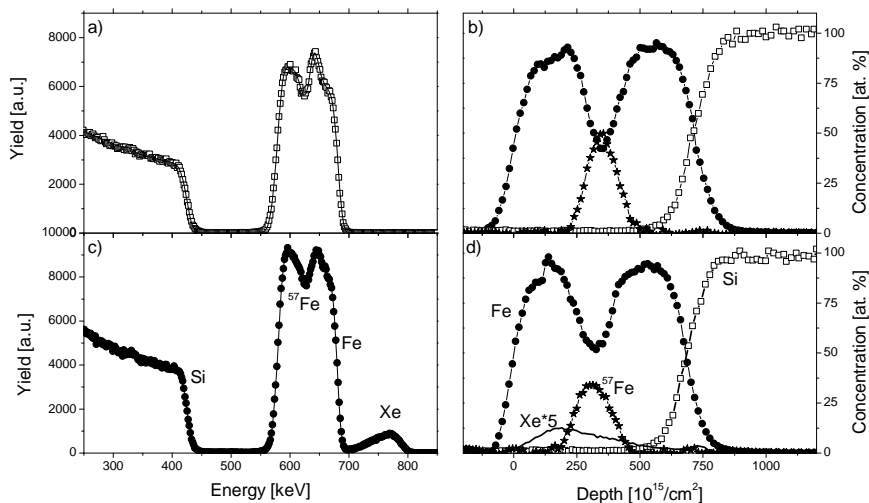


Figure 4.12: RBS spectra and depth profiles of sample 1-M. a) and b) refer to the as-deposited sample, c) and d) to the one irradiated with 200 keV,  $1 \times 10^{16}$  Xe<sup>+</sup>/cm<sup>2</sup> at room-temperature and a curvature of  $1/R \approx 1/m$ .

marker layer width (see Table 4.3). However, this error is not decisive for the deviation of the overall layer thickness.

Figs. 4.12 a) and c) illustrate RBS spectra of sample 1-M, irradiated with  $1 \times 10^{16}$  Xe<sup>+</sup>/cm<sup>2</sup>. The position of the <sup>57</sup>Fe can be recognized as the superposed structure in the <sup>nat</sup>Fe signal. Comparing the as-deposited and the irradiated sample, after irradiation the marker layer stays

at the same place and shows only minor broadening of the concentration profile (Figs. 4.12 b) and d)). A similar result, but with a sharper interface and a higher <sup>57</sup>Fe concentration in the marker layer, was observed on 1-M by secondary ion mass spectroscopy (SIMS) at the Institut für Materialphysik, Universität Göttingen. SIMS is directly sensitive to the measured isotope and thus, especially for the separation of <sup>nat</sup>Fe and <sup>57</sup>Fe or the detection of light elements, more reliable than RBS (see Fig. 4.13). In conclusion, the depth of the marker layer, accessible for MOMS, is the same before and after irradiation.

In addition to the <sup>57</sup>Fe/<sup>nat</sup>Fe layer structure, also the amount of iron oxides was

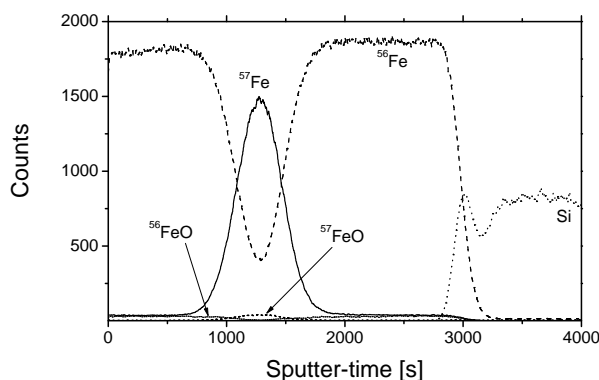


Figure 4.13: SIMS-measurement of sample 1-M. The Si substrate, <sup>56</sup>Fe, <sup>57</sup>Fe and iron oxides were analyzed.

measured by SIMS. A certain amount of oxide formation is expected, because the films were not capped by a protecting layer of a non-reactive material. As illustrated in Figure 4.13, the amount of oxidized iron is less than 2.5% of the total iron yield and has a constant concentration over the whole film depth, indicating no high degree of oxidation at the sample surface.

The projected range of the xenon ions in the film was  $R_p = 34$  nm, as simulated by means of *SRIM2003* [Zie99, SRI03], to make sure that no interface mixing occurs. The interface width  $w_{Fe/Si}$  is not changed by irradiation and the maximum concentration of  $\approx 2.5$  at.% for  $\Phi = 1 \times 10^{16}$  Xe<sup>+</sup>/cm<sup>2</sup> is found by means of RBS at 22 - 28 nm depth. This does not agree with the simulation, even when the sputtering of 4 nm is considered. As the xenon depth profile has no symmetric shape it seems to be useful to integrate the area of the profile and to calculate the position of the half integral. This value lies at about 31(3) nm, which perfectly matches the calculated  $R_p$ -value.

### 4.2.2 Influence of stress (MOKE)

In this section the results of the experiments on the <sup>nat</sup>Fe/SiO<sub>2</sub> films will be illustrated. Figure 4.14 shows the polar diagrams of the parameters  $H_c$  and  $M_r/M_s$  as obtained by MOKE with an in-plane step width of  $\Delta\varphi = 10^\circ$ . The films were irradiated with various Xe<sup>+</sup> fluences  $\Phi$  at room-temperature and they were bent with a curvature of  $1/R \approx 1/m$  during the irradiation. Mainly three effects were observed:

1. The coercivity of the film changed continuously from  $H_c = 53(2)$  Oe (as-deposited) to 9(1) Oe ( $\Phi = 4 \times 10^{15}$  Xe<sup>+</sup>/cm<sup>2</sup>) or 14(1) Oe ( $\Phi = 1 \times 10^{16}$  Xe<sup>+</sup>/cm<sup>2</sup>) in the easy axis direction of the samples. For larger fluence,  $H_c$  increased, reaching nearly its initial value for  $4 \times 10^{16}$  Xe<sup>+</sup>/cm<sup>2</sup>.
2. The relative remanence  $M_r/M_s$  was isotropic in the as-deposited specimens and for small fluences. For  $\Phi = 4 \times 10^{15}$  and  $1 \times 10^{16}$  Xe<sup>+</sup>/cm<sup>2</sup>, the remanence became anisotropic. By further increasing the fluence, a nearly isotropic remanent magnetization was measured, similar to the one in the as-deposited sample.
3. The shape of the hysteresis curves around the hard axis changed as described in section 4.1.2: in the easy axis and the hard axis direction it was square-shaped with a high coercivity and at angles between 10 and 15° around the hard axis, the loop is asymmetric with a triangular shape (one branch showed an easy axis and the other branch a hard axis behavior, see Fig. 4.4).

Taking into account only the uniaxial anisotropic part of the polar plots of  $M_r/M_s$ , the directions  $\varphi_0$  of the easy axes of the induced anisotropy in the samples irradiated with  $\Phi = 4 \times 10^{15}$  and  $1 \times 10^{16}$  Xe<sup>+</sup>/cm<sup>2</sup> are obviously not exactly correlated with the direction of the external stress, applied in the  $\varphi = 0^\circ$  direction.

In Fig. 4.15 the development of the MOKE polar figures for the a) as-deposited, b) bent, c) irradiated and still bent and finally d) the relaxed case is shown. Comparing a) and b), no change can be seen at all. The anisotropy is induced by the implantation of xenon, as illustrated by the difference between b) and c). At this stage of the experiment the orientation of the anisotropy was not correlated with the external stress direction. The relaxation of the substrate did not affect the anisotropy direction, but slightly diminished its strength. Obviously, the external stress and the relaxation after ion irradiation had a minor influence on the orientation of the uniaxial anisotropy, contrary to the findings of Zhang [Zha01] for Ni films.

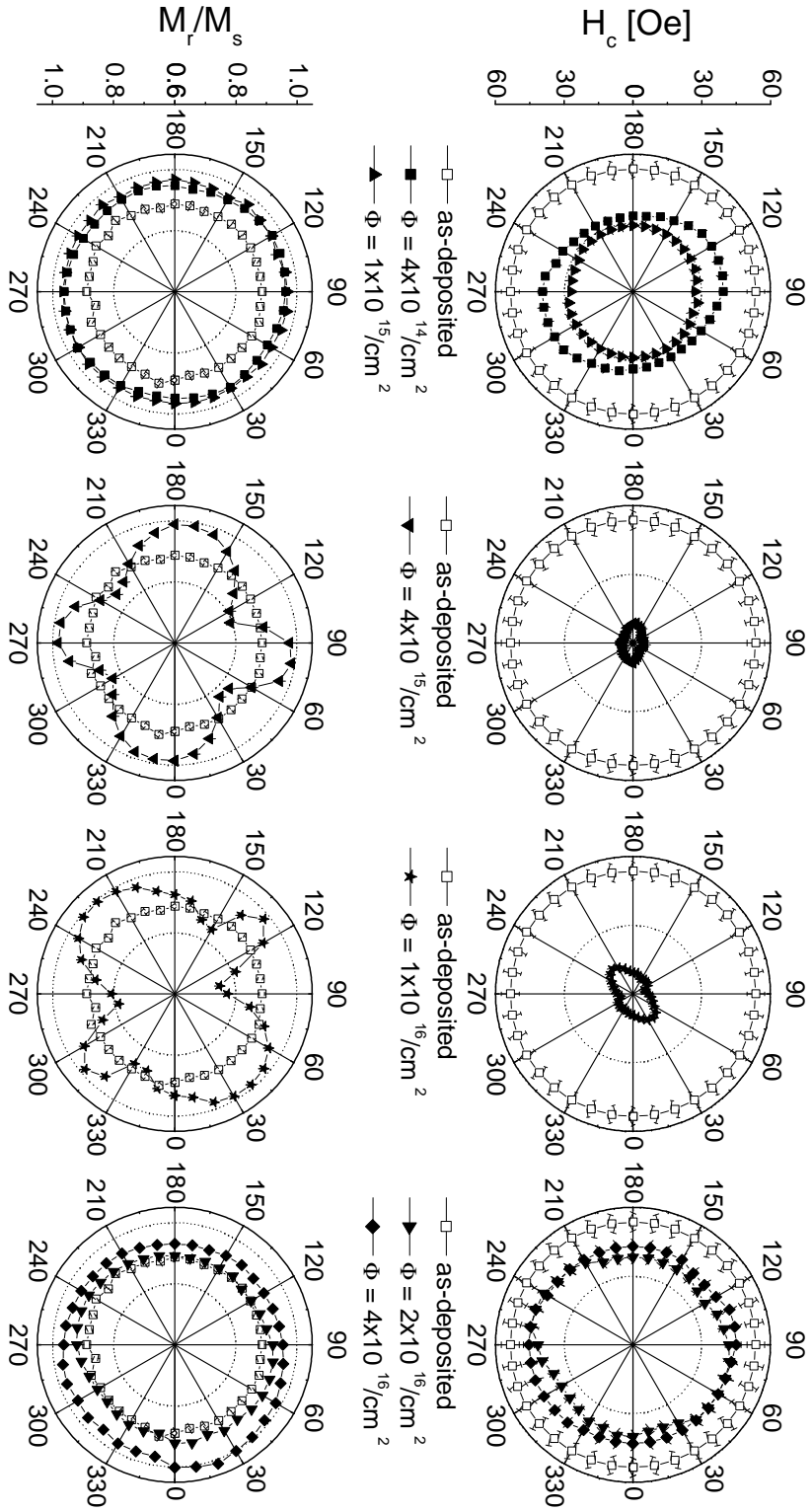


Figure 4.14: MOKe polar plots of the Fe/SiO<sub>2</sub> samples, irradiated under external stress ( $1/R \approx 1/\text{m}$ ) applied in 0° direction. The open squares refer to the as-deposited samples, all other points were measured after relaxing the irradiated sample. The uniaxial anisotropy is largest for  $4 \times 10^{15} < \Phi < 1 \times 10^{16} \text{ Xe}^+/\text{cm}^2$ .

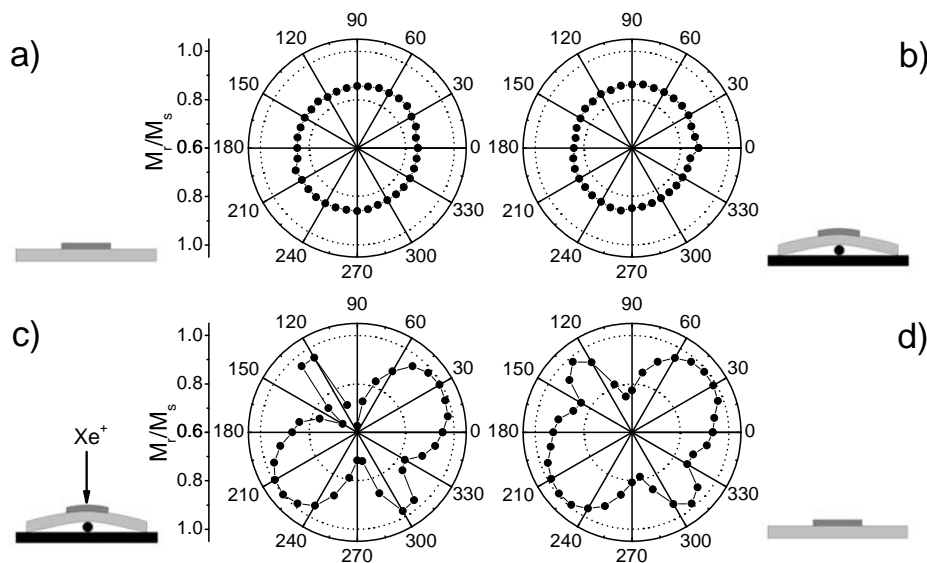


Figure 4.15: MOKE polar plots of the sample irradiated with  $1 \times 10^{16} \text{ Xe}^+/\text{cm}^2$ . a) as-deposited, b) as-deposited and bent, c) irradiated, but still bent, d) after relaxation of the external stress.

### 4.2.3 Influence of stress (MOMS)

Samples 1-I, 1-M and 1-S contain the  $^{57}\text{Fe}$  layer at the interface with the silicon (1-I), in the middle of the natural iron (1-M) and at the surface of the film (1-S) and thus they were used to perform a depth-dependent study of the influence of ion irradiation of stressed films on the spin distribution. The irradiation geometry and the stress were identical for all the samples.

The following abbreviations will be used in this context: first the sample (e.g. 1-M) was in as-deposited condition ( $1\text{-M}_{asdep}$ ). Then it was bent ( $1\text{-M}_{bent}$ ). After the bending, the sample was irradiated with  $1 \times 10^{16} \text{ Xe}^+/\text{cm}^2$ , but not yet released ( $1\text{-M}_{irr}$ ) and finally it was relaxed in irradiated condition ( $1\text{-M}_{relaxed}$ ). A magnetized sample, like for instance 2-S in the following section, will be called  $2\text{-S}_{mag}$ .

For the study of the magnetic properties, the specimens were characterized immediately after deposition by MOMS. Several spectra were recorded in standard MOMS geometry ( $\alpha = 45^\circ$ ,  $\Delta\varphi = 10^\circ - 30^\circ$ ). Additionally, hysteresis loops (as-deposited) were measured, varying the angle  $\varphi$  between the external magnetic field and the long axis of the sample in steps of  $\Delta\varphi = 20^\circ$ . After finishing also the structural analysis (RBS and XRD), the specimens were ion implanted and the characterization procedure was repeated (MOMS, MOKE, XRD, RBS).

The CEMS spectra and the resulting MOMS oscillation of  $1\text{-M}_{relaxed}$  have already been shown in Fig. 3.10. The graphs containing  $I_2/I_3$  of samples 1-I and 1-M in as-deposited and irradiated condition are presented in Figures 4.16 and 4.17, e) and f), and all corresponding fit parameters are summarized in Table 4.5. The as-deposited samples show a different behavior: while in  $1\text{-M}_{asdep}$  the spins are randomly distributed in the sample plane, in  $1\text{-I}_{asdep}$  and  $1\text{-S}_{asdep}$  one

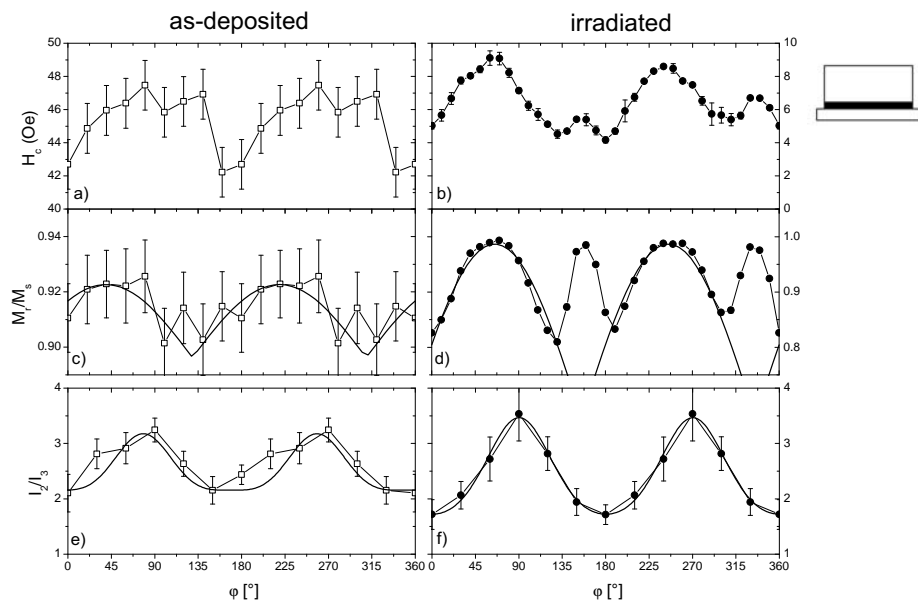


Figure 4.16: Sample 1-I: results of MOKE(a,b,c,d) and MOMS (e,f). The thick solid lines describe the fits as explained in the text. The sketch in the top right-hand corner indicates the position of the  $^{57}\text{Fe}$  marker layer (black).

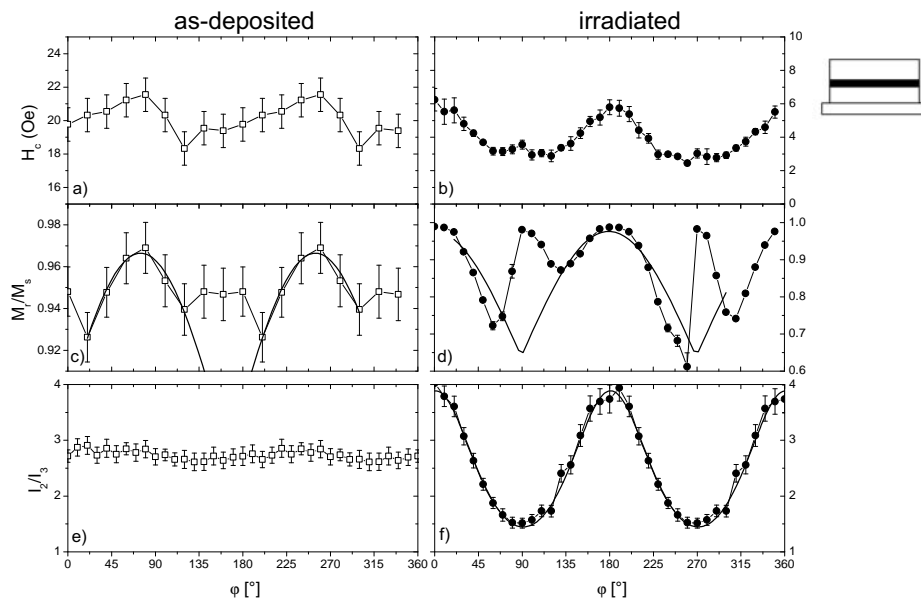


Figure 4.17: Sample 1-M: results of MOKE(a,b,c,d) and MOMS (e,f). The thick solid lines describe the fits as presented in the text.



Sample	MOMS fit				Exp. $c_{op}$ [%]	MOKE fit		
	$\psi_a$ [°]	$c_a$ [%]	$c_b$ [%]	$c_{op}$ [%]		$R_0$	$\varphi_0$ [°]	$R_D$
1-I <sub>asdep</sub>	78(8)	69(5)	31(5)	0(0)	0(7)	0.896(4)	39(5)	0.026(6)
1-I <sub>relaxed</sub>	90(3)	80(2)	15(2)	5(2)	0(3)	0.672(15)	65(4)	0.315(20)
1-M <sub>asdep</sub>	—	—	—	—	—	0.870(4)	75(4)	0.096(5)
1-M <sub>relaxed</sub>	0(3)	93(2)	4(2)	3(2)	1(4)	0.639(26)	-1(3)	0.337(34)
1-S <sub>asdep</sub>	136(4)	74(2)	26(2)	0(0)	0(2)	—	—	—
1-S <sub>relaxed</sub>	71(3)	80(2)	20(2)	0(0)	0(2)	0.633(25)	95(5)	0.347(30)

Table 4.5: MOMS and MOKE fit parameters of specimens 1-I, 1-M and 1-S.  $\psi_a$  is the angle between the strongest in-plane hyperfine field component ( $c_a$ ), found from sextet 1 ( $F_1$ ) and the axis of stress during irradiation.  $c_b$  is perpendicular to  $c_a$  and  $c_{op}$  is the out of plane component of the hyperfine field. Error 0 for  $c_{op}$  indicates that the free fit resulted in  $c_{op} < 0$ , therefore  $c_{op}$  was fixed during the fit.  $R_0$  is the isotropic component of the MOKE fit and  $\varphi_0$  and  $R_D$  are the easy axis direction and the uniaxial component.

preferred spin direction is measured. After bending, irradiating and relaxing the samples, a stronger spin alignment was observed in all specimens. These directions  $\psi_a$  are neither correlated to the values measured on the as-deposited specimen nor to the axis of stress during irradiation. Similar to the results of section 4.2.2, the preferred direction seems to be independent from the axis of maximum stress.

The results of the MOKE analysis are summarized in the right-hand part of Table 4.5 and illustrated for 1-I and 1-M in Figs. 4.16 and 4.17 a) - d). The as-deposited samples revealed nearly isotropic remanence and coercivity behavior. To visualize the small variations, the scales in Figs. 4.16 and 4.17 a) and c) are strongly expanded. The coercive field shows a slight deviation from isotropy in all the samples, which is in agreement with the MOMS results and is therefore an indication of a very small in-plane deposition anisotropy.

The MOKE data illustrated in Figs. 4.16 and 4.17 b) and d) show a uniaxial dependence of  $M_r/M_s$  and  $H_c$  on  $\varphi$ , induced by the  $\text{Xe}^+$  irradiation. Like in the preceding paragraph, one can observe the effect of a square-shaped hysteresis loop in the hard axis of magnetization and the triangular loops around this direction. In order to get the in-plane orientation of the easy axis of magnetization after the ion irradiation, the uniaxial and isotropic part of the remanence of the sample was fitted using the equation [Zha01]

$$\frac{M_r}{M_s} = R_0 + R_D \cdot |\cos(\varphi - \varphi_0)|, \quad (4.3)$$

where  $\varphi$  is the angle of  $H_{MOKE}$  during the measurements relative to the long axis of the film,  $\varphi_0$  the angle of the easy axis and  $R_0$  and  $R_D$  are the isotropic and the uniaxial anisotropic contribution to the remanence. The resulting values for  $R_0$ ,  $\varphi_0$  and  $R_D$  are summarized in Table 4.5. According to these fits,  $\varphi_0$  is not correlated with the axis of external stress during implantation for 1-I<sub>relaxed</sub> and 1-S<sub>relaxed</sub>. Only for sample 1-M<sub>relaxed</sub>, both the stress direction and the easy axis of magnetization in MOKE and MOMS analysis agree with each other.

According to the domain theory, films of thicknesses  $\lesssim 80$  nm with an in-plane anisotropy have a two-dimensional domain structure, which means that the domains extend from the surface to

the interface. Consequently, the results of MOMS and MOKE should be independent of the position of the  $^{57}\text{Fe}$  marker layer. Comparing the angles of easy axis  $\varphi_0$  (MOKE) and preferred spin direction  $\psi_a$  (MOMS), they turn out to be not exactly the same for samples 1- $I_{relaxed}$  and 1- $S_{relaxed}$ . As the deviation is too large to be explained by an inaccurate sample mounting, the effect must have a different origin. In 1-S, the sample volumes measured by means of MOMS and MOKE overlap (MOMS measures the whole surface area and MOKE measures only a small spot). Thus, the difference in  $\varphi_0$  and  $\psi_a$  seems to be a local variation of the magnetization direction. Probably the magnetic ripple structure (see section 5.1) of the polycrystalline film is responsible for the observed small deviation from theory.

In the experiments on 1-S, 1-M and 1-I, no correlation between the stress, applied during the ion irradiation, and the easy axis direction after sample relaxation was found. As for these specimens the first MOMS measurement was followed by MOKE, all samples were magnetized in certain directions  $\varphi$  before ion irradiation. The influence of the stress on the easy axis orientation, separated from any magnetization effect, was measured on sample 2-M. This sample contains the  $^{57}\text{Fe}$  layer in the middle of the natural iron. By applying MOMS, the spin distribution and the direction of the easy axis is determined without interaction of the specimen with a magnetic field. Therefore, the spin-order is not disturbed and the sample is characterized as-deposited without being magnetized. By bending this "original" specimen and irradiating it, the influence of the external stress on the film during irradiation is separated from the magnetization influence.

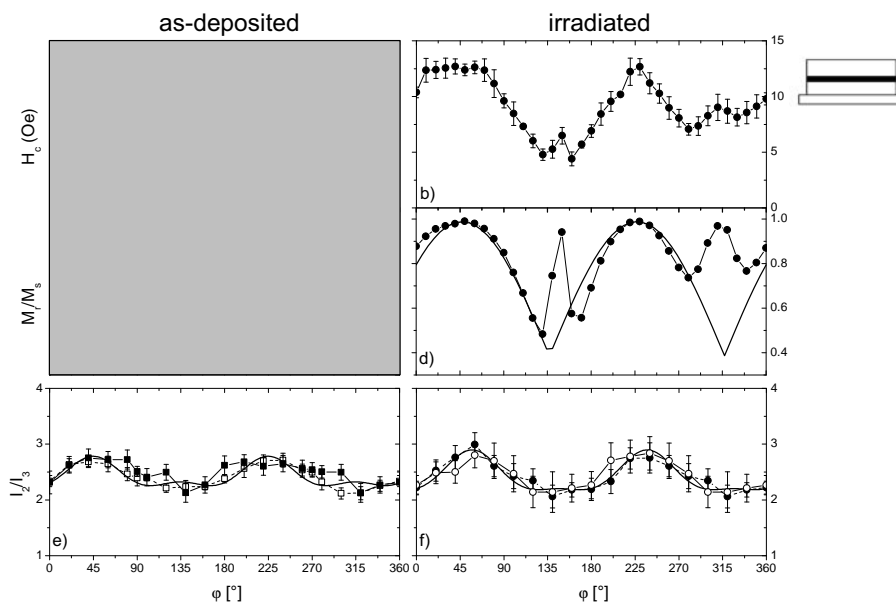


Figure 4.18: Sample 2-M: results of MOKE (b,d) and MOMS (e,f). e) MOMS results of the as-deposited (open symbols) and the bent sample (solid symbols). f) Measurements on the irradiated and still bent (open symbols) and relaxed state (solid symbols) of the specimen.

Sample	MOMS fit				Exp. $c_{op}$ [%]	MOKE fit		
	$\psi_a$ [°]	$c_a$ [%]	$c_b$ [%]	$c_{op}$ [%]		$R_0$	$\varphi_0$ [°]	$R_D$
2-M <sub>asdep</sub>	49(4)	56(2)	35(2)	9(2)	0(3)	—	—	—
2-M <sub>bent</sub>	57(6)	58(2)	42(2)	0(0)	3(4)	—	—	—
2-M <sub>irr</sub>	58(4)	59(2)	33(2)	8(2)	2(7)	—	—	—
2-M <sub>relaxed</sub>	58(4)	59(2)	33(2)	8(2)	2(7)	0.385(38)	47(5)	0.602(47)

Table 4.6: Sample 2-M: MOMS and MOKE fit parameters.  $\psi_a$  is the angle between the strongest in-plane hyperfine field component with intensity ( $c_a$ ) and the axis of stress during irradiation.  $c_b$  is perpendicular to  $c_a$  and  $c_{op}$  is the out of plane component of the hyperfine field. The error 0 for  $c_{op}$  indicates that it was fixed in the final fit.  $R_0$  is the isotropic component of the MOKE fit and  $\varphi_0$  and  $R_D$  are the easy axis direction and the uniaxial component.

Several CEMS spectra were recorded directly after deposition in standard MOMS geometry ( $\alpha = 45^\circ$ ,  $\Delta\varphi = 20^\circ$ ). After the RBS and GIXRD characterization, the film was bent to  $1/R \approx 1/\text{m}$  and again the spin distribution was controlled by means of MOMS. In the next step, sample 2-M was irradiated with  $1 \times 10^{16} \text{ Xe}^+/\text{cm}^2$  without applying an external magnetic field  $H_{impl}$  and again measured by MOMS in bent condition. Then it was relaxed and characterized by means of MOMS, RBS, GIXRD and finally MOKE.

In addition to the sextet and doublet sites normally used for the CEMS analysis, for this experiment a singlet site had to be added to fit the data of 2-M<sub>bent</sub>. This requirement might be due to the stress exerted on the film. This site reveals a center shift of  $\delta = -0.12(1) \text{ mm/s}$  and thus is in agreement with the results of Taylor [Tay91] on the hcp-stress phase of iron. All the hyperfine parameters used to fit the CEMS spectra can be found in Table B.1 (appendix).

Figs. 4.18 e) and f) show the MOMS results  $I_2/I_3(\varphi)$  in as-deposited and irradiated condition. The open symbols in graph e) were measured on 2-M<sub>asdep</sub> and the solid symbols on 2-M<sub>bent</sub>. Figure f) contains the measurements on 2-M<sub>irr</sub> (open) and 2-M<sub>relaxed</sub> (solid symbols). For all MOMS measurements the preferred spin directions were in the range of  $\psi_a = 53(5)^\circ$  and also the intensities  $c_a = 57(2)\%$  were identical within the errors. Keeping in mind that the film was not exposed to any magnetic field before the MOMS measurement of 2-M<sub>relaxed</sub> was finished, and that the orientation of the MOMS oscillation did not change after the beginning of the measurement procedure, the direction of the uniaxial anisotropy is determined by the deposition anisotropy. This direction is not changed due to the bending of the substrate, the irradiation and the relaxation process. The parameters  $\psi_a$ ,  $c_a$ ,  $c_b$  and  $c_{op}$  are summarized in Table 4.6.

The MOKE measurement, which is illustrated in Figs. 4.18 b) and d), showed that uniaxial anisotropy was induced by  $\text{Xe}^+$  irradiation. Again, one can observe the effect of a square-shaped hysteresis loop in the hard axis of magnetization and the triangular loops around this direction. The resulting values for  $R_0$ ,  $\varphi_0$  and  $R_D$  are given in Table 4.6. Obviously, the uniaxial anisotropy was parallel to the preferred spin direction in M<sub>asdep</sub>:  $\varphi_0 = 47(5)^\circ$ . For the other MOMS measurements it was within the error or slightly deviating.

The results on 2-M allow the conclusion that the easy axis orientations of 1-I, 1-M and 1-S are not correlated with the bending of the substrate. The same effect was observed in the experiments described in section 4.2.2.

#### 4.2.4 Influence of pre-magnetization (MOMS)

In this section special attention has been paid to the direction of the sample magnetization during ion irradiation. For this purpose, the specimens 2-S<sub>asdep</sub> and 2-B<sub>asdep</sub> were analyzed by means of MOMS, MOKE, RBS and GIXRD. After finishing all characterizations of the as-deposited samples, both samples were magnetized in the direction perpendicular to  $\psi_a$ , as found in the preceding MOMS analysis. This was  $\psi_a = 100^\circ$  for sample 2-S and  $\psi_a = -10^\circ$  for sample 2-B. Thereafter, 2-S<sub>mag</sub> was bombarded without being bent. Sample 2-B<sub>mag</sub> was also in remanence, but irradiated in bent condition.

Fig. 4.19 shows the results for 2-S. In 2-S<sub>asdep</sub>, represented by the open squares, the angle  $\psi_a$  is  $11(5)^\circ$  according to the fit. The solid symbols present the measurement of 2-S<sub>mag</sub>, magnetized in  $100^\circ$  direction. The angle  $\psi_a$  as found by the MOMS fit is  $90(4)^\circ$  and thus differs slightly from the expected  $\psi_a = 100^\circ$ . The MOKE measurement yielded no significant information about magnetic anisotropy, neither in  $H_c$  nor in  $M_r/M_s$ . As presented in section 4.2.2, the as-deposited samples reveal a remanence behavior which is isotropic within the errors. To show the small variations, the scales in Figs. 4.19 a) and c) are strongly expanded.

Fig. 4.19 f) illustrates the MOMS analysis after irradiation. The angle  $\psi_a = 88(4)^\circ$  did not change significantly and also the amplitude  $c_a = 0.67(2)$  of the MOMS oscillation remains the same as compared with the magnetized specimen. The correlated MOKE measurement shows a pronounced anisotropy with the easy axis in the direction  $\varphi_0 = 93(4)^\circ$ , which is the direction of the maximum in the spin distribution.

The MOMS and MOKE results for sample 2-B are illustrated in Fig. 4.20. The open symbols in e) are from 2-B<sub>asdep</sub> and show a preferred hyperfine field direction  $\psi_a = 80(4)^\circ$ . This is exactly the direction of the weak anisotropy that can be seen in the plot of  $H_c$  in a). Before irradiation

Sample	MOMS fit				Exp. $c_{op}[\%]$	MOKE fit		
	$\psi_a[^\circ]$	$c_a[\%]$	$c_b[\%]$	$c_{op}[\%]$		$R_0$	$\varphi_0[^\circ]$	$R_D$
2-S <sub>asdep</sub>	11(5)	66(3)	26(3)	8(4)	8(7)	0.897(1)	61(8)	0.010(2)
2-S <sub>mag</sub>	90(4)	66(2)	12(2)	22(3)	5(4)	—	—	—
2-S <sub>irr</sub>	88(4)	67(2)	13(2)	20(3)	8(7)	0.432(16)	93(4)	0.544(20)
2-B <sub>asdep</sub>	80(4)	51(2)	23(2)	25(2)	2(4)	0.950(1)	69(8)	0.004(1)
2-B <sub>mag</sub>	174(3)	78(2)	13(2)	9(2)	7(4)	—	—	—
2-B <sub>irr</sub>	179(5)	65(3)	35(3)	0(2)	1(7)	—	—	—
2-B <sub>relaxed</sub>	174(4)	66(2)	31(2)	3(2)	0(2)	—	—	—

Table 4.7: Samples 2-S and 2-B: MOMS and MOKE fit parameters.  $\psi_a$  is the angle between the strongest in-plane hyperfine field component with intensity ( $c_a$ ) and the axis of stress during irradiation.  $c_b$  is perpendicular to  $c_a$  and  $c_{op}$  is the out of plane component of the hyperfine field. The error 0 for  $c_{op}$  indicates that the free fit resulted in  $c_{op} < 0$ . Therefore,  $c_{op}$  was fixed during the fit.  $R_0$  is the isotropic fit component of the MOKE fit and  $\varphi_0$  and  $R_D$  are the easy axis direction and the uniaxial component.

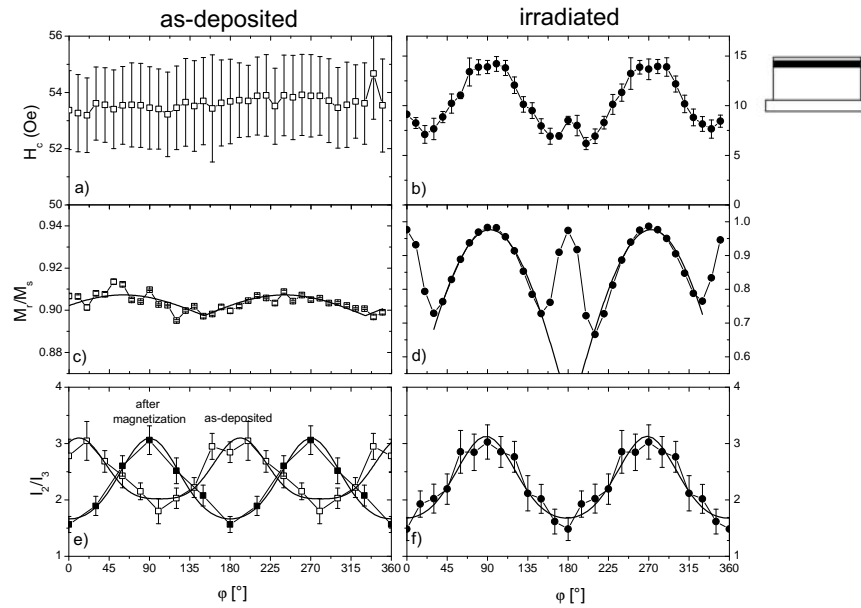


Figure 4.19: Sample 2-S: results MOKE (a,b,c,d) and MOMS (e,f). e) MOMS-results of as-deposited (open symbols) and magnetized sample (solid symbols). f) MOMS in irradiated state is plotted. The solid lines represent the fits.

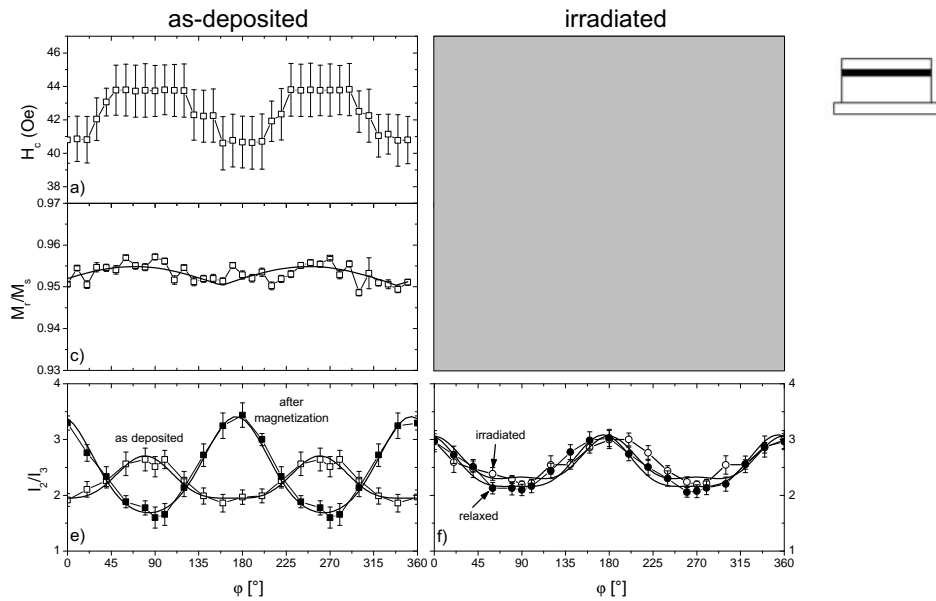


Figure 4.20: Sample 2-B: results MOKE (a,c) and MOMS (e,f). e) MOMS-results of as-deposited (open symbols) and magnetized sample (solid symbols). f) MOMS in irradiated state is plotted. The solid lines represent the fits.

the sample was magnetized in  $-10^\circ$  direction and then it was remeasured by means of MOMS. Similar to the observation on 2-S, the angle  $\psi_a$  did not change exactly to  $-10^\circ$ , but to  $174(3)^\circ$  (or  $-6(3)^\circ$ ), which is slightly outside the error.

The spin alignment in this direction is still present after irradiation and relaxation; only the amplitude has decreased from  $c_a = 0.78$  in magnetized condition to  $c_a = 0.66$  after ion bombardment. The final MOKE analysis is missing due to the destruction of the sample during the complicated treatment. All MOKE and MOMS results for 2-S and 2-B are summarized in Table 4.7.

#### 4.2.5 Crystallographic structure

In addition to the MOKE, MOMS and RBS analysis a detailed XRD study was performed for all as-deposited and irradiated samples. The objective was to gain information on the change of the lattice constant due to the ion irradiation and a possible variation of the lattice constant, measured parallel and perpendicular to the applied mechanical stress (long axis of the sample). In this context, experiments in  $\theta - 2\theta$  (rotating sample) and in grazing incidence geometry ( $\alpha = 2^\circ$ , see section 3.4.1), were performed.

Besides the very large peak of Si(400), the  $\theta - 2\theta$  spectra of the  $^{nat}\text{Fe}/\text{SiO}_2$  films only show the (110) reflex of bcc iron ( $2\theta_{\text{Fe}(110)} \approx 44.7^\circ$ ), indicating a crystallographic out-of-plane texture. The ion irradiation shifted the Fe(110) line toward smaller angles and, additionally, the width at the half maximum (FWHM) of the line decreased which might be caused by grain growth or the relaxation of micro-stress. The angle shift increased up to the fluence of  $\Phi = 1 \times 10^{16} \text{ Xe}^+/\text{cm}^2$ .

The changes in the peak position as well as in the FWHM are summarized in Table 4.8.

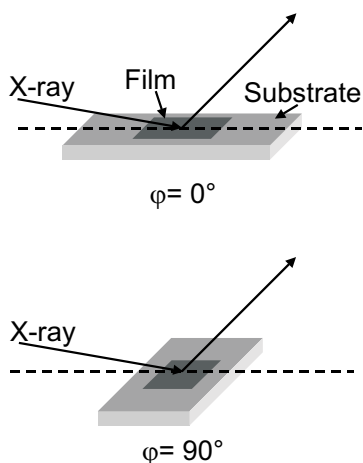


Figure 4.21: Sample-X-ray geometries of the GIXRD experiments, performed for all "1" and "2" specimens.

$\theta - 2\theta$  scans were also performed on the samples containing  $^{57}\text{Fe}$ , finding again the bcc Fe(110) peak at  $2\theta \approx 44.7^\circ$ . However, in these films the texture was very weak, resulting in low peak intensity. In order to increase the count rate and to measure besides the (110) also the (200) and the (211) reflection, a GIXRD study was done. During implantation the substrates were bent in  $0^\circ$  direction. Thus, rather than rotating the specimens, the spectra were measured for two different orientations of sample and incident X-ray beam. As illustrated in Fig. 4.21, in the first geometry the X-ray beam was parallel to the  $\varphi = 0^\circ$  direction and in the second it was perpendicular ( $\varphi = 90^\circ$ ). According to the technique used in section 4.1.3, a resulting inhomogeneous stress state after relaxation of the irradiated sample would cause different peak positions in the two directions.

The peaks of bcc Fe(110) ( $2\theta = 44.7^\circ$ ) and Fe(211) ( $2\theta = 82.2^\circ$ ), measured on sample 2-M<sub>relaxed</sub>, are illustrated in Fig. 4.22. In addition to these reflexes also the weak line of Fe(200) was measured at  $2\theta = 65.0^\circ$ . After fitting the peaks

$\Phi$ [ $\text{Xe}^+/\text{cm}^2$ ]	as-deposited			irradiated		
	$2\theta$ [ $^\circ$ ]	FWHM [ $^\circ$ ]	$a$ [ $\text{\AA}$ ]	$2\theta$ [ $^\circ$ ]	FWHM [ $^\circ$ ]	$a$ [ $\text{\AA}$ ]
$1 \times 10^{15}$	44.686(9)	1.003(30)	2.866(1)	44.769(13)	0.725(41)	2.861(2)
$4 \times 10^{15}$	44.893(9)	0.730(28)	2.853(1)	44.576(10)	0.560(32)	2.872(1)
$10 \times 10^{15}$	44.863(9)	0.723(31)	2.855(1)	44.499(13)	0.550(45)	2.877(2)

Table 4.8:  $2\theta$  diffraction angles with FWHM and corresponding lattice constants for bcc Fe(110), obtained after different irradiated fluences.

with a symmetric Pearson VII function, no significant difference in the peak position or in the peak intensity and width was found for the two geometries.

From the peak positions, the lattice constants derived from the different crystallographic directions of the iron were obtained and plotted versus the angle  $\varphi$  between X-ray and  $0^\circ$ -axis of specimen 2-M (see Figure 4.23). All the lattice constants of the as-deposited film (open symbols) were smaller than in bulk iron and they showed a general increase caused by the xenon implantation (solid symbols). In addition the derived  $a$  for the different crystallographic directions vary significantly in  $2\text{-M}_{asdep}$  and noticeably in  $2\text{-M}_{relaxed}$ . This deviation is a good indicator of in-plane strain caused by stress (see section 4.1.3). Nevertheless, it is very important that the lattice constants in both sample-X-ray orientations are the same within the error for all measured peaks. Thus, only the stress states of the film as-deposited and after ion implantation differ, but no significant difference can be found between the analyzed geometries.

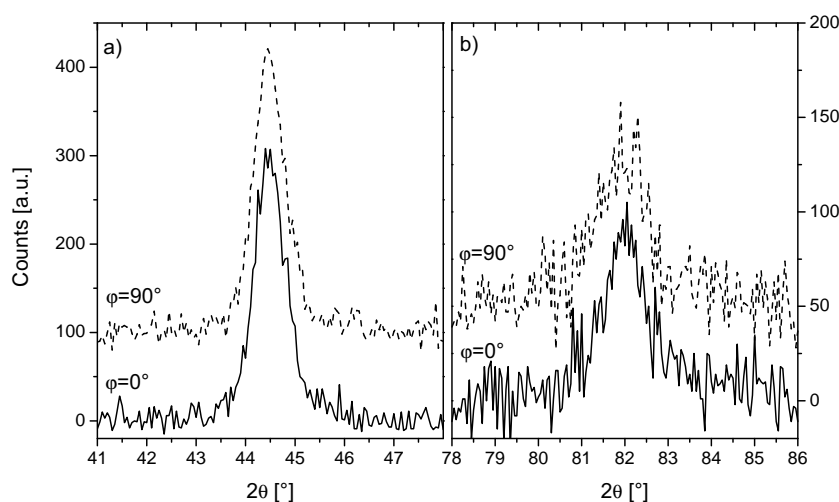


Figure 4.22: GIXRD peaks of sample 2-M for the two geometries  $\varphi = 0^\circ$  and  $90^\circ$ . The peaks are identified as: bcc Fe(110) ( $2\theta \approx 44.7^\circ$ ) and Fe(211) ( $2\theta \approx 82.2^\circ$ ).

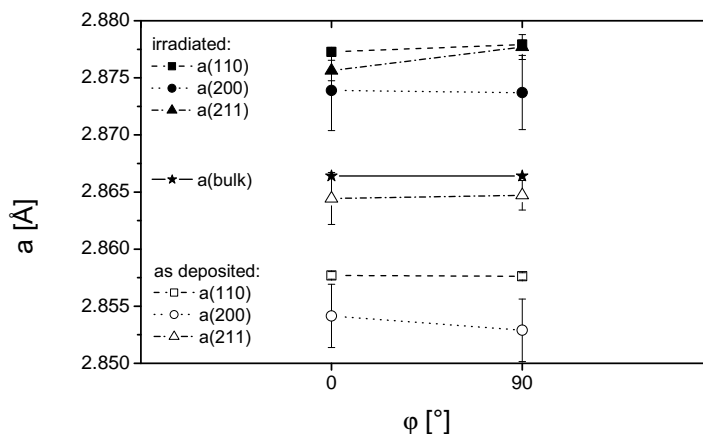


Figure 4.23: Comparison of the derived lattice constants  $a$  for different crystallographic directions and different sample-X-ray geometries (see Fig. 4.21) measured in sample 2-M. The open symbols are the constants of the as-deposited film, the solid symbols are of the irradiated specimen.

### 4.3 Summary

In the previous two sections the influence of ion irradiation on electron-beam deposited Fe films on Si(100) or SiO<sub>2</sub> was investigated for various external conditions and with different projectiles. The experimental results can be summarized as follows:

1. Irradiation of electron-beam deposited Fe/Si(100) films in a magnetic field with noble gas or iron projectiles induces uniaxial anisotropy. In addition to the easy axis a minor effect of a second energy minimum in hard axis direction was observed.
2. The change of  $K_u$  with increasing ion fluence depends on the projectile mass. For noble gases, it is faster for heavier projectiles and for self irradiation it has a stronger effect than expected for this mass (as compared to Kr<sup>+</sup>).
3. External stress during irradiation or due to relaxation of the irradiated film plays a minor role for the anisotropy direction.
4. The main parameters, determining the easy axis direction  $\varphi_0$  are deposition anisotropy (in case the sample is not magnetized before or during the irradiation) and the magnetization state or the external saturation field during the irradiation.
5. Generally, the high coercivity  $H_c$  of an as-deposited electron-beam evaporated Fe film decreases with increasing ion fluence, but rises again for a large fluence of heavy projectiles. Again this effect depends on the projectile mass.
6. The high deposition stress is relaxed by irradiation and nearly saturates for high fluences



at a weak compressive stress. No inhomogeneous in-plane stress, resulting from the sample bending during irradiation, was found after irradiating and relaxing the sample.

7. The irradiation produces a large number of defects in the film. The change in coordination number  $N_1 + N_2$  in first approximation does not depend on the implanted ion species, suggesting that only a small amount of projectile inclusions is present in the film.
8. The lattice constant decreases for small ion fluences ( $\lesssim 7.5 \times 10^{15}$  ions/cm<sup>2</sup>), but becomes similar to the as-deposited value for further irradiation.
9. The lattice parameter  $a_{\perp}$  increases after irradiation with  $\Phi < 1 \times 10^{16}$  Xe<sup>+</sup>/cm<sup>2</sup>.

# Chapter 5

## Discussion

The experimental results of the previous chapter gave a broad overview of the irradiation-induced effects on the magnetic and structural properties of the iron films. Before correlating these results in terms of macroscopic and microscopic effects, the symmetry of the observed magnetic anisotropy will be discussed in section 5.1. Section 5.2 contains a detailed discussion of the different stresses involved in the experiments presented, in comparison with results obtained for Xe irradiated Ni films. Other possible contributions to the orientation of the anisotropy will be discussed in section 5.3. Finally, a microscopical model for ion-beam induced magnetic anisotropy will be presented in section 5.4.

### 5.1 Symmetry of the magnetic anisotropy

The MOKE polar diagrams presented in chapter 4 show two axes perpendicular to each other, having a high remanence and a high coercivity. Around one of these axes triangular hysteresis loops are observed and the angular range of high  $M_r/M_s$  is usually quite small (20 - 30°) for this. The other high remanence axis shows the typical easy axis behavior of a uniaxial anisotropy with a  $\sin^2 \varphi$  dependence. This observation suggests that the origin of the high remanence is not the same in the two directions.

Zhang observed a similar phenomenon for xenon irradiated Ni films [Zha01]. These films had a uniaxial anisotropy and in the hard axis direction a high remanence occurred in a narrow  $\varphi$  region of 5 - 10° - typically only one point in the polar diagram. This observation was interpreted as a coupled fourfold (magnetocrystalline) and uniaxial anisotropy (induced by internal stress) [Zha01, Zha03a, Lie01].

Several arguments contradict this interpretation. First of all, to obtain a reasonable contribution of the magnetocrystalline anisotropy and, consequently, a classical fourfold symmetry, the film must show a pronounced in-plane texture which was not observed for the Ni films, as evidenced by pole-figure measurements. A second argument is that neither for nickel films nor for iron films the second high-remnance axis shows a  $\sin^2(2\varphi)$  behavior, which is expected for a classical fourfold energy term. In addition, the angular range showing the increased  $M_r/M_s$  is not the same for the different specimens. Finally, the loops measured around the second high-remnance axis are of triangular shape with a high-remnance and a low-remnance branch (see Fig. 4.4), which would not be expected for a fourfold anisotropy. All these arguments suggest that the

present Fe samples do not show a coupled uniaxial and fourfold anisotropy.

Another possible explanation for the phenomenon is inherent in the method. By measuring the longitudinal MOKE, parts of the polar Kerr signal can also contribute to the measured signal [Yan93, Din00]. As the polar Kerr effect is by one order of magnitude larger than the longitudinal one, even a small polar component can influence the whole measurement. However, our experiments resulted in a symmetrical MOKE-signal which cannot explain the presence of the asymmetrical hysteresis curves [Yan93, Din00, Din01]. Moreover, the polar contribution can be separated from the longitudinal one by reverting the geometry of laser and optics [Din00]. This experiment was performed on one of the present films, but without identifying a polar contribution.

Several authors have observed second-order effects of the MOKE [Osg98, Yan00, Pos02], which makes the quantitative analysis of the hysteresis curves difficult. These second-order effects also result in asymmetric hysteresis loops [Zho90, Bla90], but no triangular shapes were observed as found here. Moreover, a correlation of the results presented here with this phenomenon is highly unlikely, because the incidence angle of the laser beam was  $\approx 50^\circ$  in the present experiments and the second-order effects are supposed to be reasonable for nearly perpendicular incidence [Osg98].

The most promising approach to explain the observed two high-remanence axes is related to the polycrystalline structure of the film and consequently to its magnetic ripple structure. As a result of the magnetocrystalline and magnetostriction anisotropy, the easy axis of magnetization is oriented in a different direction for each grain in a polycrystalline ferromagnetic film. The local direction of magnetization follows the statistical anisotropy fluctuations along the direction of the mean magnetization, forming the so-called "magnetic ripple" [Hof64, Rie74, Hof79]. The opening angle of the ripple - which is basically the largest angle between the local magnetization vectors - can be derived [Hof64] by solving the "ripple equation" (equation minimizing the energy contributions of all relevant magnetic energy terms) for a certain direction and strength of an applied external magnetic field. Hoffmann's theory was reproduced experimentally [Now84] and the model was expanded by different authors [Rie74, Now92].

The magnetic ripple has a strong influence on the magnetization process, especially in the hard axis direction of polycrystalline uniaxial anisotropic ferromagnetic thin films. The complete hysteresis process was described by Feldtkeller [Fel61] and later by Nowak [Now92, Now93]. For the analytical description, the Stoner-Wohlfahrt model with an additional term for the so-called "internal field"  $L(H)$  was introduced:

$$E(\varphi, H) = \frac{1}{2} M_s H_k \sin^2 \varphi - [H + L(H)] M_s \sin \varphi. \quad (5.1)$$

$\varphi$  is the angle between the vector of local magnetization and the anisotropy axis,  $M_s$  is the saturation magnetization,  $H_k$  is the uniaxial anisotropy field, and  $L(H)$  describes the so-called "internal field" during the magnetization process. Nowak found experimentally that the direction of  $L(H)$  in the hard axis magnetization process always follows the direction of the external magnetic field, which means that it inhibits coherent rotation of the magnetization to the easy axis direction and tends to constrain the direction of local magnetization to stay parallel to the hard axis. The origin of the internal stray field was found to be the variation of the local magnetization direction within the Néel walls and the concerned stray field.

When applying a strong magnetic field in the direction of the hard axis (Fig. 5.1 a) and slowly decreasing it, first the ripple structure will form and the local magnetization will fluctuate within an angle  $\varphi_r$  around the external field direction (b). By further decreasing the field, domains will nucleate separated by low-angle Néel walls. The magnetization rotates incoherently in the different domains as illustrated in Fig. 5.1 c). When the external field is zero, the domains have reached the so-called "blocking-state", in which they have an angle of nearly  $90^\circ$  relative to each other (c). The tails of the neighboring Néel walls - which are the regions around the wall core, in which the magnetization is rotating (d) - overlap strongly and produce the stray field which keeps the sample magnetization in the hard axis direction. Consequently, this is the origin of the high remanence point in the hard axis hysteresis loop. If the domain width is small, as for thick films, the overlap of the tails will be large and the remanence will be higher than for thin films. Very instructive domain pictures describing the hysteresis process presented here are depicted in [Now93, Hub00].

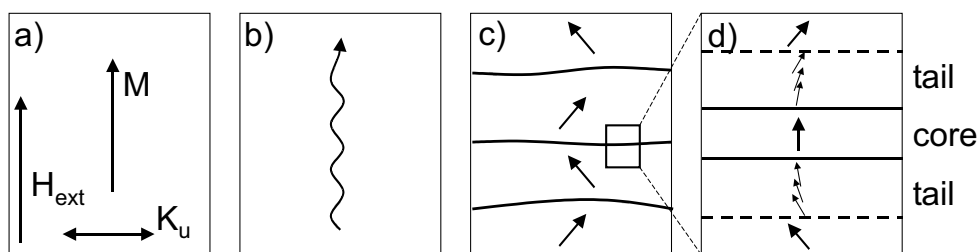


Figure 5.1: Illustration of the magnetization process in the hard axis direction of a polycrystalline uniaxial anisotropic film: a) saturation, b) magnetic ripple, c) incoherent rotation of domain magnetization ("blocking-state"), d) schematic structure of the low-angle Néel walls.

Such phenomenon is observed only in the hard axis direction. On the basis of the hard axis domain wall effect, the triangular hysteresis curves around this direction can be explained by the presence of a very small bias field  $H_0 = H_k \sin \alpha$  applied perpendicular to the external field.  $H_k$  is the anisotropy field of the specimen and  $\alpha$  the angle between the hard axis and  $H_{MOKE}$  [Bel70]. In the present iron films the anisotropy field  $H_k$  is usually quite small, in the order of 5 - 8 Oe, as found in the hard axis branch of the asymmetric hysteresis curves. A bias field of  $H_0 < 2$  Oe perpendicular to  $H_{MOKE}$  would explain the observed effect. Since  $H_k$  in the present iron films is much smaller than it was in the nickel films investigated by Zhang [Zha01] (it is even smaller than the coercive field), this effect is very strong for Fe, but almost not noticeable for Ni. A similar effect was also observed for permalloy films, which have a very small coercivity and anisotropy field [Gup03a].

To sum up, by taking into account a small bias-field perpendicular to  $H_{MOKE}$ , the electron-beam deposited iron films are uniaxially anisotropic after irradiation. The effect in the hard axis direction originates in the polycrystalline structure of the films, but is not correlated with an additional fourfold anisotropy term. Thus, the assumptions made in section 4.1.2 for fitting the normalized anisotropy constants are reasonable.

## 5.2 Influence of stress

Because stress was found to play a crucial role in anisotropy formation in Ni films [Zha01], the main findings on Ni will be briefly summarized before discussing the present results. Zhang suggested that the ion-beam induced magnetic anisotropy was closely related to the stress in the film. The as-deposited films, having a thickness of 75 nm, should be dominated by isotropic local stress coming from defects and grain boundaries. The irradiation with Xe<sup>+</sup> is supposed to reduce the residual stress and could also produce compressive stress due to the insertion of non-soluble xenon atoms into the lattice. The orientation of the induced anisotropy should be correlated with the direction of the induced compressive stress, and may depend on the incidence angle of the ions, the purity of the sample, and the orientation of the substrate.

Zhang explained the alignment of the magnetic anisotropy, caused by the relaxation process of the substrate, by introducing inverse magnetostriction into the free energy equation of the sample: when the specimen was bent before irradiation, a high tensile stress was applied. The stress induced strains in the film were reduced by implanting Xe<sup>+</sup>. The relaxation of the substrate led to a high compressive stress in the film and, consequently, to uniaxial magnetic anisotropy by inverse magnetostriction. A second term of the free energy was always observed after the irradiation of flat or bent samples that were not yet relaxed.

The summary given above allows the conclusion that one has to distinguish two kinds of stress: the external mechanical stress, induced by bending the substrate, and the microscopic stress in the film due to the ion-beam irradiation and the deposition process. As their influence is different, they will be discussed separately.

### 5.2.1 External mechanical stress

It was mentioned that two terms of the free energy determine the direction and size of the induced anisotropy [Zha01]. The first one is correlated with the relaxation of the substrate after implantation, and it was explained by inverse magnetostriction. The second one is the anisotropy observed at an ion irradiated sample that is not yet relaxed (see Fig. 4.15 c)); it is equivalent to the one after irradiating the film without application of external stress.

In the experiments on iron films, a perfect alignment of the magnetic anisotropy with the external mechanical stress can be found in only one case (1-M). In contrast to the findings on Ni films, the relaxation process from the irradiated (bent) sample to the relaxed state does not influence the direction of the easy axis, as illustrated in Figure 4.15 c) and d). Regarding the free energy term of the inverse magnetostriction effect (see equation (2.8))

$$E_{me} = -\frac{3}{2}\lambda\sigma\cos^2\varphi, \quad (5.2)$$

only the magnetostriction constant  $\lambda$  and the stress  $\sigma$  are decisive for the size of  $E_{me}$ .

In Table 5.1 the magnetostriction constants of the most important cubic ferromagnetic metals are summarized. For polycrystalline Ni,  $\lambda$  is about 8 times larger than for Fe and this might be one reason why the effect of the relaxation-induced stress does not contribute significantly to the results on iron films, while its contribution is strong in the case of nickel.

Another indication of the negligible role of the inverse magnetostriction effect for iron is the

Element	$\lambda_{100}$	$\lambda_{111}$	$\lambda$	Literature
bcc-Fe	20.7	-21.2	-4.4	[Chi64]
fcc-Ni	-45.9	-24.3	-32.9	[Chi64]
Fe <sub>0.18</sub> Ni <sub>0.82</sub>	$\approx 0$	$\approx 0$	$\approx 0$	[Boz53]
Fe <sub>0.5</sub> Co <sub>0.5</sub>	119.3	41.3	72.5	[Chi64]

Table 5.1: Magnetostriction constants of cubic ferromagnetic metals, all in  $10^{-6}$ .  $\lambda$  is the magnetostriction constant of the polycrystalline bulk material.

missing change of the polar diagram of  $M_r/M_s$  when just bending the specimens (see Figure 4.15 a) and b)). For nickel films a small anisotropy could be recognized perpendicular to the stress direction, as the magnetostriction constant  $\lambda_{Ni}$  is negative.

Apart from the studies on iron and nickel, similar experiments were conducted on permalloy films having a magnetostriction constant near zero. The analysis did not show any change of the anisotropy direction due to the relaxation process [Gup03a], which is in agreement with the results presented here.

Nevertheless, after the irradiation of about  $1 \times 10^{16}$  Xe<sup>+</sup>/cm<sup>2</sup>, all the iron films presented in section 4.2 show anisotropy, but the direction of the easy axis is different for all of them.

### 5.2.2 Microscopical stress

As described in section 4.1.3 a very large microscopic stress is present in the samples. The largest value is a tensile stress of 3.8(4) GPa after deposition, which is just under 2% of the Young modulus of iron. It is well known that nearly all metal films deposited by electron-beam evaporation show intrinsic tensile stress. Thornton [Tho89] predicts that the internal stress increases with a decreasing ratio of the substrate temperature to the melting point of the evaporated material  $T_s/T_m$ . For  $T_s/T_m < 0.2$ , a sharp increase in the intrinsic deposition stress was observed. The substrate holder in the chamber used for evaporation of the films is water-cooled, thus  $T_s$  is not lower than 10°C. According to Thornton for  $T/T_m = 283$  K/1800 K = 0.157 a stress of more than 1 GPa is possible. Additional important parameters are the base pressure during the evaporation, and the deposition rate which was about 3 Å/s in the present case. Typical values for the stress in iron films deposited on SiO<sub>x</sub>, MgF<sub>2</sub> or glass are between 1.3 and 1.6 GPa [Win91, Klo68]. However, several parameters are responsible for the intrinsic stress formation [Hof64] and because their values given in the literature vary, the measured very large stress of 3.8(4) GPa after deposition cannot be excluded.

Misra et al. observed for 150 nm thick films of the high temperature melting metal Cr that the large tensile residual stress after deposition was reduced significantly by irradiation with Ar<sup>+</sup> ions [Mis98]. A fluence of  $1 \times 10^{15}$  Ar<sup>+</sup>/cm<sup>2</sup> with an energy of 110 keV ( $R_p \approx 55$  nm) was sufficient to relax the stress completely and any further irradiation reversed the tensile deposition stress into compressive stress of the order of -1.0 - -1.5 GPa. The stress relaxation was explained by the reduction of voids in the grain boundaries of the film. The influence of substrate damage and amorphization was excluded as the reason for the stress reduction. The compressive

stress was interpreted to be a result of a net decrease in the interatomic distances in the bombarded films and in conclusion to repulsive forces between the atoms. The sketch in Fig. 5.2 illustrates this model: in the initial state the interatomic distance is still in the region of attractive interaction ( $r_i$ ). Due to a small irradiation fluence, a maximum tensile stress can be achieved ( $r_c$ ). Further irradiation induces a continuous decrease in the lattice parameter and finally leads to a zero stress state ( $r_0$ ). Any further irradiation causes a repulsive interaction. This interpretation is supported by molecular dynamics simulations in Ni and C films [Mue87, Mar96]. Misra's observations match the results presented in section 4.1.3. The deposition stress is relaxed after the irradiation at a fluence in the range between  $10^{15}$  and  $10^{16}$  ions/cm<sup>2</sup>, depending on the projectile mass. After this decrease, a saturation value is observed at  $\approx -1$  GPa of compressive stress. This value stays constant up to the highest implanted fluences. A decrease

in the stress-free lattice constant  $a_0$  is observed in the same fluence region as found by Misra (see Fig. 4.11).  $a_0$  as fitted by GIXRD, decreases for certain fluences up to  $7.5 \times 10^{15}$  ions/cm<sup>2</sup> and for higher fluences the interatomic distance increases again. The fluence range in which a small stress-free lattice constant  $a_0$  occurs depends on the projectile mass. For xenon, only the point at  $1 \times 10^{15}$  Xe<sup>+</sup>/cm<sup>2</sup> shows the pronounced decrease, then the lattice constant increases, reaching the deposition value. A qualitatively similar observation was made for the radius of the second iron shell  $a$  by EXAFS (see Fig. 4.9 b)): the stressed lattice constant does not change significantly for the irradiation fluences of  $\Phi = 1 \times 10^{16}$  and  $5 \times 10^{16}$  ions/cm<sup>2</sup>. However, all values of  $a$  are smaller than the ones of  $a_0$ .

Generally, a direct comparison of GIXRD and EXAFS results is critical for two reasons. Firstly, the radii of the second shell  $a$  resulting from EXAFS are the average lattice constants of the stressed lattice, and the results of the GIXRD stress-analysis  $a_0$  are the average lattice constants of the hypothetical, stress-free lattice. The lattice constant  $a_{\psi,average}$ , as illustrated in Fig. 4.11, is the average of the lattice constants measured for the crystallographic orientations (110), (200) and (211); thus the angle  $\psi$  is between 20° and 40° and  $a_{\psi,average}$  is similar to the out-of-plane lattice constant. To compare all these values, an accurate correction of  $a$  for the stress would be necessary. This is very complicated, because not only the in-plane stress and the resulting Poisson expansion or contraction has to be considered, but also the texture of the film plays a role because iron is not isotropic with respect to the Young modulus and the Poisson ratio. Secondly, GIXRD measures the absolute value of the lattice constant, while EXAFS is a relative method which requires a calibration sample. Therefore a quantitative discussion of the lattice constants is difficult in any case. In conclusion, the values of the GIXRD concerning the lattice constants are more reliable, while the procedure to obtain absolute values from EXAFS contains many sources of error. A comparative study for both methods was performed by Jaouen et al. [Jao01]. In their work, the stress-free lattice parameter was measured, and the value of  $a_0$  was

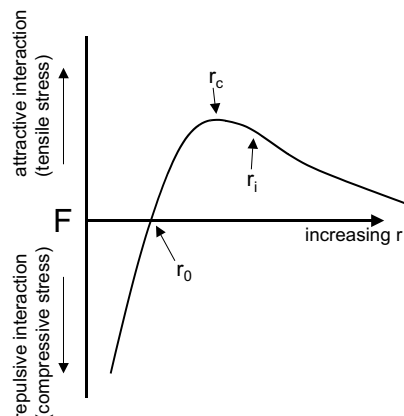


Figure 5.2: Illustration of the model, explaining the concept of compressive stress due to reduction of the interatomic distance.

found to be systematically larger in GIXRD than in EXAFS. This deviation was explained by the difference between the measurement of long-range and short-range effects. Possibly, also grain-size and, consequently, surface effects might play a role in this context.

However, the increase in the lattice constant for high irradiation fluences cannot be explained by the model presented above, since it occurs without a stress relaxation.

The magnetic parameter most sensitive to structural changes in the sample is its coercivity. The coercivity  $H_c$  strongly depends on the defect and grain structure and on the internal strains of the specimen [Kne62]. Because iron is difficult to deposit very purely, the foreign atoms may also contribute to the large value of  $H_c$  after deposition. The strong reduction in the coercivity in the electron-beam evaporated films is most probably correlated with the stress reduction due to ion irradiation. The corresponding effect in electron-beam evaporated nickel films was observed by Zhang [Zha01].

In addition to the reduction in the deposition stress, a possible slight increase in the grain size during ion bombardment (see section 4.1.2 and 4.2.5) might contribute to the reduction of the coercivity up to fluences of  $1 \times 10^{16} \text{ Xe}^+/\text{cm}^2$ . The increase in  $H_c$  for higher fluences (see section 4.2.2) might be correlated to structural irradiation damage and xenon inclusions remaining in the film. Kneller [Kne62] emphasizes the dependence of the magnetization and the coercive field on strong irradiation defects.

### 5.3 Influence of other external parameters

In section 5.2.1 it was concluded that the irradiation of electron-beam evaporated Fe films with  $1 \times 10^{16} \text{ Xe}^+/\text{cm}^2$  induces magnetic anisotropies, but the direction of the easy axis was different for all the films and could not be correlated with the external stress applied during ion implantation. Other external parameters that influence the orientation of the anisotropy will be discussed in the present paragraph.

**Influence of the deposition.** Specimen 2- $M_{asdep}$ , as presented in Figure 4.18, shows a preferred hyperfine field direction  $\psi_a$  measured by means of MOMS, which stays fixed during bending, irradiation and relaxation. The final MOKE measurement shows a uniaxial anisotropy with the easy axis oriented in the direction of the preferred hyperfine field (Table 4.6). This result suggests that the deposition process of the specimen is decisive for the anisotropy direction after irradiation if no magnetic field was applied before.

Several parameters are known to influence the magnetic anisotropy of as-deposited films, for instance small magnetic fields during deposition, or other deposition angles than  $90^\circ$  [Chi55]. Thus the electro-magnet of the electron-gun might be a reason for the observed magnetic anisotropy in the as-deposited sample as it is the only source of a magnetic field inside the deposition chamber. However, the strength of the magnetic field could not be measured or estimated. Another explanation could be a non-normal incidence of the condensating iron atoms: during the deposition, the substrates were fixed on a rotatable wheel to change the deposited sample [Har00]. That is why the angle between the crucible of the evaporator and the substrate is not fixed and varies up to  $10^\circ$ , possibly leading to magnetic anisotropy in the deposited films.

**Influence of the pre-magnetization.** Another parameter to be considered to explain the alignment of the uniaxial anisotropy for samples 2-S and 2-B is the magnetic field, applied during irradiation or annealing (see section 4.1 and [Zha01, Cha02, Woo02]). The results presented



in section 4.2.4 suggest that in a sample with an isotropic remanence of  $M_r/M_s > 0.9$  (Figs. 4.19 c) and 4.20 c)) the remanent magnetization is also sufficient to align the anisotropy. Regardless of the stress state of the sample, the irradiation of the magnetized samples 2-S and 2-B results in perfect agreement between the angles  $\psi_a$  measured before and after irradiation and relaxation. Taking into account that the samples of section 4.2.2 and 4.2.3 were magnetized by the MOKE measurement before the bombardment, the random orientation of  $\psi_a$  might be explained in this way: after the final MOKE measurement of the film, the sample was in remanent magnetization state and the following irradiation possibly aligned the easy axis of anisotropy in this particular direction.

The experiments discussed show that the alignment of the anisotropy can have several reasons. The direction of the anisotropy after irradiation without stress and external magnetic field is given by the deposition parameters. By applying an external magnetic field or by magnetizing the film this direction can be changed, but mechanical stress plays a minor role for the orientation of the easy axis in iron films.

## 5.4 Microscopical model for ion-beam induced anisotropy

In the preceding sections the parameters responsible for the orientation of ion-beam induced magnetic anisotropy were discussed from a macroscopical point of view. The influence of the external irradiation parameters were discussed, but the questions concerning the microscopic origin of the magnetic anisotropy were not answered. Therefore a careful study of the ion-beam induced changes in the sample structure is necessary. On the basis of these results possible reasons for magnetic anisotropy will be discussed.

### 5.4.1 Irradiation induced defects

In recent decades a large number of experiments have been performed on the production of defects in thin films by ion implantation. In particular the studies of Jenkins [Jen78, Jen93] and Kirk [Kir87] are interesting for the interpretation of the experiments presented here, as they deal with the irradiation of metal films with noble gases or self-ions. In agreement with [Rob83, Tem86], they found the formation of so-called "dislocation loops" as a result of the ion bombardment. Even some crystalline precipitates and bubbles of the implanted xenon ions ( $E = 350$  keV,  $\Phi = 1 \times 10^{16}$  ions/cm<sup>2</sup>) were observed in iron films [Tem86], exerting a pressure of up to 5 GPa on the lattice.

The production of dislocations strongly depends on the properties of the irradiated material and its crystallographic structure. While in bcc-iron films nearly no defects were found for self-irradiation fluences smaller than  $1 \times 10^{14}$  ions/cm<sup>2</sup>, but only for  $\Phi \gtrsim 10^{15}$  Fe<sup>+</sup>/cm<sup>2</sup>, fcc-metals like nickel or copper showed reasonable defect yields  $Y = N_L^v/N_c$  ( $N_L^v$  = number of visible vacancy loops per unit area,  $N_c$  = ion dose). Similar results were found for noble gas implantations. The formation of vacancy loops is generally explained by the collapse of collision cascades and the annealing of vacancies and interstitials. A collision cascade results in the local melting (thermal spike) of the cascade core, lasting some picoseconds [Sei87, Rub92]. Within the melt, the already consisting vacancies lose their individual identities to remain as density fluctuations.

Because the cascade starts to cool down from the outside, the atoms recrystallize coherently in this volume and the density fluctuation inside the still molten core increases. Finally, when the whole surrounding is crystalline, the low density core of the cascade will collapse to form the vacancy dislocation loop. The formation of interstitial dislocation loops was not observed for thin films; only a higher concentration of interstitial atoms in the periphery of the cascade was found in simulations. In conclusion, the most important parameters for the collapse of vacancy loops are: 1. the defect migration occurring during the thermal spike phase, 2. the thermal conductivity of the film material, 3. the cooling rate of the spike region which is correlated to the melting temperature, and 4. the initial vacancy configuration and concentration.

The mechanism described was suggested for Cu, Ni and  $\text{Cu}_3\text{Au}$  by Kirk et al. [Kir87]. According to their work, each collision cascade can result in the formation of a dislocation loop. Furthermore, these authors discovered that the defect yield increases with the projectile mass, but does not change with the ion energy for room-temperature irradiations.

The properties of Fe concerning the irradiation defects are different. For the creation of dislocation loops in iron, overlapping cascades and in conclusion much higher ion fluences are necessary. This effect might be explained by differences in the average thermal spike lifetimes which increases for overlapping collision cascades.

The important differences between the irradiations in the experiments of section 4.1 are the projectile mass, the deposited energy and the spike volume (see Fig. 2.3). The neon implantation produces only narrow and locally separated collision cascades, spread over a large volume of the specimen. Thus the vacancies are produced in a large volume, but the probability to collapse to form a vacancy loop is small due to the separation of the different higher order cascades. The xenon irradiation produces spatially overlapping spikes which allow for an effective production of dislocation loops. For krypton and iron irradiations the defect yield should lie between xenon and neon.

The EXAFS results suggest that during irradiation with  $1 \times 10^{16}$  ions/cm<sup>2</sup> the number  $N_1 + N_2$  decreases by 17(6)% and by 25(6)% for  $5 \times 10^{16}$  ions/cm<sup>2</sup>. Although the uncertainty of  $N_1 + N_2$  is rather large, the reduction seems to be the same for all the projectiles at the two measured fluences. Since EXAFS only accesses the  $N_i$  of the crystalline part of the film, no direct information about the defects in the grain boundaries can be obtained. However, according to Kirk, the production of dislocation loops depends on the projectile mass and because the decrease of  $N_1 + N_2$  is similar for  $\text{Fe}^+$ ,  $\text{Kr}^+$  and  $\text{Xe}^+$  irradiation in the grains, it seems to be possible that the efficiency of the defect production is different in the grain boundaries.

As presented in Table B.1, additional information concerning the ion-beam induced defects can be obtained from the Mössbauer parameters. In each specimen a decrease of the intensity  $F_1$  of the  $\alpha$ -iron site due to ion irradiation is found, whereas the fraction  $F_2$  of the sextet 2 with a reduced hyperfine field (due to defective environment) increases significantly. This is an indication of the number of defects that are created during ion irradiation.

#### 5.4.2 Correlation between structure and magnetism

The objective of the present paragraph is to present a model for changes in the sample magnetism corresponding to the structural modifications occurring in the specimens irradiated in

the presence of an external magnetic field. Magnetocrystalline or magnetoelastic anisotropy cannot be the origin of the observed effects. On the one hand, a pole figure analysis of one irradiated nickel film contradicts magnetocrystalline anisotropy of the film, and on the other hand GIXRD spectra in two sample-X-ray geometries (see Fig. 4.21) show no difference in the diffraction angles and line widths, in contradiction to magnetoelastic effects.

Several microscopical models were found to explain the effect of induced magnetic anisotropy. Nearly all of them are correlated with magnetic annealing or stress annealing experiments. Film treatments by annealing and ion irradiation only agree in some of their properties and it is important to keep these differences in mind when discussing the mechanisms of induced magnetic anisotropy. The "annealing time" of the ion irradiation is quite short, an irradiation of  $1 \times 10^{16}$  ions takes about 20 minutes and each single spike, which is essentially the annealed volume, has a lifetime of  $\lesssim 10$  ps. The temperature in a spike is far above the Curie-temperature and is locally also higher than the melting point. In this way, not only diffusion of vacancies or atoms can be enhanced, but also new vacancies and defects will form as a result of the irradiation. The publications on magnetic annealing experiments use temperatures up to 1300 K, applied for typically one hour. It was found that also the cooling rate - usually between 10 and 200 K/h - strongly affects the magnetic anisotropy constant which is large for rapid cooling treatment. During the whole time of annealing and cooling the magnetic field is applied.

Perhaps the most famous concept to explain the microscopic origin of the induced magnetic anisotropy is the one of "directional ordering", presented by Néel and Taniguchi [Nee53, Tan54]. Chikazumi [Chi55, Chi97] found a good quantitative agreement of this theory with the anisotropy effect of iron-nickel alloys: in a binary alloy with metals A and B three different kinds of dipoles can be formed, A-A, B-B and A-B. Considering that the energy of the dipole-dipole interaction is different for the three sorts of atomic pairs and that the atoms are arranged in directionally ordered manner, the total dipole-dipole alignment can result in magnetic anisotropy. Iron-nickel and other metallic alloys could be described by this theory in good quantitative agreement.

For materials consisting of only one element, the model has to be modified. Apart from the element A the vacancies can be considered as the second part B of the dipoles. In analogy to the directional order model for alloys, the anisotropy can be explained by the alignment of vacancies or anisotropic vacancy clusters in the crystal [Wil57]. Lesnik found that generally the amount of vacancies or non-magnetic impurities in the grains is too small to explain a large magnetic anisotropy effect [Les69, Les73]. He suggests that a non-uniform distribution of defects in the grain boundaries is the origin of the induced anisotropy. According to section 5.4.1 a large number of vacancies are introduced in the grain boundary by ion irradiation, and thus the magnetization in this volume decreases compared to the grain volume. The lattice imperfections connected with the vacancies in the grain boundary favor the diffusion of atoms along the boundaries, enhancing an alignment [Les73].

Antonov [Ant77] reached corresponding results for polycrystalline iron specimens, investigated by means of TEM, and postulated a model to fit his measured anisotropy constants. By assuming  $i$  vacancy clusters to have the shape of ellipsoids, he derived the effective anisotropy of a film by considering the shape anisotropy of these objects (see section 2.1.2):

$$E = \frac{1}{2} M_s^2 \sum_i v_i (N_{yi} - N_{xi}) \sin^2 \varphi_i.$$

$v_i$  are the volumes of the ellipsoids,  $N_{xi}$  and  $N_{yi}$  are the form factors and  $\varphi_i$  are the angles between the main axis of the respective ellipsoid  $i$  and the direction of the magnetization. Antonov derived different anisotropy constants for various concentrations, distributions, eccentricities and orientation distributions of voids. He obtained values of  $K_u \ll 10^3 - 2 \times 10^5$  erg/cm<sup>3</sup> for the anisotropy constant in 30 nm thick iron films.

The results which were presented in section 4.1.2 are in qualitative agreement with this theory. It was discussed that any kind of defect production in iron films starts at  $1 \times 10^{15}$  ions/cm<sup>2</sup>. Thus  $(K_u/M_s)_{irr}$  and the vacancy loop production can be assumed to change in the same way: they start to rise at fluences  $\Phi \approx 1 \times 10^{15}$  ions/cm<sup>2</sup> and the increase continues up to the highest implanted fluence.

Moreover, the efficiency of the vacancy loop formation is supposed to rise for increasing ion mass. The same happens with  $(K_u/M_s)_{irr}$ : the uniaxial anisotropy constant increases at smaller fluences and faster for irradiation with heavier ions (see Fig. 4.7 a)), similar to the defect production, as discussed above.

Another argument supporting the close connection between the formation of vacancy loops and the ion-beam induced anisotropy can be seen by comparing the fluence dependence of  $(K_u/M_s)_{irr}$  in nickel or permalloy with that in iron. Whereas for the first two metals even an ion fluence of  $\Phi < 4 \times 10^{14}$  Xe<sup>+</sup>/cm<sup>2</sup> is sufficient to induce the anisotropy [Zha01, Gup03a], for iron films this is only reached for  $\Phi > 4 \times 10^{15}$  Xe<sup>+</sup>/cm<sup>2</sup>. As discussed in paragraph 5.4.1 this observation corresponds well with the findings of different authors on the production of vacancy loops by ion irradiation in these metals.

It is possible to estimate the absolute value of the anisotropy constant in analogy to the work of Antonov. Considering the bulk saturation magnetization for bcc-iron,  $M_s = 1711$  emu/cm<sup>3</sup> [Sko99], the largest measured anisotropy constant ( $2.5 \times 10^{16}$  Xe<sup>+</sup>/cm<sup>2</sup>) of section 4.1.2 would be in the order of

$$4.1 \text{ Oe} \cdot 1710 \text{ emu/cm}^3 = 0.7 \times 10^4 \text{ erg/cm}^3. \quad (5.3)$$

This value is slightly smaller than the derived anisotropy constant for a film with spherical grains having an average anisotropy factor of  $a/b = 7$ .  $a$  and  $b$  are the half-axes of an average vacancy ellipsoid in the film [Ant77]. Thus the model reproduces the correct order of magnitude of the anisotropy observed in this work.

Besides the rising  $(K_u/M_s)_{irr}$  for increasing ion fluence, also a drop in the normalized anisotropy constant at  $\Phi = 5 \times 10^{16}$  Xe<sup>+</sup>/cm<sup>2</sup> is observed. This phenomenon cannot be explained yet; it might be correlated to a beginning amorphization of the iron caused by strong radiation damages. Additionally, the reduction of the film thickness as a result of the sputtering enhances the mixing process at the Fe/Si interface. The ions can penetrate the interface, producing probably a reasonable amount of iron-silicide. This might also influence the anisotropy of the sample. Similar effects have been presented for large fluences of gold ions implanted into permalloy films [Gup03a] and were explained by the increasing production of pinning centers, which reduce the uniaxial anisotropy and increase the coercive field.

To Summarize, the results of the experiments presented in chapter 4 indicate a possible relation between the rise in the uniaxial anisotropy constant  $(K_u/M_s)_{irr}$  and an efficient production of vacancy loops by the ion irradiation. However, a direct proof of this assumption by transmission electron microscopy (TEM) has not been given here.

## Chapter 6

# Effects of substrate and deposition method

Up to now this work has been focused on the magnetic and structural properties of polycrystalline iron films, deposited via electron-beam evaporation on Si(100) substrates. Some of the observed effects may be closely related to the deposition method, and it is interesting to check the influence of the implantation for films which are deposited with a different method. Moreover, the ion irradiation strongly affects the structural properties of the specimens by the production and removal of radiation damages. Thus, a study of its influence on the magnetic anisotropy of highly in-plane textured iron films is very attractive. In such experiments the induced magnetic anisotropy effects can be compared with the magnetocrystalline anisotropy. The pulsed laser deposition method (PLD) was chosen because it is known to produce highly textured films. The deposition on Si(100) enabled a comparison with the findings of the preceding chapters. To produce in-plane textured films, MgO(100) was used as a substrate because it is known that iron films can grow epitaxially on this material [Sub99].

After a short description of the deposition and the layer structure of the films in section 6.1, the results on the Fe/Si(100) system will be described (section 6.2). In section 6.3 the results on the iron films on MgO(100) are illustrated. In both sections MOMS and MOKE were applied in combination with XRD. A short discussion of the effects observed on PLD films and electron-beam evaporated films will be presented in section 6.4.

### 6.1 Deposition, ion irradiation and analysis

**Deposition.** All the iron films presented in this chapter were deposited by PLD and contain a 15 nm thick  $^{57}\text{Fe}$  layer located at a certain depth within the 75 nm thick films. The deposition method is the same for  $^{nat}\text{Fe}$  and  $^{57}\text{Fe}$  - while the films described earlier were a mixture of electron-beam and effusion-cell deposition - and thus no strains due to the different deposition methods should occur at the internal interfaces. Caused by the different energies of the deposited atoms or ions, the growth of the films is different for PLD than for electron-beam evaporation. First of all, a pure  $^{nat}\text{Fe}$  film on Si(100) was prepared for calibration purposes. After its deposition (25002 laser pulses) its thickness was measured by RBS to be 85 nm. During the evaporation of the 75 nm thick  $^{nat}\text{Fe}/^{57}\text{Fe}$  layer structures (22100 laser pulses altogether) the

Sample name	L1: $^{nat}\text{Fe}$		L2: $^{57}\text{Fe}$		L3: $^{nat}\text{Fe}$		$t_{RBS}$ [nm]	$d_{57\text{Fe}}$ [nm]
	# pls.	$t_{nom}$ [nm]	# pls.	$t_{nom}$ [nm]	# pls.	$t_{nom}$ [nm]		
SI-S	1500	5	4400	15	16200	55	83(4)	13(3)
SI-M	8850	30	4400	15	8850	30	—	—
SI-I	17700	60	4400	15	—	—	65(4)	56(3)
MGO-S	1500	5	4400	15	16200	55	58(4)	9(3)
MGO-M	8850	30	4400	15	8850	30	49(4)	24(3)
MGO-I	17700	60	4400	15	—	—	—	—

Table 6.1: Layer structures of all PLD films. # pls. is the number of laser pulses for the present layer,  $t_{nom}$  is the nominal layer thickness according to the calibration sample,  $t_{RBS}$  is the overall film thickness as measured by RBS and  $d_{57\text{Fe}}$  is the depth of the  $^{57}\text{Fe}$  marker layer according to RBS.

laser-target-sample geometry was not changed any more. Thus all these films were supposed to have the same nominal thickness (see Table 6.1).

Like with the experiments described in section 4.2 three different layer structures were deposited. The 15 nm marker layer was placed at the surface, in the middle and the interface with the substrate, and the corresponding samples are SI-S, SI-M and SI-I for the films on Si(100) and MGO-S, MGO-M and MGO-I for the ones on MgO(100). All substrates were  $10 \times 10 \text{ mm}^2$  in size.

Before the films were ion irradiated, a characterization of the layer structure was performed by RBS with a procedure very similar to the one presented in section 4.2.1 (see Table 6.1). The thickness of SI-S, which was deposited first, is slightly larger than nominal, but the values of  $t_{RBS}$  decrease for the specimens deposited later on. MGO-I is considered to be thinner than 49(4) nm, but was not measured by RBS. The reduction of the film thicknesses with increasing pulse number on the target is caused by the ageing effect of the target [Stu00].

**Ion irradiation and analysis.** After the deposition, all films were characterized by MOMS ( $\alpha = 45^\circ$ ,  $\Delta\varphi = 20^\circ$ ). The  $\varphi = 0^\circ$  direction was arbitrarily chosen parallel to one substrate edge and marked on the samples. A careful study of the crystal structure was performed by XRD in various geometries, and before irradiation the hysteresis curves of all films except SI-S and MGO-S were analyzed by MOKE with an angular resolution of  $\Delta\varphi = 10^\circ$ .

The irradiations were carried out with parameters similar to the ones presented in the preceding sections: the sample was at room-temperature and the fluence was  $1 \times 10^{16} \text{ Xe}^+/\text{cm}^2$ . The energy was 200 keV for the Fe/Si(100) layers but was reduced to 150 keV ( $R_p = 27 \text{ nm}$ ) for Fe/MgO(100) because the films were thinner. SI-S and MGO-S were bombarded without application of an external magnetic field, similar to sample 2-M in section 4.2.3. During the irradiation of the other samples, an external field of 104 Oe was present; for SI-M and MGO-M it was oriented in the  $\varphi = 0^\circ$  direction, for SI-I in  $145^\circ$  and for MGO-I in  $45^\circ$  direction. An explanation for the choice of these angles will be given below.

After the irradiation MOMS, XRD and MOKE were carried out. An additional  $\varphi$ -scan was performed on all specimens to investigate the in-plane texture of the films.

## 6.2 Fe/Si(100)

### 6.2.1 Magnetic anisotropy

**MOMS.** In chapter 4.2 it was discussed that it is important to apply MOMS as the first characterization technique after deposition as well as after irradiation. For all corresponding CEMS spectra except SI-I<sub>asdep</sub> two sextets with hyperfine fields of  $B_{HF} \approx 33$  T and  $B_{HF} \approx 30$  T and one doublet with a quadrupole splitting of  $\approx 1$  mm/s or 0.6 mm/s were sufficient for a good fit. Taking into account that a reduction of the hyperfine field of  $\alpha$ -iron by  $\Delta B_{HF} = 3.6$  T is correlated to the loss of one nearest or next nearest neighbor, this result indicates a smaller number of defects in the analyzed layer in comparison with the electron-beam evaporated films in section 4.2 (see also Table B.1). For the as-deposited films, the area fraction of the  $\alpha$ -iron sextet is  $> 90\%$ , only for SI-I it is  $80\%$  because the  $^{57}\text{Fe}$  is not sandwiched between two  $^{nat}\text{Fe}$  layers but located at the interface with the silicon substrate. This is the reason for the large area fraction  $F_2$  of sextet 2. The fit parameters of the CEMS spectra of samples SI-S, SI-M and SI-I are summarized in Table B.2.

After the ion implantation, the samples SI-S and SI-M showed similar changes of the hyperfine parameters. In both specimens the area fraction of the unperturbed  $\alpha$ -iron decreased from  $> 90\%$  to  $< 80\%$  in favor of the defect site ( $B_{HF} \approx 30$  T) and the non-magnetic doublet. For SI-I<sub>irr</sub> the area fraction  $F_1$  of  $\alpha$ -iron decreased and a strong doublet with  $F_D = 25\%$  was observed that can be assigned to iron silicide ( $\Delta = 0.61(1)$  mm/s,  $\delta = 0.26(1)$  mm/s). As a result of the small film thickness ( $\approx 65$  nm), the xenon ions penetrated the Fe/Si interface, forming iron silicide by ion-beam mixing.

The MOMS fitting parameters are summarized in Table 6.2 for all the samples before and after the ion bombardment and illustrated in Figures 6.1 and 6.2 for specimens SI-M and SI-I. All samples have a preferred hyperfine field direction which depends on the geometry of the layer structure. After deposition SI-M showed a poor spin-alignment, as indicated by the small value  $c_a = 0.55$ . Considering that in this sample the marker layer was in the middle of the film, a similar behavior had previously been observed in sample 1-M (see section 4.2.3), which had exactly the same layer structure. For specimens SI-S<sub>asdep</sub> and SI-I<sub>asdep</sub>, having the  $^{57}\text{Fe}$  layer at the top or at the interface with the substrate, a spin direction is preferred, which is indicated by the large value  $c_a \approx 0.8$ .

During implantation no external field was applied to sample SI-S and no MOKE analysis was carried out before the ion irradiation. According to the results of chapter 4.2.3, the spin distribution is expected to keep the parameters  $\psi_a$  and  $c_a$  after ion irradiation, but the experiment results in a difference in  $\psi_a$  of  $20^\circ$ .

In contrast to this irradiation geometry, an external magnetic field was applied during implantation to SI-M and SI-I. For SI-I the direction of  $H_{impl}$  was chosen parallel to the preferred spin direction before irradiation (see MOMS results, Table 6.2). The results of chapter 4.1 suggest good alignment of the easy axis along this field direction after ion irradiation. Thus, SI-M<sub>irr</sub> is supposed to show  $\psi_a = 0^\circ$  and SI-I<sub>irr</sub>  $\psi_a = 145^\circ$ . The results suggest a quite strong spin alignment ( $c_a > 0.8$ ), but the alignment directions are in contradiction to the expected values.

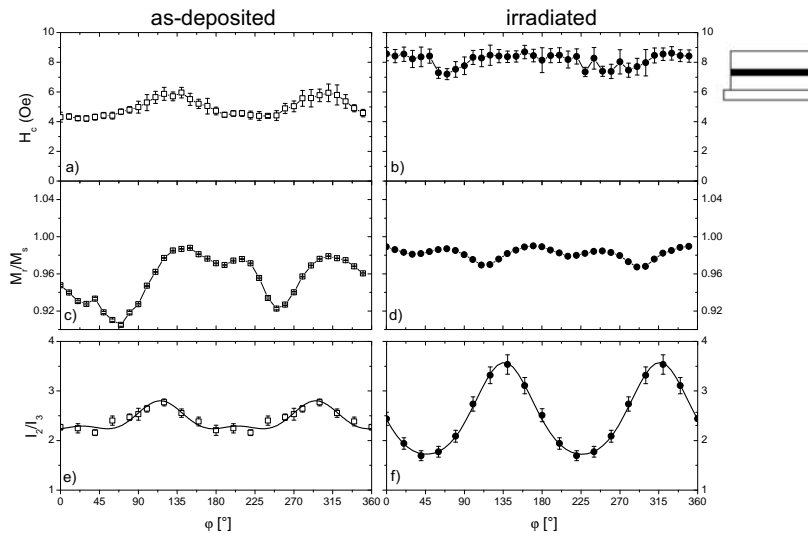


Figure 6.1: Sample SI-M: results of MOKE (a,b,c,d) and MOMS (e,f). During irradiation an external magnetic field of 104 Oe was applied in  $0^\circ$  direction.

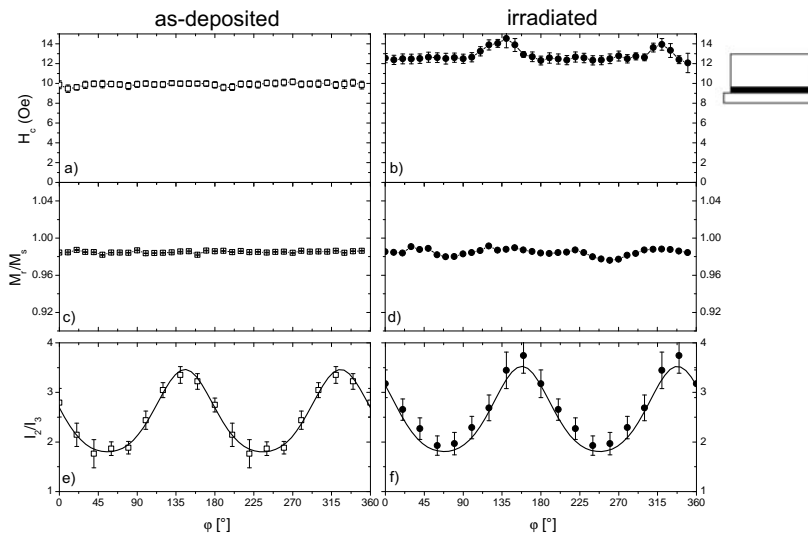


Figure 6.2: Sample SI-I: results of MOKE (a,b,c,d) and MOMS (e,f). During the irradiation an external magnetic field of 104 Oe was applied in  $145^\circ$  direction.



Sample	MOMS fit				Exp.
	$\psi_a$ [°]	$c_a$ [%]	$c_b$ [%]	$c_{op}$ [%]	$c_{op}$ [%]
SI-S <sub>asdep</sub>	101(3)	79(1)	13(1)	8(1)	3(2)
SI-S <sub>irr</sub>	120(6)	50(2)	47(2)	3(2)	0(3)
SI-M <sub>asdep</sub>	115(4)	55(1)	36(1)	9(1)	0(5)
SI-M <sub>irr</sub>	136(3)	84(1)	15(1)	1(1)	0(3)
SI-I <sub>asdep</sub>	145(3)	80(2)	17(2)	3(2)	3(5)
SI-I <sub>irr</sub>	158(4)	82(2)	18(2)	0(0)	0(3)

Table 6.2: MOMS fit parameters SI-S, M and I.  $\psi_a$  is the angle between the strongest in-plane hyperfine field component ( $c_a$ ) and the  $0^\circ$  direction.  $c_b$  is perpendicular to  $c_a$  and  $c_{op}$  is the out-of-plane component of the hyperfine field. Error 0 indicates a fixed  $c_{op}$  for the final fit.

In both samples the angle  $\psi_a$  of the as-deposited state was neither preserved nor does the orientation match the direction of  $H_{impl}$ .

**MOKE.** The results of the MOKE measurements must also be seen with respect to the findings obtained on the films deposited by electron-beam evaporation. The most obvious difference are the small values of the coercive force, which are  $< 10$  Oe in all the PLD specimens before irradiation, while they were  $> 40$  Oe for most electron-beam evaporated films. In agreement with the samples of chapter 4, the MOKE analysis of SI-M<sub>asdep</sub> and SI-I<sub>asdep</sub> indicates no or a small magnetic anisotropy, as presented in Figs. 6.1 and 6.2 a)+c). The weak variation of  $M_r/M_s$  visible in Figs. 6.1 c) and d) is a consequence of the large expansion of the scale. However, this small anisotropy in  $140^\circ$  direction seems to be significant, since it is also observed as an increase in the value of  $H_c$ .

The irradiation affected  $H_c$  in a similar way for both specimens: the average value increased by about 3 Oe and shows a weak anisotropic component in addition to the strong isotropic part. SI-S<sub>irr</sub> does not show this anisotropic fraction in  $H_c$  and the relative remanence has only a small  $\varphi$ -dependence. According to the results for specimen 2-M in section 4.2.3, an alignment of the easy axis with respect to the preferred spin-direction as observed by MOMS is expected, because the specimen was not magnetized before and during the irradiation. The results do not agree with this expectation. SI-M<sub>irr</sub> and SI-I<sub>irr</sub> are not completely isotropic but their anisotropy is very small, as illustrated in Figures 6.1 and 6.2 b)+d).

On account of the negligible size of the anisotropy, a fit of the normalized anisotropy constants and the corresponding angles  $\varphi_0$  of the easy axes was not possible. Qualitatively, the easy axes are supposed to be at  $140(10)^\circ$  for SI-S<sub>irr</sub>, at  $170(10)^\circ$  or  $260(10)^\circ$  for SI-M<sub>irr</sub> and  $130(10)^\circ$  for SI-I<sub>irr</sub>. None of these angles matches the results obtained by MOMS.

## 6.2.2 Crystallographic structure

As the texture of the PLD films is usually quite strong, the crystallographic analysis via XRD is promising. Particularly in the  $\theta - 2\theta$  scans the effect of the out-of-plane texture should be visible. The specimens were rotated during the measurements to obtain the average information

Sample	$\theta - 2\theta$		Rocking curve	
	$2\theta$ [°]	FWHM [°]	$\theta$ [°]	FWHM [°]
SI-S <sub>asdep</sub>	44.510(7)	0.614(20)	21.35(8)	11.49(24)
SI-S <sub>irr</sub>	44.527(5)	0.471(17)	21.13(2)	9.38(5)
SI-M <sub>asdep</sub>	44.511(14)	0.569(50)	21.75(4)	7.49(8)
SI-M <sub>irr</sub>	44.592(2)	0.396(5)	21.84(1)	6.30(3)
SI-I <sub>asdep</sub>	44.426(27)	0.690(112)	21.23(20)	13.84(74)
SI-I <sub>irr</sub>	44.556(8)	0.400(25)	21.20(5)	10.08(14)

Table 6.3: Results of the XRD analysis of the PLD films on Si(100).

about the film. Like for the specimens deposited by electron-beam evaporation on Si(100), only the Fe(110) peak is visible at  $44.7^\circ$  (see Fig. 6.3). The exact position and width of the peak were determined using symmetric Pearson VII line-shapes. The correlated parameters are summarized in Table 6.3. In contrast to the results of section 4.2.5, the lattice shows an out-of-plane expansion after deposition which is released partially as an effect of the ion irradiation. Besides the out-of-plane texture the crystalline quality is an important parameter. To measure this property the change of the rocking curve of the Fe(110) peak before and after irradiation was analyzed. The sample was rotated around its normal during the measurement. The full width at half maximum of the rocking peak of all samples was  $\approx 10^\circ$  and decreased due to irradiation (see Table 6.3). This change is illustrated for sample SI-M in Figs. 6.4 a)+b).

The high texture of the films enabled us to obtain information on the in-plane orientation of the lattice. For this purpose a  $\varphi$ -scan was performed on the films. For a  $\varphi$ -scan measurement, the X-ray reflections at a fixed  $2\theta$  angle  $\psi$  were measured from a plane ( $hkl$ ) inclined at an angle to the surface normal. In this way the in-plane texture of the film could be determined.

Figure 6.4 c) is an example of a  $\varphi$ -scan performed on sample SI-M<sub>irr</sub>. The graphs result from the Si(422) line, having its maximum at  $180^\circ$ , and the Fe(211) line. As the silicon wafer is (100) oriented it can be concluded that the  $0^\circ$  direction of the sample is the  $\langle 110 \rangle$  orientation. Also the peaks at  $0^\circ$ ,  $90^\circ$  and  $270^\circ$  should be visible, but their angle  $\theta$  was slightly different, probably due to lattice imperfections or a slight misalignment of the goniometer. Fe(211) has a high intensity, but shows no maximum, which leads to the conclusion that the film has a fiber texture as can be found in films with columnar growth [Cul78]. The XRD results for all specimens are summarized in Table 6.3.

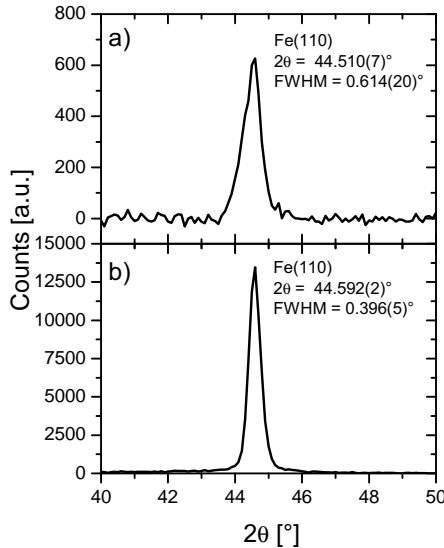


Figure 6.3: Fe(110) peaks of sample a) SI-M<sub>asdep</sub> and b) SI-M<sub>irr</sub> after irradiation with  $10^{16}$  Xe<sup>+</sup>/cm<sup>2</sup>.

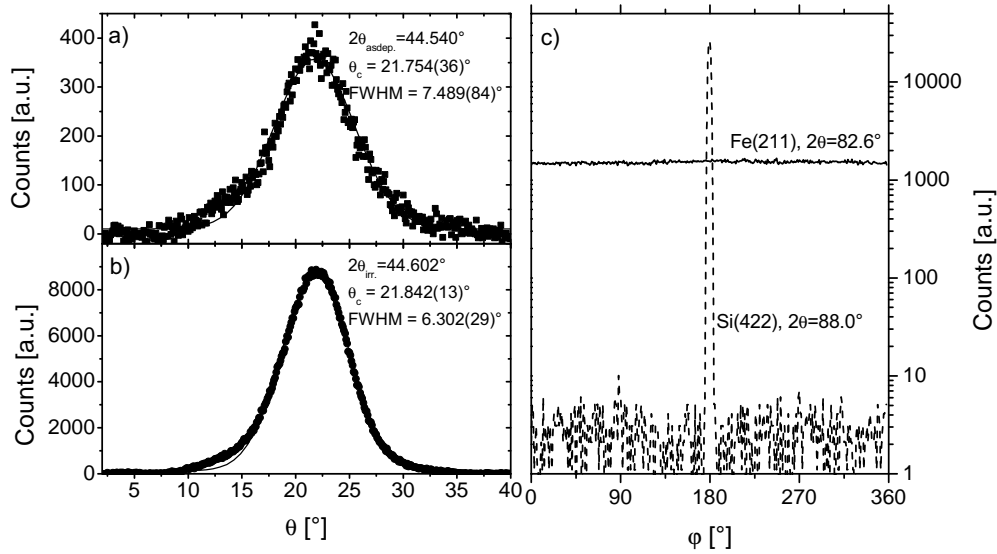


Figure 6.4: Rocking curves of sample a) SI-M<sub>asdep</sub> and b) SI-M<sub>irr</sub>. c)  $\varphi$ -scan of sample SI-M<sub>irr</sub>.

## 6.3 Fe/MgO(100)

### 6.3.1 Magnetic anisotropy

**MOMS.** The CEMS spectra of MGO-S, MGO-M and MGO-I were fitted using mainly the sextet of  $\alpha$ -iron and the defect site with  $B_{HF} \approx 30$  T. Like in the case of the silicon substrate, the area fraction  $F_2$  of the doublet in the as-deposited films is very small. It is surprising that the area fraction  $F_2$  is the largest for MGO-M<sub>asdep</sub> (8%) in comparison with the other specimens (4%), because the marker layer is located in the middle of the film and thus no interface effects should occur. The irradiation caused an increase in the area fraction  $F_2$  from 4% (8%) to 13% (23%), resulting from the defect production in the film. Also the hyperfine field increases by 0.1 - 0.2 T for the  $\alpha$ -iron site and by 1 T for the defect site. All fit parameters are summarized in Table B.2.

MOMS resulted only for specimen MGO-I<sub>asdep</sub> in a large value  $c_a = 0.72$  at  $\psi_a = 136(3)^\circ$ . Here the  $^{57}\text{Fe}$  marker-layer was deposited directly onto the substrate. The origin of this spin-distribution preference is probably the crystal orientation of the substrate. Iron usually grows with the  $\langle 100 \rangle$  orientation in the  $\langle 110 \rangle$  direction of the MgO substrate [Sub99] and because the  $\langle 100 \rangle$  direction of MgO is parallel to  $0^\circ$ , the easy axis of iron (Fe(100)) is oriented in  $45^\circ$  or  $135^\circ$  direction (see Fig. 6.6). For the samples containing the marker layer in the middle and on top of the film, the anisotropy of the hyperfine field distribution is nearly isotropic before ion irradiation

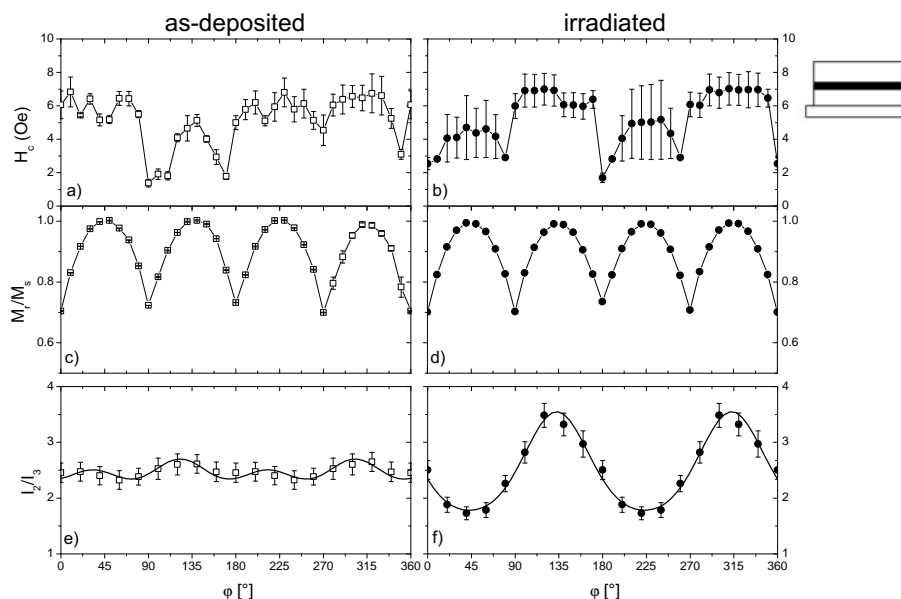


Figure 6.5: Sample MGO-M: results of MOKE (a,b,c,d) and MOMS (e,f). During irradiation an external magnetic field of 104 Oe was applied in  $0^\circ$  direction.

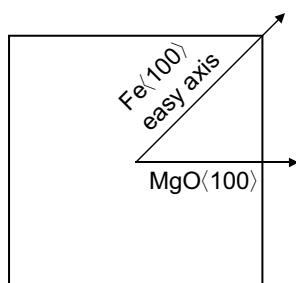


Figure 6.6: Crystallographic orientation of the iron film on MgO.

(MGO- $S_{asdep}$ :  $c_a = 0.53$ ,  $\psi_a = 144^\circ$ ; MGO- $M_{asdep}$ :  $c_a = 0.51$ ,  $\psi_a = 122^\circ$ ).

The irradiation affects the behavior of the spins distinctly. Sample MGO-S was irradiated without any external magnetic field and in non-magnetized condition. For MGO-M the external field of 104 Oe was applied in the  $0^\circ$  direction of the sample, which is the hard axis of magnetization. MGO-I was irradiated with the external field in the easy axis direction ( $45^\circ$ ).

MGO- $S_{irr}$  still had a small preferred component  $c_a = 0.58$ , but the direction of the spin alignment had changed. It had been  $144(6)^\circ$  before the irradiation and changed to  $\psi_a = 45(5)^\circ$  direction. The out-of-plane component  $c_{op}$  was also reduced by the ion bombardment. MGO- $M_{irr}$  with the external field oriented in  $0^\circ$  direction during irradiation ended in  $\psi_a = 133(3)^\circ$ , changing its original orientation by about  $10^\circ$ . The degree of spin orientation

( $c_a = 0.83$ ) is quite high. Finally, sample MGO- $I_{irr}$  changed its hyperfine field orientation by  $90^\circ$  from  $136(3)^\circ$  to  $45(3)^\circ$ . It showed a nearly perfect alignment of all spins ( $c_a = 0.95$ ).

In conclusion the ion irradiation aligned the hyperfine field preferentially in  $45^\circ$  and in  $135^\circ$  direction. The parameter  $c_a$  increased for all irradiated specimens and in MGO- $I_{irr}$  a nearly perfect alignment of the spins was achieved. The MOMS results are summarized in Table 6.4 and illustrated for MGO-M and MGO-I in Figures 6.5 and 6.7.

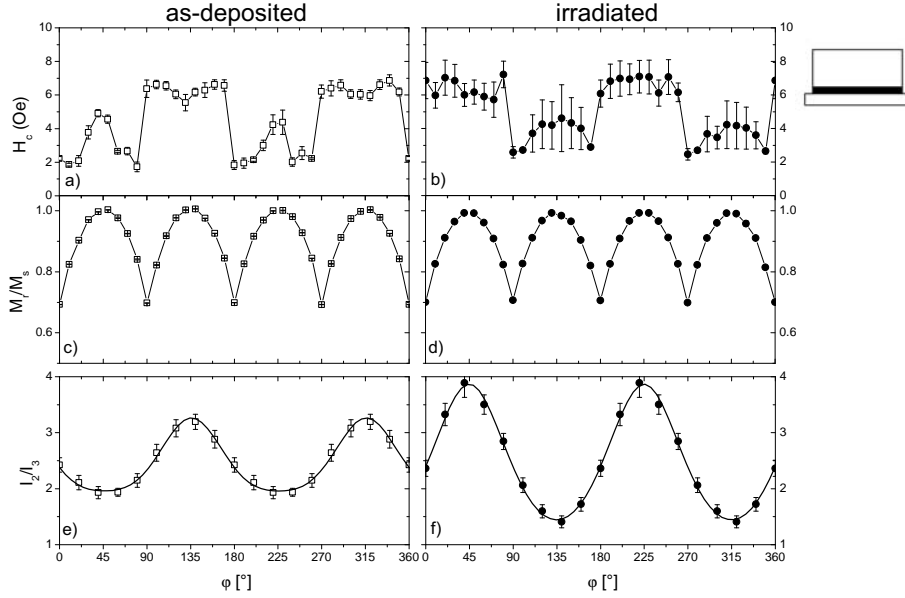


Figure 6.7: Sample MGO-I: results of MOKE (a,b,c,d) and MOMS (e,f). During irradiation an external magnetic field of 104 Oe was applied in  $0^\circ$  direction.

Sample	$\psi_a$ [°]	MOMS fit			Exp.
		$c_a$ [%]	$c_b$ [%]	$c_{op}$ [%]	$c_{op}$ [%]
MGO-S <sub>asdep</sub>	144(6)	53(2)	40(2)	7(2)	1(5)
MGO-S <sub>irr</sub>	45(5)	58(2)	40(2)	2(2)	1(5)
MGO-M <sub>asdep</sub>	122(5)	51(1)	46(1)	5(1)	0(2)
MGO-M <sub>irr</sub>	133(3)	83(2)	15(2)	0(2)	0(2)
MGO-I <sub>asdep</sub>	136(3)	72(1)	24(1)	4(1)	3(6)
MGO-I <sub>irr</sub>	45(3)	95(1)	4(1)	1(1)	0(4)

Table 6.4: MOMS fit parameters of the PLD films.  $\psi_a$  is the angle between the strongest in-plane hyperfine field component ( $c_a$ ) and the  $0^\circ$  direction.  $c_b$  is perpendicular to  $c_a$  and  $c_{op}$  is the out of plane component of the hyperfine field.

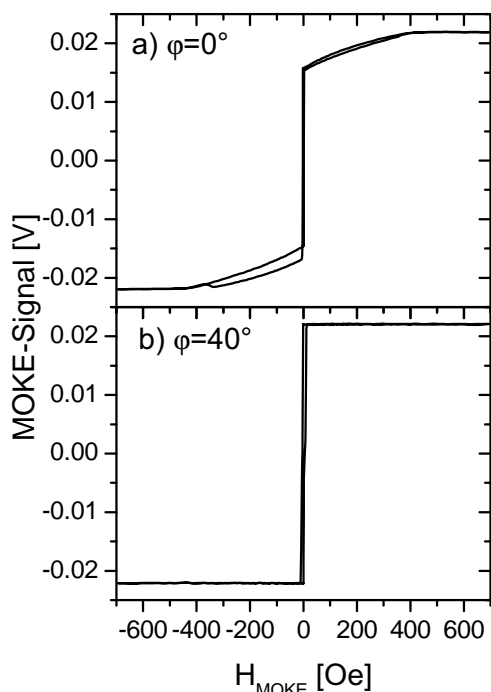


Figure 6.8: MOKE hysteresis curves a) for the hard axis ( $\varphi = 0^\circ$ ) and b) near the easy axis ( $\varphi = 40^\circ$ ) of the film. In the hard axis direction the curve is distorted.

entation as measured by MOMS. Generally, the coercive field was  $< 8$  Oe which is comparable with the values obtained for the films deposited by PLD on silicon substrate.

The ion implantation in different geometries of the magnetic field relative to the  $0^\circ$  axis of the sample has no visible effect on the relative remanence of all films. Even the irradiation with  $H_{impl}$  in  $0^\circ$  direction, which is the hard axis of magnetization, did not affect the fourfold symmetry of the remanence, as described for the as-deposited samples. The  $\varphi$ -dependence of the coercive field  $H_c$  is twofold and contains some additional information correlated to the MOMS results.

As described in the preceding paragraph, the coercive field is large over a broad angular range of one easy axis and in the second easy axis it shows just a small maximum. For MGO- $S_{irr}$  the results of the MOMS measurement suggest an angle  $\psi_a$  of  $45^\circ$  which is parallel to an easy axis direction. In the same direction  $H_c$  is very large over a wide angular range and in  $135^\circ$  direction  $H_c$  shows a maximum value only for a small angular range. The same phenomenon can be observed for MGO- $M_{irr}$  and MGO- $I_{irr}$  as illustrated in Figures 6.5 and 6.7.

**MOKE.** All hysteresis curves of the Fe/MgO samples had a completely different shape compared to the ones measured in the preceding paragraphs (see Figure 6.8). Similar shapes of the loops near the hard axis of epitaxial Fe(100) films were observed by various authors [Yan00, Sub99, Ber01a]. The curves have a very low coercive field of only 2 - 10 Oe and in the hard axis direction an external magnetic field of  $\approx 400$  Oe is necessary to saturate the film. Consequently, specimen MGO-M was not completely saturated during the irradiation.

When analyzing the MOKE hysteresis loops for the parameters  $H_c$  and  $M_r/M_s$ , the most obvious property of the samples MGO- $M_{asdep}$  and MGO- $I_{asdep}$  is their perfect fourfold anisotropy having their easy axes in  $45^\circ$  and  $135^\circ$  directions. This result matches the expectations of epitaxial growth of the iron on MgO [Sub99] as the Fe $\langle 100 \rangle$  direction is oriented parallel to MgO $\langle 110 \rangle$ . An anisotropy is also visible in the  $H_c$  data, but they show only a twofold symmetry with a broad angular range of high coercivity around one easy axis and a small peak around the other easy axis. In all the samples the broad high-coercivity direction coincided with the preferred spin ori-

### 6.3.2 Crystallographic structure

First of all a scan in  $\theta - 2\theta$  geometry with rotating specimens was performed. Besides the MgO(200) substrate reflex at  $42.9^\circ$ , the very pronounced line of Fe(200) at  $65.0^\circ$  was observed. In all as-deposited films this peak shows two components: one main component at smaller angles and a much weaker component at angles near the bulk value. Because a double Pearson VII function was necessary to fit the peaks, the *WinFit!*-program [Kru97] was used to determine the  $2\theta$  angles. All errors were estimated to be  $0.02^\circ$  for the  $2\theta$  angle and  $0.05^\circ$  for the FWHM (see Table 6.5).

After irradiation the Fe(200) peak was found at a slightly larger angle than after deposition indicating still an out-of-plane texture of the iron films in (100) direction. Comparing the present line intensities with the intensities of the films deposited on a silicon substrate and considering that in a random powder sample the (200) peak should show only 20% of the intensity of the (110) line, the films seem to have a very strong out-of-plane texture [PDF97].

In this context the rocking curves of the films on the MgO substrate are very interesting. The FWHM is  $\approx 1^\circ$  for all as-deposited samples. The quality of the film obviously is excellent, as in many publications epitaxially grown films show even higher FWHM values [Kre98]. After the irradiation the FWHM even decreased to  $\approx 0.6^\circ$ . Therefore the crystalline order improved by irradiation as already indicated by the FWHM decrease in the  $\theta - 2\theta$  scan (see Table 6.5).

A  $\varphi$ -scan was performed after the irradiation to examine the in-plane texture of the crystal structure. In contrast to the findings on SI-S, SI-M and SI-I, very sharp peaks were found for MgO(311) and Fe(211). The  $\langle 100 \rangle$  directions of the iron are therefore oriented in the  $\langle 110 \rangle$  directions of the substrate, showing a strong in-plane texture after irradiation with  $\text{Xe}^+$ . This results was already suggested by the observations of the magnetic properties of the films.

The  $\varphi$ -scans were only performed on the irradiated specimens. The decrease of the FWHM of the rocking curves and the coinciding alignment of the magnetic anisotropy constant suggest that the texture was already present in the as-deposited samples.

Sample	$\theta - 2\theta$		Rocking curve		$\varphi$ -scan
	$2\theta$ [°]	FWHM [°]	$\theta$ [°]	FWHM [°]	$\varphi_{max}$ [°]
MGO-S <sub>asdep</sub>	64.511(20)	0.750(50)	32.222(2)	0.977(4)	—
MGO-S <sub>irr</sub>	64.649(20)	0.360(50)	32.389(4)	0.602(8)	45/135
MGO-M <sub>asdep</sub>	64.273(20)	0.632(50)	32.144(3)	1.031(7)	—
MGO-M <sub>irr</sub>	64.753(20)	0.458(50)	32.424(3)	0.611(7)	45/135
MGO-I <sub>asdep</sub>	64.270(20)	0.534(50)	32.130(2)	0.792(5)	—
MGO-I <sub>irr</sub>	64.937(20)	0.476(50)	32.443(1)	0.472(2)	45/135

Table 6.5: Results of the XRD analysis of PLD films on MgO(100) substrates.

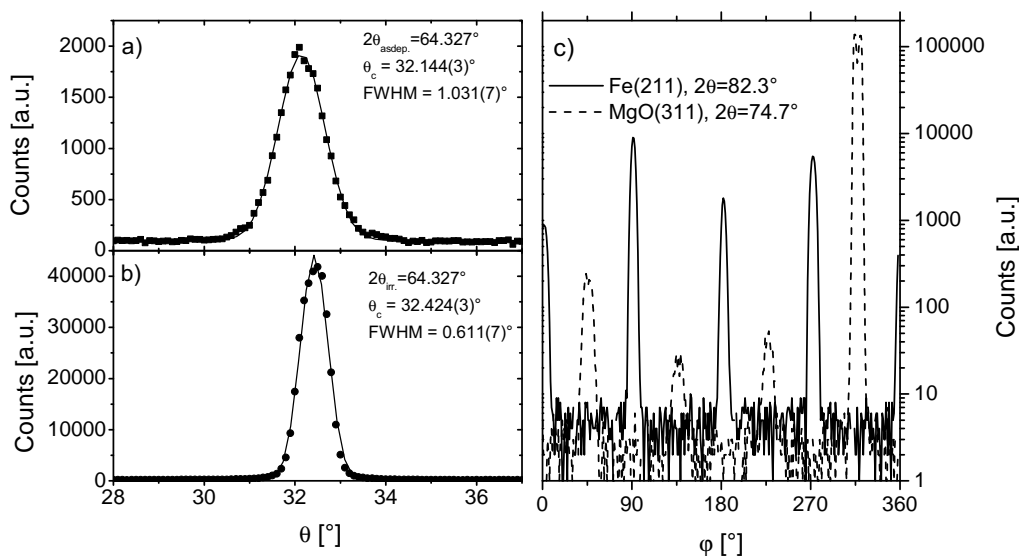


Figure 6.9: Rocking curve of a) sample MGO-M<sub>asdep</sub> and b) MGO-M<sub>irr</sub> (b)). c) shows the  $\varphi$ -scan of specimen MGO-M<sub>irr</sub>.

## 6.4 Discussion

### 6.4.1 Structure of the PLD films

Metal films prepared by pulsed laser deposition are known to show some special structural properties in comparison with electron-beam evaporated films [Kre97]:

1. The films show a lattice expansion in growth direction, combined with a compressive stress in the film plane.
2. In miscible systems PLD films have a broad interface with the substrate, as the ablated ions are implanted into the substrate surface at a higher energy (100 eV). In immiscible systems the interfaces are sharp.
3. The films often have a high degree of crystallinity (usually columnar growth). Moreover they show a texture due to the high deposition energies and consequently the high surface mobility of the ions.

Some of these properties were found in the films studied here. The lattice expansion perpendicular to the film surface is clearly seen in the low  $2\theta$ -angles of the Fe(110) (Fe/Si) and Fe(200) peaks (Fe/MgO), resulting from the  $\theta - 2\theta$  measurements: while the values published for bulk bcc-iron are  $2\theta_{110} = 44.673^\circ$  and  $2\theta_{200} = 65.021^\circ$  [PDF97] the measured angles as presented in Tables 6.3 and 6.5 are on average  $0.2^\circ$  (SI-S<sub>asdep</sub>, SI-M<sub>asdep</sub> and SI-I<sub>asdep</sub>) and  $0.6^\circ$  (MGO-S<sub>asdep</sub>, MGO-M<sub>asdep</sub> and MGO-I<sub>asdep</sub>) smaller. This is equivalent to an expansion of the lattice by 0.4%



and 0.9%. These values change to 0.2% (Fe/Si) and 0.4% (Fe/MgO) during ion irradiation. The interface properties of the films were measured by RBS and CEMS. In the depth profiles of the RBS measurements the interface signals of the PLD films were not broader ( $w_{Fe/Si} = 11$  nm) than the ones measured for the electron-beam evaporated films (see section 4.1.1). However, as the implantation depth of 100 eV ions is 1 nm, RBS is not sensitive enough to detect the penetration of the Fe in the substrate. A comparison of the parameters used for the fitting of the CEMS spectra of SI-I<sub>asdep</sub> with the ones used for the other samples possibly indicates a small amount of silicide formation. While for SI-M<sub>asdep</sub> and SI-S<sub>asdep</sub> the area fraction of the doublet site  $F_D$  is less than 1%, it is about 3% for SI-I<sub>asdep</sub> with a quadrupole splitting of  $\Delta = 0.99(12)$  mm/s. Two sextets with  $B_{HF} \approx 33$  T and  $B_{HF} \approx 30$  T were needed to obtain a perfect fit of the spectra. Consequently, no large number of iron atoms are surrounded by silicon, which would cause a further reduction of the hyperfine field. In conclusion, the CEMS-measurements suggest neither intense iron silicide phase formation nor strong interface mixing. The MgO-Fe system is immiscible and thus the interface is sharp. However, it is interesting that the area fractions  $F_1$  and  $F_2$  are different for the as-deposited specimens SI-I and MGO-I. This is a hint of different interface properties of the films on Si and on MgO.

As expected, the crystal quality is very good, especially in the case of the films deposited on MgO. Not only the high texture, but also the FWHM of the rocking curve of less than  $1^\circ$  after deposition is an indication of a nearly epitaxial film. As its width decreases for the irradiated films and as a very high in-plane texture is found in the  $\varphi$ -scan (the FWHM is  $< 4^\circ$  for all peaks in MGO-S<sub>irr</sub>, MGO-M<sub>irr</sub> and MGO-I<sub>irr</sub>), the quality of the film is even improved by the irradiation. The decrease in the  $\theta - 2\theta$  line widths is also in agreement with this observation.

While the films on MgO have a very strong in-plane texture, the ones on silicon show typical properties of polycrystalline films with an out-of-plane fiber texture in (110) direction. The rocking curves (FWHM about  $10^\circ$  before and  $8 - 9^\circ$  after irradiation) and the isotropic intensity distributions of the  $\varphi$ -scan prove this interpretation. The FWHM in the  $\theta - 2\theta$  scan decreases during the implantation, indicating a possible ion-beam induced grain growth or relaxation of microstrain.

### 6.4.2 Fe/Si

A comparison of the structural and magnetic properties of the PLD films on silicon substrates with the ones used in the preceding chapters leads to several differences. Both deposition methods prepare polycrystalline films with a Fe(110) out-of-plane texture. However, the texture is strong for the PLD films, while it is very weak for the ones prepared by electron-beam deposition. The lattice parameter normal to the film plane indicates an expansion of the PLD films and a reduced value for the electron-beam evaporated ones, compared with the bulk value (see Tables 4.8 and 6.3). The ion irradiation induces a decrease in the perpendicular lattice parameter of the PLD films and an increase for the others. The rise is supposed to be in correlation with the reduction of the internal tensile deposition stress. Similarly, the observed decrease in the PLD lattice parameter might be caused by the reduction of the compressive deposition stress of the films.

According to section 5.2,  $H_c$  is very sensitive to these structural differences. In fact, the as-

deposited PLD films have nearly isotropic coercivity of  $\lesssim 10$  Oe while the electron-beam evaporated samples showed  $20 \text{ Oe} < H_c < 60 \text{ Oe}$ . Due to ion irradiation, this value decreased to  $\lesssim 10$  Oe and this decrease was interpreted to happen due to the reduction of the in-plane tensile stress (see section 5.2). Consequently, the low coercive field of the as-deposited PLD films might be a result of low compressive deposition stress, which is in qualitative agreement with the predictions of Krebs [Kre97]. The rise of  $H_c$  to  $\lesssim 13$  Oe during the ion irradiation might be correlated to radiation damages. A similar but stronger effect was observed by means of ion irradiation of electron-beam evaporated films with  $5 \times 10^{16} \text{ Xe/cm}^2$ .

The influence of ion-beam irradiation on magnetic anisotropy and its alignment is also completely different for the two deposition methods. Before irradiation, PLD as well as electron-beam evaporated films are nearly isotropic in  $M_r/M_s$ . According to the results of chapters 4 and 5 an irradiation fluence of  $1 \times 10^{16} \text{ Xe}^+/\text{cm}^2$  at room-temperature is sufficient for electron-beam evaporated films to become twofold magnetically anisotropic. The alignment of the anisotropy depends on the magnetization direction of the film during the irradiation, or, if the sample was not externally magnetized, the deposition anisotropy as measured by MOMS. The analysis of the in-plane anisotropy in the PLD films does not show consistent results. MOMS shows a strong alignment of the spins of SI-S<sub>asdep</sub> ( $\psi_a = 101(3)^\circ$ ,  $c_a = 0.79(1)$ ). The irradiation of this film without externally magnetizing it before or during the ion implantation is expected to conserve the spin alignment, and a MOKE analysis after irradiation should show uniaxial anisotropy oriented in the direction  $\varphi_0 = 100^\circ$  (see results on sample 2-M, section 4.2.3). The present MOMS and MOKE measurements result in a very weak anisotropic spin distribution and hysteresis behavior. Nearly all error bars of the MOMS ratios  $I_2/I_3$  overlap. The observations concerning the magnetic properties of specimens which were magnetized during the ion irradiation (SI-M and SI-I) are not in line with the former results either: SI-M<sub>asdep</sub> shows a small magnetic anisotropy ( $M_r/M_s$ ) which becomes nearly zero after ion irradiation. A preferred spin direction ( $\psi_a = 136(3)^\circ$ ,  $c_a = 0.84(1)$ ) is obtained from the MOMS fit. When orienting the external magnetic field in  $145^\circ$  direction, like it was done for SI-I during the ion bombardment, again the anisotropy measured by MOKE is nearly zero and MOMS shows a preferred hyperfine field orientation in  $\psi_a = 158(4)^\circ$  direction.

To sum up, the ion irradiation of PLD films induces no significant magnetic anisotropy, as measured by MOKE. The application of an external magnetic field during the implantation has no effect on this macroscopic behavior, but it induces a high spin alignment. However, the directions  $\psi_a$ , resulting from MOMS, are not correlated to the directions of  $H_{impl}$ . A closer look to the CEMS hyperfine parameters of the samples 2-M, 2-B and 2-S (see section 4.2.3 and 4.2.4) and SI-S and SI-M might explain the large difference of the irradiation effect on PLD and electron-beam deposited films. While for 2-M, 2-B and 2-S after the ion bombardment three sextets with hyperfine fields of 33 T ( $F_1 \approx 75\%$ ), 27 T ( $F_2 \approx 9\%$ ) and 20 T ( $F_3 \approx 6\%$ ) were used to achieve a good fit (Table B.1), for SI-S and SI-M only two sextets with  $B_{HF} = 33$  T ( $F_1 \approx 75\%$ ) and  $B_{HF} = 30$  T ( $F_2 \approx 20\%$ ) were sufficient to describe the spectra (Table B.2). Consequently, the electron-beam evaporated films have a large number of  $^{57}\text{Fe}$  atoms surrounded by more than 2 vacancies, while in the PLD films on average only one of the nearest and next nearest neighbors is not iron. This observation is in agreement with the microscopic model of Antonov [Ant77] presented in section 5.4.2, in which the accumulation of defects in a preferential direction is supposed to be responsible for the induction of magnetic anisotropy. Obviously the

fraction of  $^{57}\text{Fe}$  atoms near such precipitates is much smaller for the PLD films compared to electron-beam evaporated films and thus the present results are in agreement with the model presented in section 5.4.2, although they are different for the two deposition methods.

### 6.4.3 Fe/MgO

The films deposited on MgO(100) substrates differ from all other samples presented up to now. As described in section 6.3, MGO-S, MGO-M and MGO-I are out-of-plane as well as in-plane textured. That is why they are supposed to show magnetocrystalline anisotropy (see section 2.1.2). The easy axes of a bcc iron single crystal are in the  $\langle 100 \rangle$  directions and since the present films show a Fe(100) out-of-plane texture, a fourfold in-plane magnetic anisotropy is expected, which is illustrated in the polar diagrams of the relative remanence (see Figs. 6.5 and 6.7). The easy axes are aligned in  $45^\circ$  and  $135^\circ$  directions which are  $\langle 100 \rangle$  directions of the iron film according to the  $\varphi$ -scan. Similar results on the magnetization energy and the remanence of epitaxial iron films grown on a Au(100) buffer layer on MgO(100) substrates were achieved by Brockmann [Bro97] and on an MgO(100) substrate by Subagyo [Sub99].

The observations concerning the magnetocrystalline anisotropy are supported by the analysis of the normalized anisotropy constants  $K_1/M_s$  of the fourfold anisotropy,  $K_u/M_s$  of the uniaxial anisotropy and  $K_0/M_s$  for the isotropic part. According to Brockmann et al. [Bro97] the equation

$$\frac{E_m}{M_s}(\varphi) = \frac{K_0}{M_s} + \frac{K_1}{4 \cdot M_s} \sin^2 [2(\varphi - \varphi_1)] + \frac{K_u}{M_s} \sin^2(\varphi - \varphi_u) \quad (6.1)$$

was used to fit the normalized magnetization energy, as described in section 4.1.2. The uniaxial as well as the isotropic anisotropy constant are smaller than 3 Oe in all specimens; only the fourfold anisotropy constant is very strong:  $K_1/M_s = 180(10)$  Oe.  $K_1/M_s$  is the same for all films in as-deposited and in irradiated state. Considering the bulk saturation magnetization of iron  $M_s = 1711$  emu/cm<sup>3</sup>, the cubic anisotropy constant is derived as  $K_1 = 3.1(2) \times 10^5$  erg/cm<sup>3</sup>, which is smaller than the cubic anisotropy constant of bulk bcc Fe at 300 K ( $K_{1,bulk} = 4.2 \times 10^5$  erg/cm<sup>3</sup> [Bro97]). Nevertheless, the order of magnitude matches, which is a good result for this rough estimation.

In contrast to  $E_m/M_s$  of the MOKE analysis, MOMS results in a twofold symmetry for several samples. Particularly MGO-M<sub>irr</sub> and MGO-I<sub>irr</sub> have a very pronounced spin alignment in  $133^\circ$  and  $45^\circ$  direction. According to the results of section 3.3, this alignment in one easy axis direction is most likely a result of the external magnetic field applied during irradiation, and not necessarily a result of the ion irradiation itself. Specimen MGO-S<sub>irr</sub>, which was irradiated without magnetization, has a less pronounced spin alignment.

The twofold symmetry observed by means of MOMS is also visible in the  $H_c$  graphs of the specimens MGO-M<sub>irr</sub>, MGO-I<sub>asdep</sub> and MGO-I<sub>irr</sub>: the angles  $\psi_a$  measured with MOMS for the samples with a strong uniaxial contribution are oriented parallel to the axis with the highest  $H_c$  (see description in section 6.3). The correlated value of  $c_a$  is larger than 0.7. The spin distribution is hardly anisotropic ( $c_a < 0.58$ ) for the specimens with a nearly fourfold  $H_c$  (MGO-S<sub>asdep</sub>, MGO-S<sub>irr</sub> and MGO-M<sub>asdep</sub>). Only MGO-M and MGO-I were irradiated in the presence of an external magnetic field and thus the orientation of the specimen-magnetization during ion bombardment might be a possible explanation for the twofold symmetry. As described in section

5.4.2, a uniaxial anisotropy might be the result of an inhomogeneous distribution of defects. However, the anisotropy constants derived in chapter 4.1 were  $\approx 1 \times 10^4$  erg/cm<sup>3</sup>, while the magnetocrystalline anisotropy as estimated above is  $\approx 3 \times 10^5$  erg/cm<sup>3</sup>. In conclusion, it might be possible that uniaxial anisotropy is present in the irradiated films, but nearly vanishes in comparison with the large cubic term. The anisotropic alignment of the defects might be a reason for the twofold shape of  $H_c(\varphi)$ .

## Chapter 7

# Summary and outlook

The subject of this work has been the investigation of ion-beam induced magnetic anisotropies of iron films. The influence of several parameters on the texturing effects was examined. The deposition method (electron-beam evaporation, pulsed laser deposition) and the substrate (SiO<sub>2</sub>, Si(100) and MgO(100)) are the most fundamental ones. In addition to these parameters, which have an influence on the properties of the as-deposited films, the effects of the ion fluence and mass, the external mechanical stress and the sample pre-magnetization before the ion irradiation were analyzed. For the characterization of the magnetic and structural properties of the films, the magneto-optical Kerr effect (MOKE), magnetic orientation Mössbauer spectroscopy (MOMS), Rutherford backscattering spectroscopy (RBS), X-ray diffraction (XRD) and X-ray absorption spectroscopy (EXAFS) were used.

The results reveal the induction of uniaxial magnetic anisotropy in the electron-beam evaporated films on Si(100) and SiO<sub>2</sub> substrates by irradiation with Ne<sup>+</sup>, Fe<sup>+</sup>, Kr<sup>+</sup> or Xe<sup>+</sup> projectiles. The anisotropy symmetry is twofold, containing a local energy minimum perpendicular to the easy axis of the uniaxial anisotropy. This additional easy axis is explained by the blocking effect of low-angle Néel walls, occurring in thin uniaxially anisotropic polycrystalline ferromagnetic films in the hard axis magnetization process. The choice of the substrate had no major influence on the anisotropy formation. Any projectile was capable of inducing the anisotropy, but the required ion fluence to observe the effect was found to be higher for light ions than for heavy ones. Independent of the implanted ion species, a strong decrease in the number of nearest and next nearest neighbors in the crystalline phase was observed due to ion irradiation. The results of the magnetic and structural analyses were compared with the findings of Jenkins and Kirk [Jen78, Jen93, Kir87] on the defect production in metal films by ion irradiation, and those of Antonov [Ant77] who proposed a model for magnetic anisotropy formation by the alignment of ellipsoid-shaped vacancy clusters in grain boundaries. Moreover, the comparison of the present results with the ones presented in the literature [Lie01, Zha00, Zha01, Zha03a, Gup03a, Gup03b] was important to explain the observed anisotropy effect. However, although up to now the presented model of anisotropy formation has not been confirmed by TEM, it is most probably correlated to intense directional ordered defect production, taking place during the ion bombardment.

Parallel to the structural changes in the films, a strong decrease in the coercive field  $H_c$  was observed after the ion irradiation of electron-beam evaporated films. An analysis of the in-plane

films stress in the concerned specimens revealed a reduction of the tensile deposition stress  $\sigma$ , leading to a saturation state with  $\approx -1$  GPa compressive stress for higher fluences. The decrease in  $\sigma$  was faster for heavy ions than for light ones. A qualitatively similar behavior was found for the decrease of  $H_c$  for  $\text{Ne}^+$ ,  $\text{Fe}^+$ ,  $\text{Kr}^+$  and  $\text{Xe}^+$  irradiation. The close relation of  $\sigma$  and  $H_c$  is also predicted in the standard literature [Chi97, Kne62].

Besides the general mechanism of anisotropy formation and ion induced structural changes in the films, several experiments were carried out to find the parameters which determine the orientation of the induced anisotropy. In contrast to the earlier results on nickel films, the uniaxial anisotropy could not be aligned by the application of mechanical stress during ion implantation. In this context, the magnitude of the magnetostriction plays an important role, which is one order of magnitude smaller for iron than for nickel.

The magnetic orientation Mössbauer spectroscopy (MOMS) turned out to be a very useful technique to find the origin of the anisotropy alignment. By comparing the results obtained by means of MOMS and MOKE, good agreement was found for most specimens. The small differences in the resulting easy axis directions are supposed to be a consequence of the magnetic ripple structure of the specimen. Moreover, MOMS provides additional features compared to MOKE, like the isotope selective and the hysteresis-free measurements of the magnetic properties of the sample. With the help of MOMS, external magnetic fields or the magnetization state of the electron-beam evaporated specimens during the irradiation were found to influence the orientation of the easy axis of magnetization. An alignment of the easy axis parallel to the external magnetic field and parallel to the remanent magnetization state of the specimens was observed. Additionally, it was found that for non-magnetized samples, the deposition anisotropy decides over the final alignment after ion irradiation.

The findings concerning the films deposited by means of PLD on Si(100) substrates are somewhat different. In contrast to the electron-beam evaporated specimens, no significant magnetic anisotropy was observed, neither as-deposited nor after ion irradiation ( $1 \times 10^{16} \text{ Xe}^+/\text{cm}^2$ ) with or without an external magnetic field. Additionally, the as-deposited coercivity of the PLD films was much smaller than that of the electron-beam evaporated samples and its value did not change drastically after ion irradiation. The analysis of the film structure by means of XRD and CEMS revealed two important differences to the former samples: the in-plane deposition stress was quite small and compressive, and the fraction of defects was much smaller both after deposition and ion irradiation. These observations support the assumption that on the one hand the uniaxial anisotropy in the electron-beam evaporated films is correlated to the large number of defects and on the other hand, the strong decrease in  $H_c$  is a consequence of the reduction of in-plane tensile stress.

The Fe/MgO films showed a strong out-of-plane and an in-plane crystal texture, indicating the near-epitaxy of the growth. Consequently, a magnetocrystalline anisotropy with a fourfold symmetry was observed and its anisotropy constant was estimated. The ion irradiation with 150 keV  $\text{Xe}^+$  ions ( $1 \times 10^{16}/\text{cm}^2$ ) in an external magnetic field had nearly no influence on the anisotropy, as measured by MOKE. Only a small twofold component was observed in  $H_c$ . However, the oscillation of MOMS changed significantly, which might have been induced just by the direction of the external magnetic field during irradiation, but not by the irradiation itself.

Some of the models presented for the discovered physical effects were not confirmed by direct experimental observations. Two points are important in this context: the origin of the high-

---

remanence hysteresis loops in the hard axis direction of the electron-beam evaporated films, as explained in section 5.1, and the microscopic model for the anisotropy formation as described in chapter 5.4. It would be of interest to continue the studies by performing a detailed microscopic analysis of these specific properties. Both effects can be proved by employing high resolution microscopes, for example MFM, Kerr-microscope or Lorentz-microscope for the magnetic properties in the high-remanence hard axis direction, and a high-resolution TEM for the observation of the defect structure of the films.

Generally, the use of high resolution microscopes seems to be essential for the determination of the whole potential of the method presented for the induction of magnetic anisotropy. It was discussed in the introduction that the production of magnetic patterns in thin magnetic films and multilayers is of great interest for industrial applications. Depending on the structure of the film, with the present method it should be possible to induce magnetic anisotropy without introducing foreign atoms into the used film or substrate material. Additionally, due to the small lateral straggling of heavy ions, magnetic structures can be produced with a much better lateral resolution than it is possible with for instance electrons or light ions like  $\text{He}^+$ . For this purpose, heavy ion microbeams or arrays of implantation masks might be useful. For a more detailed study, the microscopic detection of the modified areas would be necessary, including for example the hysteresis or the switching properties.

Besides these potential future projects involving many microscopic methods, the deposition and analysis of PLD films or films deposited by other methods seems to be interesting. Several of the results presented here, particularly those on silicon substrate, are not yet completely understood and would demand further experiments. At least one complete series of irradiations with different fluences seems to be necessary, because up to now it is not even known whether it is possible to induce magnetic anisotropy in Fe/Si PLD films. The construction of a PLD chamber at the II. Physikalisches Institut, Universität Göttingen is nearly finished now and it will allow the extension of the experiments on PLD films.

# Appendix A

## PCSA-ellipsometry

In this part the theoretical background of the PCSA-ellipsometer, the formalism of Jones vectors and Jones matrices will be reviewed briefly. A more detailed description can be found in [Azz77, Mue97, Zei91].

Since the interaction of the electric field of a light wave with the electrons in a solid surface is about 1000 times larger than the interaction of the magnetic field, for the Jones formalism only  $\mathbf{E}$  is used. Generally the time and space dependence of the electric field vector of an electromagnetic wave, propagating in  $\mathbf{k}$  direction with wavelength  $\lambda = 2\pi/k$  and frequency  $\nu = \omega/2\pi$ , is described by

$$\mathbf{E}(\mathbf{r}, t) = \begin{pmatrix} E_{0x} e^{i(\mathbf{k}\cdot\mathbf{r} - \omega t + \delta_x)} \\ E_{0y} e^{i(\mathbf{k}\cdot\mathbf{r} - \omega t + \delta_y)} \end{pmatrix} = \mathbf{E}_0 e^{i(\mathbf{k}\cdot\mathbf{r} - \omega t)} \quad (\text{A.1})$$

The information about the polarization state of the light is included in  $\mathbf{E}_0$  or in particular in the amplitudes  $E_{0x}$  and  $E_{0y}$  and the phase difference  $\delta_y - \delta_x$ . The normalized vector

$$E = \frac{\mathbf{E}_0}{|\mathbf{E}_0|} = \begin{pmatrix} \hat{E}_{0x} \\ \hat{E}_{0y} e^{i(\delta_y - \delta_x)} \end{pmatrix} \quad (\text{A.2})$$

is called *Jones vector* and it can describe all possible polarization states of light. A special case is linear polarized light, having  $\delta = n\pi$ ,  $n = 1, 2, \dots$

$$\mathbf{E} = \begin{pmatrix} \cos \alpha \\ \sin \alpha \end{pmatrix} \quad (\text{A.3})$$

where  $\alpha$  is the angle between  $\mathbf{E}$  and x-axis. Another very common example is left or right circular polarized light (LCP or RCP), having  $\delta = +\pi/2$  or  $\delta = -\pi/2$  and  $|E_{0x}| = |E_{0y}|$

$$\mathbf{E} = \frac{1}{\sqrt{2}} \begin{pmatrix} 1 \\ \pm i \end{pmatrix} \quad (\text{A.4})$$

For  $|E_{0x}| \neq |E_{0y}|$ , the polarization becomes elliptic. The polarization states of both examples are illustrated in Fig. A.1.

Because the polarization state of the light can be defined by a 2-dimensional vector, it is straight-



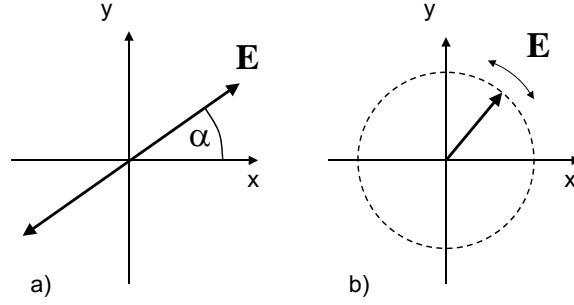


Figure A.1:  $\mathbf{E}$  vector in linear polarized (a) and circular polarized light (b).

forward to describe any change of the polarization by a  $2 \times 2$ -matrix. Therefore every active optical element corresponds to a so called *Jones-matrix*:

$$\mathbf{E}^{\text{res}} = \mathbf{T}\mathbf{E}^{\text{initial}} \quad (\text{A.5})$$

An easy example is an optical rotator that changes the polarization direction of the main axis. With this element, linearly polarized light in x-direction can be transformed to any polarization plane as described by equation (A.3).

$$\mathbf{R}(\alpha) = \begin{pmatrix} \cos \alpha & -\sin \alpha \\ \sin \alpha & \cos \alpha \end{pmatrix} \quad (\text{A.6})$$

$$\Rightarrow \begin{pmatrix} \cos \alpha & -\sin \alpha \\ \sin \alpha & \cos \alpha \end{pmatrix} \begin{pmatrix} 1 \\ 0 \end{pmatrix} = \begin{pmatrix} \cos \alpha \\ \sin \alpha \end{pmatrix}$$

Against this background one can describe the PCSA-ellipsometer setup theoretically by just deriving the Jones-matrices of the used optical elements and calculating the theoretical intensity at the detector. The derivation of the matrices is figured out in [Azz77].

- Polarizer:  $\mathbf{P}^{\text{xy}} = (\mathbf{R}(\alpha))^{-1} \begin{pmatrix} 1 & 0 \\ 0 & 0 \end{pmatrix} \mathbf{R}(\alpha)$

The ideal polarizer has one transmission and one extinction axis t and e, making an orthogonal coordinate system. The optical rotator matrices (see equation (A.6)) describes the transformation of the t-e coordinates to any coordinate system, having an angle  $\alpha$  to the x-y system of the light, where x is in the incidence plane of the light and y is perpendicular.

- Compensator or  $\lambda/4$ -plate:  $\mathbf{C}^{\text{xy}} = (\mathbf{R}(\alpha))^{-1} \begin{pmatrix} 1 & 0 \\ 0 & -i \end{pmatrix} \mathbf{R}(\alpha)$

The ideal compensator has two optical axes, one fast (f) and one slow (s) axis, perpendicular to each other. The fraction of the  $\mathbf{E}$  vector passing the slow axis is retarded by  $\lambda/4$  with respect to the fraction passing the fast axis, making a transformation from linearly polarized light into elliptically polarized light or vice versa possible.

- Modulator:  $\mathbf{M}^{\mathbf{xy}}(t) = (\mathbf{R}(\alpha))^{-1} \begin{pmatrix} e^{i\pi/2 \sin \omega t} & 0 \\ 0 & 1 \end{pmatrix} \mathbf{R}(\alpha)$

A modulator is - like a compensator - a birefringent crystal, in which the refraction index of one axis is modulated. By the modulation a time dependent variation of the phase shift of the components of the Jones vector is induced. For  $t = 0, T/2, T, \dots$ ,  $\mathbf{M}^{\mathbf{xy}}(t) = 1$ , for  $t = T/4, 3T/4, \dots$ , the influence is maximized.

- Sample:  $\mathbf{S} = \begin{pmatrix} R_p & R_{po} \\ R_{op} & R_o \end{pmatrix}$

The matrix of the sample is generally described by the reflection coefficients, which are different for parallel (p) and orthogonal (o) polarizations of the incident light. Since the Kerr effect is based on the different reflection and absorption effects concerning left and right circular polarized light, the Jones matrix can be simplified by using a coordinate system of left and right circular polarized light.  $\mathbf{S}$  has then the diagonal form

$$\mathbf{S} = \begin{pmatrix} \hat{R}_+ & 0 \\ 0 & \hat{R}_- \end{pmatrix} \quad (\text{A.7})$$

with the components  $\hat{R}_+ = R_+ e^{i\phi_+}$  and  $\hat{R}_- = R_- e^{i\phi_-}$ .

The next step is now the correlation of the time dependent light intensity at the detector with Kerr ellipticity  $\epsilon_{Kerr}$  and Kerr rotation  $\phi_{Kerr}$ . Thus all Jones matrices of the optical elements, having the correct orientation relative to the coordinate system, are applied in the correct order to the Jones vector of the emitted light. A detailed description of this procedure for a similar setup as described in 3.1.2 can be found in [Mue97]. The measured intensity is found to be

$$I_{Det} = \frac{RE_0^2}{4} (1 - 2\epsilon \cos \delta + \sin(2\alpha + \Delta\phi) \sin \delta) \quad (\text{A.8})$$

where  $\alpha$  is the orientation of the analyzer,  $\delta = \frac{\pi}{2} \sin \omega t$  is the time dependent phase shift,  $\epsilon_{Kerr} = \frac{1}{2} \frac{r_+^2 - r_-^2}{r_+^2 + r_-^2}$  is the Kerr ellipticity and  $\phi_{Kerr} = -\frac{1}{2} \Delta\phi = -\frac{1}{2}(\phi_+ - \phi_-)$  the Kerr rotation. As can be seen in (A.8),  $\epsilon_{Kerr}$  and  $\phi_{Kerr}$  can be easily separated, since they occur in separate terms of the function. The frequency of the ellipticity part is two times larger than the frequency of the rotation term. Developing  $\cos \delta$  and  $\sin \delta$  with Bessel functions results in the expression:

$$I_{Det} \approx \frac{RE_0^2}{8} \left( 1 - J_0\left(\frac{\pi}{2}\right) 2\epsilon + 2(\alpha - \phi) J_1\left(\frac{\pi}{2}\right) \sin \omega t - 2\epsilon J_2\left(\frac{\pi}{2}\right) \sin 2\omega t + \dots \right). \quad (\text{A.9})$$

If the intensity is correlated to the modulation frequency  $\nu = 50$  kHz by a Lock-in amplifier, the measurement of the first harmonic results in

$$U_{MOKE}(\omega) \propto J\left(\frac{\pi}{2}\right) (\alpha - \phi), \quad (\text{A.10})$$

which results in the relative value of the Kerr rotation and consequently (see section 3.1.1) the relative magnetization of the sample.

## Appendix B

# CEMS Parameters

Sample	sextet 1			sextet 2			sextet 3			doublet		
	$F_1$ [%]	$B_{HF}$ [T]	$\delta$ [mm/s]	$F_2$ [%]	$B_{HF}$ [T]	$\delta$ [mm/s]	$F_3$ [%]	$B_{HF}$ [T]	$\delta$ [mm/s]	$F_D$ [%]	$\Delta$ [mm/s]	$\delta$ [mm/s]
1- $I_{asdep}$	78.3(32)	33.2(1)	0.01(1)	10.0(46)	27.7(3)	0.04(4)	8.2(31)	20.1(4)	0.05(5)	3.5(11)	0.98(8)	0.20(5)
1- $I_{relaxed}$	70.1(40)	32.9(1)	0.04(1)	9.5(33)	27.2(2)	0.15(3)	8.9(30)	18.7(4)	0.06(7)	11.5(10)	0.73(1)	0.20(2)
1- $M_{asdep}$	100	33.3(1)	0.00(1)	—	—	—	—	—	—	—	—	—
1- $M_{relaxed}$	100	33.0(1)	0.00(1)	—	—	—	—	—	—	—	—	—
1- $S_{asdep}$	89.7(22)	33.0(1)	-0.02(1)	6.8(21)	26.4(4)	-0.01(2)	—	—	—	3.7(9)	1.28(23)	0.28(3)
1- $S_{relaxed}$	73.7(19)	33.0(1)	0.01(1)	14.8(20)	26.6(10)	0.04(2)	—	—	—	11.5(14)	1.20(10)	0.32(2)
2- $M_{asdep}$	90.1(13)	33.0(1)	0.01(1)	4.3(10)	27.0(7)	-0.01(2)	3.5(8)	18.8(35)	-0.02(2)	2.1(4)	1.16(22)	0.40(5)
2- $M_{bent}^a$	81.3(28)	33.0(1)	0.01(1)	7.9(22)	27.0(10)	0.01(2)	6.2(47)	20.1(12)	0.02(2)	2.1(13)	1.3(0)	0.3(0)
2- $M_{irr}$	83.4(29)	33.2(1)	0.01(1)	8.2(18)	27.5(11)	-0.01(3)	5.4(22)	20.1(14)	0.00(5)	3.0(12)	1.18(12)	0.34(7)
2- $M_{relaxed}$	85.4(19)	33.1(1)	0.01(1)	8.0(14)	27.1(7)	0.01(3)	3.8(23)	19.7(15)	0.02(7)	2.7(7)	1.20(14)	0.36(6)
2- $B_{asdep}$	87.4(24)	32.9(1)	0.01(1)	6.6(16)	27.4(16)	0.07(4)	6.1(14)	18.2(17)	-0.05(5)	—	—	—
2- $B_{mag}$	87.5(13)	33.0(1)	0.01(1)	6.7(14)	27.3(11)	0.08(4)	4.8(15)	20.2(11)	-0.01(2)	1.1(7)	1.3(0)	0.30(9)
2- $B_{irr}$	82.3(27)	33.1(1)	0.02(1)	9.5(15)	27.5(5)	0.05(2)	5.6(21)	20.0(7)	0.05(3)	2.6(5)	1.28(39)	0.38(6)
2- $B_{relaxed}$	86.4(18)	33.1(1)	0.02(1)	6.2(9)	27.4(7)	0.00(1)	4.0(16)	20.3(9)	0.07(3)	3.5(6)	1.29(25)	0.36(5)
2- $S_{asdep}$	85.2(34)	32.9(1)	0.02(1)	6.9(22)	27.3(12)	0.06(5)	7.9(26)	19.3(15)	0.06(5)	—	—	—
2- $S_{mag}$	85.4(31)	32.9(1)	0.01(1)	6.6(11)	27.2(4)	0.02(6)	6.3(29)	19.7(5)	0.10(7)	1.7(8)	1.36(29)	0.34(15)
2- $S_{irr}$	69.3(22)	33.0(1)	0.00(1)	12.9(19)	27.2(2)	-0.01(3)	9.5(27)	18.9(3)	0.11(4)	8.4(14)	1.13(6)	0.33(3)

Table B.1: Most important fit parameters of the CEMS spectra.  $F_i$  assigns the area fraction of the concerned site,  $B_{HF}$  the hyperfine fields,  $\Delta$  the quadrupole splitting of the doublet and  $\delta$  is the center shift.

<sup>a</sup>additional singlet site:  $F_S = 3.2(17)$ ,  $\delta = -0.12(2)$  mm/s

Sample	sextet 1			sextet 2			sextet 3			doublet		
	$F_1$ [%]	$B_{HF}$ [T]	$\delta$ [mm/s]	$F_2$ [%]	$B_{HF}$ [T]	$\delta$ [mm/s]	$F_3$ [%]	$B_{HF}$ [T]	$\delta$ [mm/s]	$F_D$ [%]	$\Delta$ [mm/s]	$\delta$ [mm/s]
SI-S <sub>asdep</sub>	94.6(11)	32.9(1)	-0.01(1)	4.3(7)	29.6(2)	-0.01(2)	—	—	—	0.4(2)	1.10(8)	0.38(4)
SI-S <sub>irr</sub>	77.2(25)	33.2(1)	0.03(1)	18.3(28)	30.2(2)	0.03(1)	—	—	—	4.5(6)	0.97(7)	0.29(4)
SI-M <sub>asdep</sub>	90.6(18)	32.9(1)	-0.01(1)	8.5(19)	29.8(2)	-0.03(1)	—	—	—	0.9(6)	1.22(20)	0.28(9)
SI-M <sub>irr</sub>	75.7(21)	33.1(1)	0.03(1)	22.2(22)	30.3(1)	0.02(1)	—	—	—	2.1(10)	1.07(13)	0.23(6)
SI-I <sub>asdep</sub>	80.3(28)	33.0(1)	-0.01(1)	14.1(29)	29.8(2)	-0.01(2)	2.4(24)	17.4(3)	0(0)	3.1(9)	0.99(12)	0.30(7)
SI-I <sub>irr</sub>	53.8(42)	32.9(1)	0.04(1)	21.3(44)	29.7(2)	0.04(1)	—	—	—	24.9(8)	0.61(1)	0.26(1)
MGO-S <sub>asdep</sub>	94.0(20)	33.0(1)	0.01(1)	4.4(8)	29.1(6)	0.01(7)	—	—	—	0.9(5)	0.96(11)	0.25(5)
MGO-S <sub>irr</sub>	83.0(55)	33.1(1)	0.01(1)	14.3(55)	30.2(1)	-0.02(1)	—	—	—	2.7(12)	1.21(14)	0.38(7)
MGO-M <sub>asdep</sub>	90.0(23)	33.0(1)	0.00(1)	8.1(20)	29.8(3)	-0.01(3)	—	—	—	0.8(3)	1.17(21)	0.18(11)
MGO-M <sub>irr</sub>	76.7(22)	33.3(1)	0.00(1)	23.3(22)	30.5(1)	-0.01(1)	—	—	—	—	—	—
MGO-I <sub>asdep</sub>	93.8(26)	33.0(1)	0.01(1)	3.4(20)	28.5(4)	-0.04(5)	—	—	—	2.8(13)	1.05(14)	0.20(6)
MGO-I <sub>irr</sub>	85.7(31)	33.0(1)	0.01(1)	11.2(22)	30.2(2)	0.02(2)	—	—	—	3.0(20)	0.78(8)	0.41(5)

Table B.2: Most important fit parameters of the CEMS spectra.  $F$  assigns the area fraction of this site,  $B_{HF}$  the hyperfine field and  $\delta$  the center shift.

# Bibliography

- [And79] H. H. Andersen, *Appl. Phys.* **18**, 131 (1979)
- [Ant77] L. I. Antonov, V. V. Veter, L. A. Yudina, G. V. Kozodoy, E. L. Fedorova, and V. V. Yudin, *Fiz. metal. metalloved.* **43**(3), 518 (1977)
- [Arg55] P. N. Argyres, *Phys. Rev.* **97**, 334 (1955)
- [Ash76] N. W. Ashcroft, and N. D. Mermin, *Solid State Physics*, Saunders Company, Philadelphia (1976)
- [Ave94] R. S. Averback, *J. Nucl. Mat.* **216**, 49 (1994)
- [Azz77] R. M. A. Azzam, and N. M. Bashara, *Ellipsometry and Polarized light*, North-Holland, Amsterdam (1977)
- [Bad87] S. D. Bader, and E. R. Moog, *J. Appl. Phys.* **61**, 3729 (1987)
- [Bai88] M. N. Baibich, J. M. Broto, A. Fert, F. Nguyen Van Dau, F. Petroff, P. Etienne, G. Creuzet, A. Friederich, and J. Chazelas, *Phys. Rev. Lett.* **61**, 2472 (1988)
- [Bar97] N. Barradas, C. Jeynes, and R. P. Webb, *Appl. Phys. Lett.* **71**, 291 (1997)
- [Bar98] N. Barradas, P. K. Marriott, C. Jeynes, and R. P. Webb, *Nucl. Instr. and Meth. B* **136-138**, 1157 (1998)
- [Bay83] G. Bayreuther, *J. Vac. Sci. Technol.* **A1**(1), 19 (1983)
- [Bel70] H. S. Belson, B.F. Desavage, R. S. Tebble, and M. R. Parker, *IEEE Trans. Magn.* **MAG-6**, 722 (1970)
- [Ben65] H. S. Bennett, and E. A. Stern, *Phys. Rev.* **137**, A448 (1965)
- [Ber70] Bergmann-Schaefer, *Lehrbuch der Experimentalphysik, Band I: Mechanik, Akustik, Wärme*, Walter de Gruyter & Co., Berlin (1970)
- [Ber01a] D. Berling, P. Bertoncini, A. Mehdaoui, P. Wetzel, G. Gewinner, and B. Loegel, *J. Magn. Magn. Mater.* **237**, 181 (2001)
- [Ber01b] P. Bertoncini, P. Wetzel, D. Berling, A. Mehdaoui, B. Loegel, G. Gewinner, R. Poinso, and V. Pierron-Bohnes, *J. Magn. Magn. Mater.* **237**, 191 (2001)

- [Bie80] J. P. Biersack, and L. G. Haggmark, Nucl. Instr. and Meth. **174**, 257 (1980)
- [Bin89] G. Binasch, P. Grünberg, F. Saurenbach, and W. Zinn, Phys. Rev. B **39**, 4828 (1989)
- [Bla85] N. Blaes, H. Fischer, and U. Gonser, Nucl. Instr. and Meth. B **9**, 201 (1985)
- [Bla90] J. A. C. Bland, M. J. Baird, H. T. Leung, A. J. R. Ives, K. D. Mackay, and H. P. Hughes, J. Magn. Magn. Mater. **113**, 178 (1990)
- [Bol94] W. Bolse, Mat. Sci. Eng. **R12**, 53 (1994)
- [Boz51] R. M. Bozorth, *Ferromagnetism*, Van Nostrand, New York (1951), p. 441
- [Boz53] R. M. Bozorth, and J. G. Walker, Phys. Rev. **89**, 624 (1953)
- [Bro97] M. Brockmann, S. Miethaner, R. Onderka, M. Köhler, F. Himmelhuber, H. Regensburger, F. Bensch, T. Schweinböck, and G. Bayreuther, J. Appl. Phys. **81**, 5047 (1997)
- [Car02] E. Carpena, Dissertation, Göttingen (2002)
- [Cha98] C. Chappert, H. Bernas, J. Ferr, V. Kottler, J.-P. Jamet, Y. Chen, E. Cambril, T. Devolder, F. Rousseaux, V. Mathet, and H. Launois, Science **280**, 1919 (1998)
- [Cha02] G. S. Chang, T. A. Callcott, G. P. Zhang, G. T. Woods, S. H. Kim, S. W. Shin, K. Jeong, C. N. Whang, and A. Moewes, Appl. Phys. Lett. **81**, 3016 (2002)
- [Che90] Y. T. Cheng, Mat. Sci. Rep. **5**, 45 (1990)
- [Chi55] S. Chikazumi, and T. Oomura, J. Phys. Soc. Japan **10**, 842 (1955)
- [Chi52] S. Chikazumi, Phys. Rev. **85**, 918 (1952)
- [Chi64] S. Chikazumi, *Physics of Magnetism*, John Wiley & Sons, Inc., New York, London, Sydney (1964)
- [Chi97] S. Chikazumi, *Physics of Ferromagnetism*, Clarendon Press, Oxford (1997)
- [Chu78] W. K. Chu, J. W. Mayer, and M.-A. Nicolet, *Backscattering Spectrometry*, Academic Press, Orlando (1978)
- [Con35] E. U. Condon, and G. H. Shortley, *The Theory of Atomic Spectra*, Cambridge Univ. Press (1935)
- [Cor89] T. Corts, Diplomarbeit, Göttingen (1989)
- [Coo65] B. R. Cooper, Phys. Rev. **139**, A1504 (1965)
- [Cul78] B. D. Cullity, *Elements of X-RAY DIFFRACTION*, Addison-Wesley (1978)
- [Daa91] G. H. O. Daalderop, PhD Thesis, Delft University of Technology (1991)
- [Daa94] G. H. O. Daalderop, Phys. Rev. B **50**, 9989 (1994)

## BIBLIOGRAPHY

---

- [Dan39] S. M. Dancoff, and P. Morrison, Phys. Rev. **55**, 122 (1939)
- [Des99] J. Desimoni, and F. H. Sanchez, Hyp. Int. **122**, 277 (1999)
- [Dev99a] T. Devolder, C. Chappert, Y. Chen, E. Cambril, H. Bernas, J.-P. Jamet, and J. Ferré, Appl. Phys. Lett **74**, 3383 (1999)
- [Dev99b] T. Devolder, C. Vieu, H. Bernas, J. Ferré, C. Chappert, J. Gierak, J.-P. Jamet, T. Aign, P. Meyer, Y. Chen, F. Rousseaux, V. Mathet, H. Launois, and O. Kaitasov, C. R. Acad. Sci. Paris, t. 327, Série IIB, 915 (1999)
- [Din00] H. F. Ding, S. Pütter, H. P. Oepen, and J. Kirschner, J. Magn. Magn. Mater. **212**, L5 (2000)
- [Din01] H. F. Ding, S. Pütter, H. P. Oepen, and J. Kirschner, Phys. Rev. B **63**, 134425 (2001)
- [Ela88] W. T. Elam, J. P. Kirkland, R. A. Neiser, and P. D. Wolf, Phys. Rev. B **38**, 26 (1988)
- [Ers73] J. L. Erskine, and E. A. Stern, Phys. Rev. B **8**, 1239 (1973)
- [Far92] M. Farle, H. Saffari, W. A. Lewis, E. Kay, and S. B. Hagstrom, IEEE Trans. Magn. **MAG-28**, 2940 (1992)
- [Fel61] E. Feldtkeller, Elektron. Rechenanl. **3**, 167 (1961)
- [Fer30] E. Fermi, Z. Phys. **60**, 320 (1930)
- [Fer99] J. Ferré, C. Chappert, H. Bernas, J.-P. Jamet, P. Meyer, O. Kaitasov, S. Lemerle, V. Mathet, F. Rousseaux, and H. Launois, J. Magn. Magn. Mater. **198-199**, 191 (1999)
- [Fil03] A. Filipponi, V. M. Giordano, S. De Panfilis, A. Di Ciocco, E. Principi, A. Trapananti, M. Borowski, and Jean-Paul Itié, Rev. Sci. Instrum. **74**, 2654 (2003)
- [Fra62] H. Frauenfelder, *The Moessbauer Effect*, New York (1962)
- [Gon75] U. Gonser, *Moessbauer Spectroscopy*, Springer Verlag, Berlin-Heidelberg-New York (1975)
- [Gra93] U. Gradmann, *Magnetism in Ultrathin Transition Metal Films*, in *Handbook of Magnetic Materials*, Elsevier, Amsterdam (1993)
- [Gre71] N. N. Greenwood, and T. C. Gibb, *Mössbauer Spectroscopy*, Chapman and Hall Ltd., London (1971)
- [Gro79] P. Grosse, *Freie Elektronen in Festkörpern*, Springer Verlag (1979)
- [Gup03a] R. Gupta, G. A. Müller, P. Schaaf, K. Zhang, and K.-P. Lieb, Nucl. Instr. and Meth., in press
- [Gup03b] R. Gupta, G. A. Müller, P. Schaaf, K. Zhang, and K.-P. Lieb, to be published
- [Har95] J. F. Harbsmeier, Diplomarbeit, Göttingen (1995)



- [Har00] J. F. Harbsmeier, Dissertation, Göttingen (2000)
- [Hei79] N. Heiman, and N. S. Kazama, *J. Appl. Phys.* **50**(11), 7633 (1979)
- [Hof64] H. Hoffmann, *J. Appl. Phys.* **35**, 1790 (1964)
- [Hof79] H. Hoffmann, *Thin Solid Films* **58**, 223 (1979)
- [Hub88] E. Huber, and E. E. Marinero, *Appl. Phys. A* **47**, 131 (1988)
- [Hub00] A. Hubert, and R. Schäfer, *Magnetic Domains, The Analysis of Magnetic Microstructures*, Springer Verlag (2000)
- [IFF92] *Synchrotronstrahlung zur Erforschung kondensierter Materie, Vorlesungsmanuskript des 23. IFF-Ferienkurses*, Forschungszentrum Jülich GmbH, Jülich (1992)
- [IFF99] *Magnetische Schichtsysteme, Vorlesungsmanuskript des 30. IFF-Ferienkurses*, Forschungszentrum Jülich GmbH, Jülich (1999)
- [Jao01] M. Jaouen, J. Pacaud, and C. Jaouen, *Phys. Rev. B* **64**, 144106 (2001)
- [Jen78] M. L. Jenkins, C. A. English, and B. L. Eyre, *Philos. Mag.* **38**, 97 (1978)
- [Jen93] M. L. Jenkins, M. A. Kirk, and W. J. Phythian, *J. Nucl. Mat.* **205**, 16 (1993)
- [Joh74] P. B. Jonson, and R. W. Christy, *Phys. Rev. B* **9**, 5056 (1974)
- [Joh96] M. T. Johnson, P. J. H. Bloemen, F. J. A. den Broeder, and J. J. de Vries, *Rep. Prog. Phys.* **59**, 1409 (1996)
- [Kir87] M. A. Kirk, I. M. Robertson, M. L. Jenkins, C. A. English, T. J. Black, and J. S. Vetrano, *J. Nucl. Mater.* **149**, 21 (1987)
- [Kit49] C. Kittel, *Rev. Mod. Phys.* **21**, 541 (1949)
- [Kle02] K. V. Klementev, *VIPER for Windows*, [www.desy.de/~klmn/viper.html](http://www.desy.de/~klmn/viper.html)
- [Kle01] K. V. Klementev, *J. Phys. D: Appl. Phys.* **34**, 209 (2001)
- [Klo68] E. Kloholm, *J. Vac. Sci. Tech.* **6**, 138 (1968)
- [Kne62] E. Kneller, *Ferromagnetismus*, Springer-Verlag, Berlin/Göttingen/Heidelberg (1962)
- [Kra72] R. A. Krakowski, and R. B. Miller, *Nucl. Instr. and Meth.* **100**, 93 (1972)
- [Kre97] H.-U. Krebs, *Int. J. Non-Equil. Proc.* **10**, 3 (1997)
- [Kre98] S. Kreuzer, K. Prügl, G. Bayreuther, and D. Weiss, *Thin solid films* **318**, 219 (1998)
- [Kru97] S. Krumm, *WinFit!* for Windows, [www.geol.uni-erlangen.de](http://www.geol.uni-erlangen.de), [krumm@geol.uni-erlangen.de](mailto:krumm@geol.uni-erlangen.de)

- [Kul03] A. Kulinska, K. P. Lieb, G. A. Müller, M. Uhrmacher, and K. Zhang, submitted to J. Magn. Magn. Mater.
- [Lea95] J. A. Leavitt, L. C. McIntyre, Jr., and M. R. Weller, *Backscattering Spectrometry*, in *Handbook of modern ion-beam materials analysis*, J. R. Tesmer, and M. Nastasi, Materials Research Society, Pittsburg (1995)
- [Lee94] Y. H. Lee, Y. D. Shin, K. H. Lee, and J. R. Rhee, J. Appl. Phys. **75**, 5913 (1994)
- [Len92] B. Lengeler, *Röntgenabsorptionsspektroskopie in Synchrotronstrahlung zur Erforschung kondensierter Materie, Vorlesungsmanuskript des 23. IFF-Ferienkurses*, Forschungszentrum Jülich GmbH, Jülich (1992)
- [Les69] A. G. Lesnik, Phys. Stat. Sol. **35**, 959 (1969)
- [Les73] A. G. Lesnik, A. I. Mitsek, and V. N. Pushkar, Phys. Stat. Sol. (a) **17**, 697 (1973)
- [Lew94] W. A. Lewis, M. Farle, B. M. Clemens, and R. L. White, J. Appl. Phys. **75**, 5644 (1994)
- [Lie01] K. P. Lieb, K. Zhang, G. A. Müller, P. Schaaf, M. Uhrmacher, W. Felsch, and M. Münzenberg, Acta Phys. Polon. **100 A**, 751 (2001)
- [Lie03] K. P. Lieb, R. Gupta, G. A. Müller, P. Schaaf, M. Uhrmacher, and K. Zhang, Proc. of the 5th General Conference of the Balkan Physical Union BPU-5 S. Jokic, I. Milosevic, A. Balaz, Z. Nikolic, Eds. Serbian Physical Society, Belgrade, 490 (2003)
- [Mar58] W. Marshall, Phys. Rev. **110**, 1280 (1958)
- [Mar96] N. A. Marks, D. R. McKenzie, and B. A. Pailthorpe, Prys. Rev. B **53**, 4117 (1996)
- [Mei03] C. Meier, D. Reuter, C. Riedesel, and A. D. Wieck, J. Appl. Phys. **93**, 6100 (2003)
- [Mis98] A. Misra, S. Fayeulle, H. Kung, T. E. Mitchell, and M. Nastasi, Appl. Phys. Lett. **73**, 891 (1998)
- [Miy95] T. Miyazaki, and T. Tezuka, J. Magn. Magn. Mater. **139**, L231 (1995)
- [Moe58] R. L. Mößbauer, Z. Physik **151**, 124 (1958)
- [Moe01] J. Moers, *Litography in Neue Materialien für die Informationstechnik, Vorlesungsmanuskript des 32. IFF-Ferienkurses*, Forschungszentrum Jülich GmbH, Jülich (2001)
- [Moo96] J. S. Moodera, and L. R. Kinder, J. Appl. Phys. **79**, 4724 (1996)
- [Moo89] E. R. Moog, J. Zak, M. L. Huberman, and S. D. Bader, Phys. Rev. B **39**, 9496 (1989)
- [Mor65] A. H. Morrish, *The Physical Principles of Magnetism*, Wiley & Sons, New York (1965)
- [Mue87] K.-H. Müller, J. Appl. Phys. **62**, 1796 (1987)
- [Mue97] M. Münzenberg, Diplomarbeit, Göttingen (1997)

- [Mue03a] G. A. Müller, R. Gupta, K.-P. Lieb, and P. Schaaf, *Appl. Phys. Lett.* **82**, 73 (2003)
- [Mue03b] G. A. Müller, A. Kulinska, K. Zhang, R. Gupta, P. Schaaf, M. Uhrmacher, and K. P. Lieb, *Hyp. Int.*, in press
- [Nas96] M. Nastasi, J. W. Mayer and J. K. Hirvonen, *Ion-Solid Interactions*, Cambridge University Press, Cambridge (1996)
- [Nee53] L. Néel, *Compt. Rend.* **237**, 1953 (1953)
- [Neu96] M. Neubauer, Dissertation, Göttingen (1996)
- [Neu98] M. Neubauer, N. Reinecke, M. Uhrmacher, K. P. Lieb, M. Münzenberg, and W. Felsch, *Nucl. Instr. Meth. B* **139**, 332 (1998)
- [Now84] J. Nowak, and E. Szibel, *IEEE Trans. Magn.* **MAG-20**, 2105 (1984)
- [Now92] J. Nowak, *J. Appl. Phys.* **72**, 1490 (1992)
- [Now93] J. Nowak, *J. Appl. Phys.* **73**, 5125 (1993)
- [Nye85] J. F. Nye, *Physical Properties of Crystals*, Oxford University Press, Oxford (1985)
- [Osg98] R. M. Osgood III, S. D. Bader, B. M. Clemens, R. L. White, and H. Matsuyama, *J. Magn. Magn. Mater.* **182**, 297 (1998)
- [PDF97] *Powder Diffraction File database PDF-2*, International Centre for Diffraction Data, Newton Square (1997)
- [Pos02] K. Postava, D. Hrabovsky, J. Pistora, A. R. Fert, S. Visnovsky, and T. Yamaguchi, *J. Appl. Phys.* **91**, 7293 (2002)
- [Pre86] P. S. Prevey, *Metals Handbook 10*, American Society for Metals, p. 380 (1986)
- [Reu01] H. Reuther, G. Behr, and A. Teresiak, *J. Phys.: Condens. Matter* **13**, L225 (2001)
- [Reu03] D. Reuter, C. Riedesel, P. Schafmeister, C. Meier, and A. D. Wieck, *Appl. Phys. Lett.* **82**, 481 (2003)
- [Ric91] H. J. Richter, and H. Hibst, *J. Magn. Magn. Mater.* **95**, 118 (1991)
- [Rie74] H. Riedel, *Phys. Stat. Sol. (a)* **24**, 449 (1974)
- [Rix93] G. Rixecker, P. Schaaf, and U. Gonser, *Phys. stat. sol. (a)* **139**, 309 (1993)
- [Rix95] G. Rixecker, P. Schaaf, and U. Gonser, *Phys. stat. sol. (a)* **151**, 291 (1995)
- [Rob63] C. C. Robinson, *J. Opt. Soc. Am.* **53**, 681 (1963)
- [Rob83] T. M. Robinson, *Phys. Stat. Sol. (a)* **75**, 243 (1983)
- [Rub92] T. D. de la Rubia, and W. J. Phythian, *J. Nucl. Mater.* **191-194**, 108 (1992)

- [Rut11] E. Rutherford, *Philos. Mag.* **21**, 669 (1911)
- [San91] F. H. Sanchez, M. B. Fernandez van Raab, and J. Desimoni, *Phys. Rev. B* **44**, 4290 (1991)
- [San99] D. Sander, *Rep. Prog. Phys.* **62**, 809 (1999)
- [Say71] D. E. Sayers, E. A. Stern, and F. W. Lytle, *Phys. Rev. Lett.* **27**, 1204 (1971)
- [Say88] D. E. Sayers and B. A. Bunker, in *X-ray Absorption*, D. C. Koningsberger and R. Prins, John Wiley and Sons, New York (1988)
- [Sch91] P. Schaaf, Dissertation, Saarbrücken (1991)
- [Sch97] G. Schatz, A. Weidinger, *Nukleare Festkörperphysik*, Teubner Verlag, Stuttgart (1997)
- [Sch02] P. Schaaf, G. A. Müller, E. Carpena, and M. Kahle, *Hyp. Int.* **144/145**, 129 (2002)
- [Sch03] P. Schaaf, G. A. Müller, and E. Carpena, in *Mössbauer Spectroscopy in Materials Science*, NATO Science Series, ed. by M. Migliorini, M. Mashlan and P. Schaaf, Kluwer Academic, Dordrecht (2003)
- [Sei56] F. Seitz, and J. S. Koehler, *Solid State Phys.* **2**, 305 (1956)
- [Sei87] D. N. Seidman, R. S. Averback, and M. W. Guinan, *Phys. Stat. Sol. (b)* **144**, 85 (1987)
- [Sig74] P. Sigmund, *Appl. Phys. Lett.* **25**, 169 (1974)
- [Spi81] J. J. Spijkermann, *Conversion electron Mössbauer spectroscopy in Mössbauer Effect Methodology, Vol. 7*, I. J. Gruvermann, Ed. Plenum Press, New York-London (1981)
- [Sko99] R. Skomski, and J. M. D. Coey, *Permanent Magnetism*, Institute of Physics Publishing, Bristol and Philadelphia (1999)
- [SRI03] *Stopping Range of Ions in Matter*, SRIM2003 for Windows, [www.srim.org/SRIM/SRIM2003.html](http://www.srim.org/SRIM/SRIM2003.html)
- [Ste88] E. A. Stern, in *X-ray Absorption: Principles, Applications, Techniques of EXAFS, SEXAFS and XANES*, D. C. Koningsberger and R. Prins, Wiley, New York (1988)
- [Sto36] E. C. Stoner, *Proc. Roy. Soc. A* **154**, 656 (1936)
- [Sto38] E. C. Stoner, *Proc. Roy. Soc. A* **165**, 372 (1938)
- [Sto09] G. G. Stoney, *Proc. Royal Soc. (London) A* **82**, 172 (1909)
- [Stu00] K. Sturm, Dissertation, Göttingen (2000)
- [Sub99] A. Subagyó, K. Sueoka, K. Mukasa, and K. Hayakawa, *Jpn. J. Appl. Phys.* **38**, 3820 (1999)
- [Sue01] E. Súske, Diplomarbeit, Göttingen (2001)

- [Tak78] M. Takahashi, and T. Kono, Jap. J. Appl. Phys. **17**, 361 (1978)
- [Tak79] M. Takahashi, S. Kadowaki, T. Wakiyama, T. Anayama, and M. Takahashi, J. Phys. Soc. Japan **47**, 1110 (1979)
- [Tak90] T. Takayama and Y. Matsumoto, *Advances in X-ray Analysis, Vol. 33*, C. S. Barrett, Plenum Press, New York (1990)
- [Tan54] S. Taniguchi, and M. Yamamoto, Sci. Rep. Res. Inst. Tohoku Univ. A **6**, 330 (1954)
- [Tay91] R. D. Taylor, M. P. Pasternak, and R. Jeanloz, J. Appl. Phys. **69**(8), 6126 (1991)
- [Tem86] C. Templier, H. Garem, and J. P. Riviere, Philos. Mag. A **53**, 667 (1986)
- [Tes95] J. R. Tesmer, and M. Nastasi (Eds.), *Handbook of modern ion-beam materials analysis*, Materials Research Society, Pittsburg (1995)
- [Tho89] J. A. Thornton, and D. W. Hoffman, Thin Solid Films **171**, 5 (1989)
- [Uhr85] M. Uhrmacher, K. Pampus, F. J. Bergmeister, D. Purschke, and K. P. Lieb, Nucl. Instr. and Meth. B **9**, 234 (1985)
- [Wag76] F. E. Wagner, J. de Physique **37** C6, 673 (1976)
- [Was90] G. S. Was, Prog. Surf. Sci. **32**, 211 (1990)
- [Wat61] R. E. Watson, and A. J. Freeman, Phys. Rev. **123**, 2027 (1961)
- [Web96] W. Weber, R. Allenspach, and A. Bischof, Appl. Phys. Lett. **70**, 520 (1996)
- [Weg66] H. Wegener, *Der Mössbauereffekt und Seine Anwendungen in Physik und Chemie*, Bibliographisches Institut, Hochschultaschenbücher, Mannheim (1966)
- [Wei02] M. Weisheit, Dissertation, Göttingen (2002)
- [Wil57] H. J. Williams, and R. C. Sherwood, J. Appl. Phys. **28**, 548 (1957)
- [Win91] D. Winau, R. Koch, and K. H. Rieder, Appl. Phys. Lett. **59**, 1072 (1991)
- [Woi00] Th. Woike, M. Imlau, V. Angelov, J. Schefer, and B. Delley, Phys. Rev. B **61**, 12249 (2000)
- [Woo02] S. I. Woods, S. Ingvarsson, J. R. Kirtley, H. F. Hamann, and R. H. Koch, Appl. Phys. Lett. **81**, 1267 (2002)
- [Yan93] Z. J. Yang, and M. R. Scheinfein, J. Appl. Phys. **74**(11), 6810 (1993)
- [Yan00] S. Yan, R. Schreiber, P. Grünberg, and R. Schäfer, J. Magn. Magn. Mat. **210**, 309 (2000)
- [Zei91] T. Zeidler, Diplomarbeit, Bochum (1991)

## BIBLIOGRAPHY

---

- [Zem89] T. Zemcik, L. Kraus, and K. Zaveta, *Hyp. Int.* **51**, 1051 (1989)
- [Zha00] K. Zhang, K. P. Lieb, P. Schaaf, M. Uhrmacher, W. Felsch, and M. Münzenberg, *Nucl. Instr. Meth. B* **161-163**, 1016 (2000)
- [Zha01] K. Zhang, Dissertation, Göttingen (2001)
- [Zha03a] K. Zhang, K. P. Lieb, G. A. Müller, P. Schaaf, M. Uhrmacher, and M. Münzenberg, submitted to *Phys. Rev. B*
- [Zha03b] Kun Zhang, R. Gupta, K. P. Lieb, Y. Luo, G. A. Müller, P. Schaaf, and M. Uhrmacher, submitted to *J. Magn. Magn. Mat.*
- [Zha03c] Kun Zhang, R. Gupta, K. P. Lieb, Y. Luo, G. A. Müller, P. Schaaf, and M. Uhrmacher, *Europhys. Lett.* **64**, 668 (2003)
- [Zho90] Q. M. Zhong, A. S. Arrott, B. Heinrich, and Z. Celinski, *J. Appl. Phys.* **67**, 4448 (1990)
- [Zie85] J. F. Ziegler, J. P. Biersack, and U. Littmark, *The Stopping and Ranges of Ions in Solids*, Pergamon, New York (1985)
- [Zie99] J. F. Ziegler, J. P. Biersack, and U. Littmark, *The Stopping and Ranges of Ions in Solids*, Pergamon Press, New York (1999), Vol. 1
- [Zim75] J. M. Ziman, *Prinzipien der Festkörpertheorie*, Verlag Harri Deutsch (1975)

# Danksagung

Mein erster Dank gilt meinem Doktorvater Herrn Prof. Lieb, der durch seine Begeisterung, seine immerwährende Diskussionsbereitschaft und stetes Interesse an neusten Ergebnissen großen Anteil am Gelingen dieser Arbeit hat.

Herzlichen Dank auch an Herrn Juniorprof. Dr. Markus Münzenberg für sein Interesse an diesem Projekt und seine spontane Bereitschaft, die vorliegende Arbeit zu korreferieren.

Ein großer Dank gilt auch Herrn PD Dr. Peter Schaaf, der dieser Arbeit wesentliche Impulse gab, nicht zuletzt durch die Idee für die MOMS Methode. Vielen Dank auch für die vielen Diskussionen, gerade in kritischen Phasen der Arbeit.

Bei Herrn Dr. Michael Uhrmacher möchte ich mich besonders für die produktiven Diskussionen zur Strukturierung der Arbeit bedanken. Seine Lesebereitschaft und die vielen Ideen, die während dieser Zeit einflossen, waren sehr hilfreich.

Thanks also to Dr. Ratnesh Gupta and Dr. Kun Zhang. Both of them contributed much to the good working atmosphere in our group. Also many thanks for all discussions (private and scientific) and meetings we survived together.

Special thanks also to Dr. Ettore Carpena for performing the EXAFS measurements, keeping the XRD machine and the deposition chamber in good shape and for all help with the data analysis. Many thanks also for answering thousands of questions and for all discussions.

Herzlichen Dank auch an Dr. Marcus Schwickert, der rund um die Uhr für die Probleme aller Gruppenmitglieder ansprechbar war, und ohne den wahrscheinlich weder die Computer noch die experimentellen Anlagen so reibungslos gelaufen wären.

Ganz herzlich möchte ich mich bei meinen langjährigen Zimmergenossen Dr. Edgar Galindo, Dr. Orlin Iordanov und Velimir Milinovic bedanken. Mit ihnen habe ich immer eine sehr produktive Mischung aus Arbeit, Diskussion und privaten Gesprächen gefunden.

Many thanks to Dr. Sankar Dhar and Stanislaw Gasiorek for patiently answering all my questions around RBS and ion-solid interactions.

Mein ganz besonderer Dank gilt der Feinmechanik Werkstatt. Insbesondere sind hierbei Klaus Arndt und Christof Schmidt zu nennen, die meine Arbeit immer sehr konstruktiv unterstützt haben und mir mit Rat und Tat zur Seite standen. Herzlichen Dank natürlich auch an Peter Arnsberger, Andreas König, Michael Laugsch und Hans-Jürgen Obal, die meine Auftragsfluten ausbaden mußten.

Vielen Dank auch an die Elektronik-Werkstatt und an Herwig Schultz. Sie haben entscheidenden Anteil daran, daß die MOKE-Apparatur letztlich so schnell einsatzbereit war und automatisiert werden konnte.

Bei Detlef Purschke und Andreas König möchte ich mich dafür bedanken, daß die Stunden und Tage im IONAS sehr erträglich wurden. Über den reibungslosen Betrieb des Beschleunigers hinaus waren beide immer für Fragen des Beschleunigerfahrens ansprechbar. Ohne diese Unterstützung hätte wohl so manche Strahlzeitverlängerung nicht stattgefunden.

Herzlichen Dank auch an die guten Seelen des Instituts Christa Wohlfahrt, Lucie Hamdi und Heike Ahrens, die immer ansprechbar waren, wenn man Probleme hatte.

Dank auch an alle anderen Mitarbeiter des II. Physikalischen Instituts und an alle ehemaligen Kollegen, die für eine angenehme Arbeitsatmosphäre sorgten und teilweise noch aus dem Berufsalltag heraus wichtige Tips gaben.

Besonderen Dank an meine Englisch-Korrektoren Lucie Hamdi und Axel Knust, die mit Engelsgeduld (hoffentlich) auch die letzten Fehler aus der Arbeit herausbügelten.

Ganz herzlich möchte ich mich bei den Kollegen der Materialphysik bedanken, die mit Filmpräparation, Texturmessungen und SIMS zum Teil einen wesentlichen Beitrag zum experimentellen Teil dieser Arbeit leisteten. Insbesondere sind hier Jörg Faupel und Prof. H.U. Krebs zu nennen, die trotz des bevorstehenden Umzugs noch die PLD Filme präpariert haben.

Außerdem herzlichen Dank an die Arbeitsgruppe von Herrn Prof. Felsch und an Herrn Juniorprof. Dr. Markus Münzenberg, bei denen in der Anfangszeit dieses Projektes alle MOKE Messungen durchgeführt wurden, und die beim Aufbau der neuen MOKE Apparatur unentbehrliche Starthilfe gegeben haben. Namentlich sind in diesem Zusammenhang Frank Leuenberger und Dr. Andrea Käufler zu nennen.

Nicht zuletzt auch herzlichen Dank an Ulf Wiedwald und Herrn Prof. Farle von der Uni Duisburg und an Dr. Sabine Pütter von der Uni Hamburg, mit deren Hilfe FMR und MOKE Messungen gemacht wurden und die immer offen für Diskussionen waren.

Schließlich möchte ich meinen Eltern, meinem Bruder und Katrin danken. Sie waren mein persönlicher Rückhalt in den letzten Jahren und waren Tag und Nacht für meine Probleme ansprechbar.



# Lebenslauf

## Persönliche Daten

Name: Georg Alexander Müller  
Geburtsort und -tag: Kassel, 23.03.1974  
Familienstand: ledig  
Staatsbürgerschaft: Deutscher

## Schule

1980 - 1984: Grundschule Lohfelden  
1984 - 1993: Engelsburg Gymnasium, Kassel  
Juni 1993: Abitur

## Wehrdienst

Juni 1993 - September 1994: Stabsmusikkorps der Bundeswehr

## Studium

Oktober 1994 - September 1998: Studium in den Fächern Mathematik Diplom und Mathematik/Physik Lehramt an Gymnasien an der Universität Göttingen  
April 1998 - März 2000: Studium im Fach Physik Diplom an der Universität Göttingen  
Februar 2000: Diplom im Fach Physik mit einer Arbeit zum Thema "Spektroskopie von Hochspinzuständen in  $^{104}\text{Cd}$ "  
April 2000 - Oktober 2002: Studium im Fach Mathematik/Physik Lehramt an Gymnasien an der Universität in Göttingen  
seit April 2000: Aufbau- bzw. Promotionsstudium im Fach Physik an der Universität Göttingen

## Lehre

Oktober 1998 - September 2000: Assistent im Praktikum für Studierende mit Physik als Nebenfach am II. Physikalischen Institut, Universität Göttingen  
seit Oktober 2000: Assistent im Praktikum für Studierende mit Physik als Hauptfach am II. Physikalischen Institut, Universität Göttingen

